METHODS AND TOOLS FOR PRELIMINARY LOW THRUST MISSION ANALYSIS

DANIEL MARCELL NOVAK

Submitted in fulfilment of the requirements for the
Degree of Doctor of Philosophy

School of Engineering
College of Science and Engineering
University of Glasgow

Abstract

The aim of the present thesis is to develop new methods that are useful for a space mission analyst to design low thrust trajectories in the preliminary phases of a mission study, where the focus is more on exploring various concepts than on obtaining one optimal transfer. The tools cover three main axes: generating low thrust trajectories from scratch, improving existing low thrust trajectories and exploring large search spaces related to multiple gravity assist transfers. Stress is put on the computational efficiency of the tools.

Transfer arcs are generated with shaped based approaches, which have the advantage of having the ability to reproduce close to optimal transfers satisfying time of flight constraints and varied boundary constraints without the need for propagation. This thesis presents a general framework for the development of shape-based approaches to low-thrust trajectory design. A novel shaping method, based on a three-dimensional description of the trajectory in spherical coordinates, is developed within this general framework. Both the exponential sinusoid and the inverse polynomial shaping are demonstrated to be particular two-dimensional cases of the spherical one. The pseudo-equinoctial shaping is revisited within the new framework, and the nonosculating nature of the pseudo-equinoctial elements is analysed. A two-step approach is introduced to solve the time of flight constraint, related to the design of low-thrust arcs with boundary constraints for both spherical and pseudo-equinoctial shaping.

The solutions derived from the shaping approach are improved with a feedback linear-quadratic controller and compared against a direct collocation method based on finite elements in time. Theoretical results are given on the validity of the method and a theorem is derived on the criteria of optimality of the results. The shaping approaches and the combination of shaping and linear-quadratic controller are tested on four case studies: a mission to Mars, a mission to asteroid 1989ML, to comet Tempel-1 and to Neptune.

The design of low thrust multiple gravity assist trajectories is tackled by an incremental pruning approach. The incremental pruning of reduced search spaces is performed for decoupled pairs of transfer legs, after which regions of the total search space are identified where all acceptable pairs can be linked together. The gravity

assists are not powered therefore the trajectory is purely low thrust and the transfer arcs are modelled by shaping functions and improved with the linear quadratic controller. Such an approach can reduce the computational burden of finding a global optimum. Numerical examples are presented for LTMGA transfers from Earth to asteroid Apollo and to Jupiter.

Table of Contents

List of Figures

List of Tables

Acknowledgements

The work within this thesis has been partially supported by Qinetiq through an ICASE EPSRC grant.

Special acknowledgement goes to my supervisor, Max Vasile, who provided ideas and guidance to numerous aspects of my research. He has been supportive along the entire duration of my affiliation to University of Glasgow.

Many friends and colleagues provided the basis for enjoying the time spent both in the research room and outside of work. I will not forget that.

This thesis is dedicated to my family whose unconditional support never fades.

Relevant Publications by the Author

Novak, D. M., Vasile, M.: An Improved Shaping Approach to the Preliminary Design of Low-thrust Trajectories, Journal of Guidance, Control and Dynamics Vol. 34, No. 1, January-February 2011

Vasile, M., Novak, D. M., et al.: Incremental Solution of LTMGA Transfers Transcribed with an Advanced Shaping Approach, Proceedings of the 61st International Astronautical Congress, Prague, Czech Republic, 2010, IAC-10.C2.9.8

Novak, D. M., Vasile, M.: An Improved Approach to Preliminary Mission Design Using Fast Linear Quadratic Intermediate Optimisations, Proceedings of the 60th International Astronautical Congress, Daejon, South Korea, 2009, IAC-09.C1.10.5.

Novak, D. M., Vasile, M.: A New Shaping Approach for Preliminary Low-Thrust Trajectory Design, Proceedings of the 21st International Symposium on Space Flight Dynamics, Toulouse, France, 2009.

Novak, D. M., Vasile, M.: Optimal Preliminary Design of Low-Thrust Trajectories Through Two Novel Shaping Approaches, Proceedings of the 27th International Symposium on Space Technology and Science, Tsukuba, Japan, 2009.

Author's Declaration

Glasgow, April 2012

I hereby declare that this submission is my own work and that, to the best of my knowledge and belief, it contains no material previously published or written by another person nor material which to a substantial extent has been accepted for the award of any other degree or diploma of the university or other institute of higher learning, except where due acknowledgment has been made in the text.

Daniel Marcell Novak

Nomenclature

List of acronyms

AU	Astronomical Unit
DSM	Deep Space Manoeuvre
E	Earth
ESA	European Space Agency
GASP	Gravity Assist Space Pruning
J	Jupiter
JAXA	Japan Aerospace Exploration Agency
LQ	Linear Quadratic
LTMGA	Low Thrust Multiple Gravity Assist
M	Mars
Me	Mercury
MGA	Multiple Gravity Assist
MJD	Modified Julian Day
MJD2000	Modified Julian Day since 2000 (counted since 1st of Jan. 2000 noon)
NASA	National Aeronautics and Space Administration
NEA	Near Earth Asteroid
SEPTOP	Solar Electric Propulsion Trajectory Optimisation Program
STOUR	Satellite Tour Design Program
V	Venus

List of symbols

$\mathbf{A}$	homogeneous part in the equations of motion
$\mathbf{A}_g$	submatrix of $\mathbf{A}$
$\mathbf{a}$	acceleration vector of the trajectory parameterised by t
$\tilde{\mathbf{a}}$	acceleration vector of the trajectory parameterised by s

a_i	coefficients in the shaping function R
$\mathbf{B}$	control matrix coefficient in the equations of motion
BV_j	Box or hyperbox created around the set V_j
C_i, C_f	initial and final conditions on the value of R'' and Φ''
$\mathbf{C}_x$	functions defining the osculating conditions
c	geometric curvature
D	time equation scalar function
$\mathbf{E}$	solution of the matrix Riccati differential equation
f	equinoctial element
$\hat{f}$	pseudo-equinoctial element corresponding to f
f_i	coefficient in the shaping function $\hat{f}$
$\tilde{f}$	modified equinoctial element
g	equinoctial element
$\hat{g}$	pseudo-equinoctial element corresponding to g
g_x	generic function
g_i	coefficient in the shaping function $\hat{g}$
$\tilde{g}$	modified equinoctial element
$\mathbf{H}$	Hessian matrix
H	Hamiltonian function
h	equinoctial element
$\hat{h}$	pseudo-equinoctial element corresponding to h
$\mathbf{h}$	angular momentum vector of the trajectory parameterised by t
$\tilde{\mathbf{h}}$	angular momentum vector of the trajectory parameterised by s
h_i	coefficient in the shaping function of $\hat{h}$
I	total search space of the MGA problem
I_i	Set of possible encounter dates for the leg i in the MGA problem
$\mathbf{I}_3$	identity matrix of rank 3
I_t	open interval of time
$\bar{I}_t$	closure of I_t
J	cost function
k	equinoctial element
$\hat{k}$	pseudo-equinoctial element corresponding to k
k_i	coefficient in the shaping function $\hat{k}$

L	longitudinal anomaly, rad
n_r	number of revolutions
$\mathbf{O}_3$	null matrix of size 3×3
O	Landau symbol of asymptotic domination
$\wp$	optimisation problem
$\mathbf{p}$	adjoint variable vector
p	semi-latus rectum
$\mathbf{Q}$	weight matrix
$\mathbf{q}$	generalised coordinate vector
R	function shaping r
$\mathbf{r}$	radius vector, km
r	radius, km
S_i	sets of admissible shaping functions
s	generic parameter used to describe the trajectory
T_χ	shaped time of flight function
T_{viol}	time of flight violation
T	time of flight function
T_i	range of times of flight for leg i
t	time
$\mathbf{u}$	control acceleration vector
$\mathbf{v}$	velocity vector of the trajectory parameterised by t, km/s
$\tilde{\mathbf{v}}$	velocity vector of the trajectory parameterised by s
v_i	component of $\mathbf{v}$ in Cartesian coordinates, km/s
U	three dimensional space without the origin
V_i^d	pruned space accounting for leg 1 to leg i.
W	set of admissible state vectors
$\mathbf{x}$	state vector
x	Cartesian coordinate, km
y	Cartesian coordinate, km
z	Cartesian coordinate, km
α	azimuthal angle in the tangential-normal reference frame, rad
δ	deflection angle arising from a gravity assist
γ	flight path angle, rad
Δv	velocity increment resulting from the control, km/s

δ	elevation angle, rad
θ	azimuthal angle in the spherical reference frame, rad
λ_i	shaping parameters
μ	gravitational constant, km^3/s^2
$\boldsymbol{\xi}$	perturbation of the state vector
τ_i	spacing between consecutive dates in I_i^d
$\boldsymbol{\upsilon}$	perturbation of the control vector with linearised equations of motion
Φ	function shaping φ
φ	elevation angle in the spherical reference frame, rad
ϕ	phasing angle, rad
χ	scalar function shaping T
Ω_x	set on which $\dot{\mathbf{x}}$ is defined

Subscripts

f	final
h	component along the angular momentum
i	initial
l	corresponding to the linearised problem
max	maximal
n	component along the normal vector
$\mathbf{r}$	corresponding to the position components inside the state vector
r	component along the radial vector
rel	relative
$real$	corresponding to the physical, non-linearised problem
t	along the velocity vector
$\mathbf{v}$	corresponding to the velocity components inside the state vector
θ	component along the transversal vector
φ	component along the base vector corresponding to the elevation
0	corresponding to the reference trajectory
1	corresponding to the augmented linearised equations of motion

Superscripts

d	discretised set
(i)	related to leg i
T	transpose of a matrix
$\square'$	derivative with respect to s
$\square''$	double derivative with respect to s
$*$	optimal

Other

$\wedge$	cross product

CHAPTER 1 INTRODUCTION

The intention that motivated the work presented in this thesis was to develop useful mathematical and numerical tools that can be used by a space mission analyst in the preliminary phases of a low thrust mission study. It will become obvious to the reader that these methods involve several fields of astrodynamics, and mathematics in general.

To put the scope of this work into perspective within the rich field of space mission analysis, before immersing into the review of the state of the art found in the scientific literature, it is useful to skim through the major milestones that paved the way for astrodynamics and low thrust trajectory design, as we know them today. The author would like to mention the names of major mathematicians, astronomers, physicists and engineers who introduced powerful concepts that form the backbone of current research, and whose names are recurrent in the field.

Because mission analysts usually require inputs from propulsion system engineers, an overview of the current trends in low thrust propulsion technology is also presented. This helps understand which are the most important parameters that are relevant for trajectory design during a study.

After stating the objectives, the structure of the thesis is laid out in the last part of this chapter.

1.1 Concise history of astrodynamics and celestial mechanics leading up to mission analysis

Astrodynamics is the study of the motion of objects moving in gravity fields and possibly subject to non-gravitational perturbations. It is a branch of celestial mechanics, where the studied objects are assumed to have a negligible mass compared to the primary celestial bodies that generate the gravity fields. Astrodynamics provides therefore the tools to study the motion of artificial satellites. The perturbations to which the artificial satellites can be subject to can be understood broadly as any force that has an effect on a nominal trajectory. Perturbations can

originate from external effects, such as solar radiation pressure, or internal, such as engine firings.

In the following, the main milestones leading up to modern astrodynamics are summarised, the section is not intended to be a detailed account of the history of astrodynamics and celestial mechanics.

1.1.1 Celestial mechanics as the foundations of astrodynamics

Astrodynamics grew out as a branch of celestial mechanics progressively. Its origins are confounded with the latter's and can be traced back to Johannes Kepler who started to treat astronomy – a branch of mathematics in his time – as part of universal mathematical physics. Kepler laid down the mathematical foundations of orbital dynamics. Kepler's three laws of planetary motion, dating from the beginning of the 17th century, enabled the more accurate computation of the ephemerides of planets. They were later derived by Isaac Newton from the latter's law of universal gravitation, which he published in 1686 [1].

Newton's contribution was fundamental because he laid down the underlying physical laws of celestial mechanics and provided the mathematical tools that later allowed describing more complex systems and developing techniques to treat elaborate problems. Johann Heinrich Lambert, in the middle of the 18th century, studied conic sections and formulated the theorem linked to his name and which is used for finding impulsive transfers still today. Later on, with the development of calculus of variations and analytical mechanics, Joseph Louis Lagrange and Carl Friedrich Gauss derived the planetary equations governing the evolution of the orbital elements under perturbations. Carl Gustav Jacob Jacobi studied the problem of a small body moving in the field of two larger celestial bodies that move circularly around their barycentre. Along with the refinement of observational gears, mathematical techniques also improved for determining accurately orbits using terrestrial observations. Sir William Herschel discovered Uranus in 1781, the first planet to be discovered using a telescope, and in 1821 Alexis Bouvard realised that its motion is perturbed, for which he suggested that a yet unknown planet's gravity field perturbs its orbit. The level of refinement of the mathematical techniques in celestial mechanics reached such heights by the middle of the 19th century that Neptune was discovered by shear mathematical prediction. In fact, Johann Gottfried Galle from the

Berlin Observatory observed Neptune within 1 degree from Urbain Le Verrier's theoretical prediction. This marked the culmination of Newtonian mechanics.

Observations of Mercury's perihelion precession led Le Verrier to apply the techniques he used for predicting Neptune's orbit and to propose the presence of a planet closer to the Sun. The name Vulcan was already given to that hypothesised planet, and it was expected to be only a matter of time for the planet to be observed for the first time. Many astronomers put effort into finding the hiding Vulcan but the discovery never came. The correct explanation for the anomaly of Mercury's orbit only came from Albert Einstein's General Theory of Relativity, published in 1916, which actually exploited the precession as one of the major validations of the theory.

In the beginning of the 20th century, another important scientist gave a strong impulse to mathematical methods of celestial mechanics, namely Henri Poincaré. He applied the tools he developed in dynamical systems theory to the N-body problem, with the objective of studying the stability of the Solar System, a problem that attracted much interest in his time. The modern mathematical methods that Poincaré introduced are actively used today, whence the problem is centred on a nonlinear dynamical system.

1.1.2 Modern astrodynamics and mission analysis

Konstantin Tsiolkovsky's publication in 1903 [2] was the first one to address the dynamical property of an object propelled by a thruster expelling exhaust gas and carrying its own propellant on board. Tsiolkovsky used the kinematic quantity Δv, the change in velocity due to the thrust, and linked it to the exhaust velocity of the gases and the mass of expelled propellant. If one writes down the conservation of linear momentum, one has:

$$T = m\dot{v} = -\dot{m}v_e \tag{1.1}$$

where T is the thrust acting on the spacecraft, m is the spacecraft's mass and v_e the exhaust velocity of the propellant. Rearranging and integrating the second equation results in the Tsiolkovsky equation:

$$m_{propellant} = -\Delta m = m_{initial}\left(1 - \exp\left(-\frac{\Delta v}{v_e}\right)\right) \tag{1.2}$$

Although the model can be applied to many mechanical scenarios, it marks the start of the theoretical study of the motion of man-made objects moving outwith the Earth's atmosphere. The exhaust velocity is a key parameter of the propulsion system since it governs the amount of Δv achievable for a given initial and propellant mass. It is in fact the thrust per unit mass flow of propellant. Engineers later introduced the so-called specific impulse I_{sp}, defined in seconds, as the thrust per unit weight flow of propellant.

$$I_{sp} = -\frac{T}{\dot{m}g} = \frac{v_e}{g} \tag{1.3}$$

The German engineer Walter Hohmann, interested in interplanetary transfers in the 1920s, studied the most efficient way to transfer between two circular coplanar orbits [3]. He devised an approach using two impulsive thrusts, one to escape the initial orbit and one to insert into the final orbit, and which are tangential to the departure and arrival velocities. Hohmann's works were the first ones to address the need to minimise propellant mass, a crucial consideration in designing real space missions.

Research in the field of astrodynamics considerably accelerated with the advent of the Space Age in 1957, when the first artificial satellite, Sputnik 1, was sent into space. Mission analysis emerged as the engineering activity during space mission design dealing with the design and the analysis of orbits and transfers, interfacing with different subsystems of the space mission. At the heart of mission analysis lies astrodynamics. The geopolitical context imposed the need for ever-increasing mission performances and capabilities and astrodynamics made considerable advancements. These were made possible with the development of two disciplines: mathematics and computer sciences. A central focus of astrodynamics quickly became transfer optimisation, and Pontryagin's maximum principle, published in 1962 [4], laid down the mathematical bases for it.

It became clear that analytical solutions are very scarcely available, so numerical techniques have been developed, adapted to the computational resources at hand. In the early days, engineers relied heavily on their experience due to the limited

resources available. Their models had to be simple in the first place and, when using iterations, like Newton loops, for finding solutions numerically, they had to spend time finding initial guesses themselves to help the computers converging.

Transfers were initially designed by patching together segments of orbits with impulsive manoeuvres in between. This assumption of instantaneous orbit changes proves to be valid when the acceleration created by the thruster exceeds significantly the acceleration created by the local gravity field and the manoeuvre is short. This is often the case when chemical propulsion is employed.

With time, the complexities of the envisaged transfers increased, because it was recognised that by increasing the search space, better solutions could be found. For example, introducing gravity assists provided free orbit changes but increased the number of variables. Not only did the mathematical formulation of mission scenarios increase in complexity, but also the underlying dynamical systems became more sophisticated. The effects of various perturbing forces were introduced into the equations of motion.

With the advent of missions relying on spacecraft flying at Lagrange points, an active field of study became the design and control of trajectories in the three-body problem. The aim there is to exploit the properties of the corresponding dynamical system to reach and maintain optimally exotic orbits (e.g. halo, Lissajous, Lyapunov, homoclinic, heteroclinic orbits). It has also been proven that reduction in propellant mass can be achieved by exploiting four-body dynamics. The Japanese Hiten mission to the Moon was rescued in 1991 using the trajectory proposed by Edward Belbruno [5] going through the weak stability boundary of the Earth-Moon-Sun system. It should be noted that the improvement in the necessary propellant mass comes at the expense of increased transfer time.

Optimisation is central to most of today's research in astrodynamics, be it for the design of transfers or for elaborating a navigation strategy. Efforts are put into combining mathematical results and numerical methods in different ratios, with the ultimate aim of automating the search for optimal transfers as much as possible and raising the reliability of numerical techniques.

Since the mid 1990s, an area under increased investigation is low-thrust trajectory design, whereby transfers are not subject to manoeuvres considered impulsive anymore but to continuous ones whose magnitudes are the same or lower than the local gravity field's. Electric propulsion and solar sails are example of technologies

that have such characteristics. The former are considered flight proven since NASA's Deep Space 1, launched in 1999, to asteroid Braille and comet Borrelly. A higher specific impulse is achieved by accelerating charged particles in an electric field; therefore higher Δv is obtained compared to chemical propulsion for the same mass of propellant. However the thrust magnitude is much lower, so thrusting is done for long periods of time and transfers take longer. The impact on trajectory design is that a thrust profile is to be optimised. This is mathematically and numerically a particularly challenging task since a function and not a finite dimensional vector has to be theoretically optimised, and a multitude of approaches – which will be thoroughly covered later in this chapter – have been tried with different levels of success.

Astrodynamics is a rich field and it is not in the scope of the present section to describe all of the aspect being researched. It can be said however that the study of low thrust propulsion opened up new topics of research in which its combination with high thrust or even solar sails are explored. Other major topics of interest today in astrodynamics are those where the subject of the study is a system of objects instead of a single object. These can be space tethers, constellations, satellite formations or swarms, whereby the dynamics of the system become more complex.

1.2 Low thrust propulsion

1.2.1 Principle

The main reason why a space mission analyst makes a distinction between low thrust and high thrust propulsion is because of the impact on trajectory design. For high thrust manoeuvres the total momentum change is generally achieved in a very short time compared to the time scales of the trajectory. In the two-body model for instance, the relevant time scale of reference would be the lower between the initial and final orbital period. In that case, a convenient assumption is that the thrust is impulsive such that a simple Δv vector representing the instantaneous change in velocity can model the manoeuvre. For low thrust propulsion, thrust can be applied for very long times.

One can define propulsion as being low thrust when the thrust produced on the spacecraft is substantially lower than the gravitational force acting upon the satellite.

It is also possible to define it in terms of acceleration: the relative difference between the spacecraft's total acceleration and the local gravitational acceleration is close to zero.

The latter definition is general in the sense that it does not fix the engineering technique with which the action-reaction principle is implemented. The change in momentum can therefore originate either from mass that is first accelerated and then ejected from the spacecraft or from external particles that transfer their momentum to the spacecraft by interacting with it. The former case gives rise to the more conventional propulsion systems where an on-board tank carries fuel that is accelerated by exploiting chemical, thermodynamic or electric processes, while the latter, less common solution, can be implemented by a momentum exchange with solar photons or laser beam photons.

It is important to note that from the point of view of a mission analyst, if the thrust duration allowed by the propulsion system is short, designing transfers where the thrust is low is the same as when the thrust is high, such that the manoeuvres can in either case be modelled as impulses. Thus the possibility to apply thrust for longer periods, up to multiple revolutions, is an important specificity of the so-called low thrust propulsion systems for the mission analyst. This observation discards for example miniaturized cold gas or chemical propulsion systems, where achievable acceleration is effectively low but the limited size of the propellant tank on board forbids any longer thrust duration.

One can argue then that by putting a larger tank on board the spacecraft that the aforementioned cold gas and chemical propulsion can be considered as low thrust propulsion for a mission analyst. It would certainly be the case in theory, but in practice that would not happen because the spacecraft would tend to become a flying tank, whereby the thrust would mainly be used for accelerating the propulsion system alone.

However, if the exhaust velocity is raised while every other parameter remains unchanged, the same low thrust level can be achieved with lower mass flow rate of the ejected particles, in which case there will be enough propellant in the tank to thrust for longer. This is the reason why in practice, for mission analysts, low thrust propulsion suggests automatically high exhaust velocity, i.e. specific impulse. In the following, different propulsion technologies are presented, from conceptual to flight proven, and which would be qualified as low thrust by a mission analyst.

1.2.2 Low thrust propulsion systems carrying propellant on board

Increasing the specific impulse of a propulsion system can be achieved by having a system that converts energy from an abundant source into kinetic energy for the exhaust particles. There are many ways to do that and many types of propulsion systems have been studied and developed up to different levels of technology readiness in that regard. Here it is not the purpose to explain in detail the way in which the different types of engines work but to provide an oversight of the different physical effects that are exploited in order to achieve an acceleration of the spacecraft. Extensive references are found in [6], [7] and [8]. The goal is to extract the main parameters that a mission analyst would have to take into account when designing and analysing transfers for real missions using low thrust propulsion.

According to the implementation of the thruster, the energy from the source can be converted into different forms before ending up as the propellant's kinetic energy. The conversions are generally not perfect and losses arise. The efficiency η of the thruster is then defined as the ratio between the rate of kinetic energy expelled by the thruster and the power P input to the system.

$$\eta = \frac{\dot{m}_{propellant} v_e^2}{2P} \tag{1.4}$$

so

$$P = \frac{T^2}{2\eta \dot{m}_{propellant}} = -\frac{m^2 a^2}{2\eta \dot{m}} \tag{1.5}$$

where a is the acceleration of the spacecraft. Note that these equations are valid if all particles are exhausted with the same velocity v_e, in the direction opposite to the spacecraft's velocity vector. Note that v_e can however depend on time.

Nuclear and solar energy are two abundant energy sources but the power they can provide depends on the size of the power plant on board the spacecraft. Hence it is not worth increasing the specific impulse limitlessly: the higher the specific impulse the

less propellant mass is needed on board, but the more power is required to accelerate the propellant and therefore the heavier the power system will be. Indeed, if one considers the often-used power to thrust ratio:

$$\frac{P}{T} = \frac{v_e}{2\eta} \tag{1.6}$$

then it becomes obvious that for the same thrust, a higher exhaust velocity will require proportionately higher power.

Nuclear energy can be used to heat a chemically non-reactive propellant, which is then expelled through a nozzle. Another way to harness nuclear energy is by converting it into electric energy, which is then used to accelerate charged particles. Solar energy can be exploited the same way by converting electromagnetic power from sunlight into electric power. The solar power obtained with a fixed area of solar panel is inversely proportional to the square of the distance from the Sun, so this power source becomes inefficient when going far from the Sun.

Many concepts have been identified and developed for using electric power for spacecraft propulsion [6]. Electrothermal propulsions heat the propellant, usually hydrogen, ammonium or hydrazine using electric energy. Resistojets and arcjets are the two main types of electrothermal thrusters. Resistojets transfer heat through resistive conductors shaped in coils. They have specific impulses of about 300 s and require 0.4 to 2 kW power and have the advantage of being relatively simple. Arcjets create electric arcs in the gas flow to heat up the propellant and expand it. Their power requirement is of the same order of magnitude as that of resistojets but their specific impulse can go up to 800 s. Electrothermal propulsion has been used on several Earth orbiting missions for station keeping and orbit insertion.

Electrostatic and electromagnetic propulsion is based on accelerating charged particles using differences of electric potential for the former and Lorentz force for the latter. Electrostatic types of thrusters include gridded ion thrusters that work generally with Xenon gas which is ionised by bombarding it with electrons. The gas is accelerated by passing through grids within which a strong electric field is applied. Specific impulses of more than 3000 s are achievable with power consumption up to 2.5 kW. Thrust magnitudes from a few millinewtons up to a Newton can be obtained,

depending on the input power. These thrusters can be throttled by adjusting the flow rate of propellant and the input power.

Hall effect thrusters also accelerate charged particles, but the ionisation of the gas and the acceleration of the created plasma takes place in a cylindrical region where the electrons move circularly under the effect of a radial magnetic field forming effectively a Hall current. The electric field is created by the anode placed at the base of the cylinder and the cathode formed by the cloud of electrons. Similar performances are achievable compared to the gridded ion thrusters and both have been proven to operate for thousands of hours continuously or in cycles.

Electrostatic thrusters based on accelerating charged colloid droplets were first studied in the 1960s and have known a rebirth of interest in recent years due to their potential to serve as engines for very small spacecraft. They generally provide thrust below 10 mN with a specific impulse of 1000 s.

Propulsion systems using electromagnetic force are characterised by whether they are steady or unsteady, and self-field or applied field. An external field is applied when the discharge current does not generate a magnetic field strong enough to ensure the high performance of the thruster. When it comes to unsteady systems, capacitors discharge power in pulses. The most common electromagnetic thruster is the pulsed plasma thruster where the propellant is usually solid Teflon that is ablated, ionised and expelled. They are simple and reliable and have specific impulses around 1000 s, but provide thrust only below 10 mN.

Magnetoplasmadynamic thrusters are on the other hand steady thrusters, where a complex interaction between either induced or applied magnetic fields and electric fields accelerates the plasma out of the engine. They have been proven to allow for specific impulses above 2000 s and thrust above 20 N, but at the expense of power consumption of the order of megawatts. Due to the complexity of the phenomena involved in this kind of propulsion system, theoretical and numerical results lag behind empirical results.

1.2.3 Alternative low thrust propulsion systems

Propulsion systems where no propellant is carried on board have also been studied. Among these are solar lightsailing, magnetic loop sail and beamed laser propulsion [6]. They are considered more exotic due to the physical phenomena they exploit and

the particular dynamics they involve, in a way that trajectory design, from the point of view of a mission analyst, requires specific methods. Solar sailing attracts the most interest from researchers because it would be less challenging and expensive to implement than the others. At 1 AU, a perfectly reflective sail perpendicular to the Sun line would produce a thrust per sail area ratio of 9.1 $\mu N/m^2$. The accelerations for a spacecraft are therefore very small. This property, combined with the necessity to take into account the directional constraints on the sail and its controllability, makes transfer designs challenging [9]. Indeed, it is difficult to find a priori initial guesses that are feasible in terms of control constraints and state constraints. Even for a simple rigid solar sail model, the control direction constraint is an additional constraint compared to a scenario using conventional electric propulsion. In practice however, the inertia and the flexible nature of the sail complicates the real dynamics by a lot.

1.2.4 Missions flown using low thrust propulsion

Many of the propulsion system types described above are flight proven already. Resistojets, arcjets, hall effect thrusters and pulsed plasma thrusters have all flown many times, but due to their limited size and performance they have only been used for precise attitude control or minor station keeping manoeuvres. Using low thrust propulsion systems as primary propulsion system to perform major orbit changing manoeuvres dates back only to 1998, with the launch of NASA's Deep Space 1. Since then more such spacecraft have flown or are planned due to the reduction in propellant mass that they allow and the progressing advances in technology readiness levels.

Deep Space 1 was equipped with Boeing's NSTAR gridded ion engine and flew by asteroid Braille and comet Borrelly [10]. The launch mass was 486 kg and 81.5 kg of Xenon was initially carried in the tank. The mission's trajectory is illustrated in Fig. 1.1.

The same engines are currently flying on NASA's Dawn mission, launched in 2007, to rendezvous Vesta and Ceres [11]. A gravity assist at Mars is performed. The engine delivers a maximum thrust of 92 mN that is reached for an input power of 2.6 kW and a specific impulse of 3200 s. The Dawn spacecraft weighed 1240 kg at launch and carried 450 kg of xenon on board. Fig. 1.2 illustrates the transfer strategy of the mission.

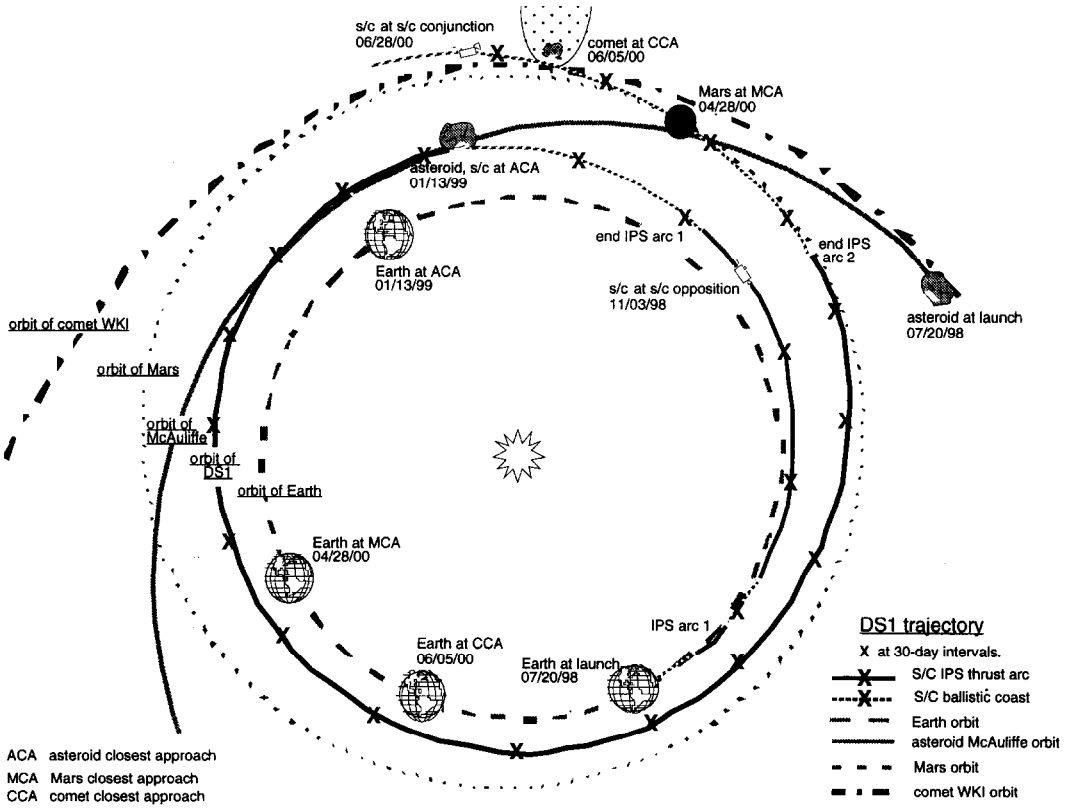

Fig. 1.1 Deep Space 1 mission trajectory [10]

ESA launched SMART-1 to orbit the Moon in 2003. It carried SNECMA's PPS 1350-G Hall effect thruster using Xenon [12]. The initial launch mass was 367 kg which included 82 kg of Xenon. The total thrust time reached almost 5000 hours to provide a total Δv of 3.9 km/s. The thruster was supplied with electrical power of up to 1200 W.

Japan launched Hayabusa in 2003 to return samples from asteroid Itokawa [13]. The mission weighed 510 kg at launch and carried four cathode-less electron cyclotron resonance ion engines, providing 8 mN each and a specific impulse of 3200 s. 60 kg of xenon was carried in the propellant tank. Depending on the distance of the spacecraft from the Sun, the solar arrays provided power to the propulsion thruster up between 250 and 1100 W.

The success of SMART-1 encouraged ESA to employ electric propulsion on BepiColombo, its cornerstone mission to Mercury. BepiColombo will be a spacecraft of a larger class. It will be launched in 2014 and cruise for 6 years until being ballistically inserted in an elliptical orbit around Mercury [14]. The spacecraft will weigh 2.3 tons at launch and will be propelled by four of QinetiQ's T6 gridded ion thruster using xenon, inherited from the T5 thruster currently flying on ESA's GOCE

mission. The thrusters have been shown to provide up to 145 mN of thrust and a specific impulse of up to 4300 s when powered by 4.5 kW. The efficiency has been shown to reach 66%. In order to reduce the propellant requirement, BepiColombo will make use of a number of gravity assists around the Earth, Venus and Mercury such that the nominal Δv will be close to 7 km/s. BepiColombo's complex trajectory is illustrated in Fig. 1.3.

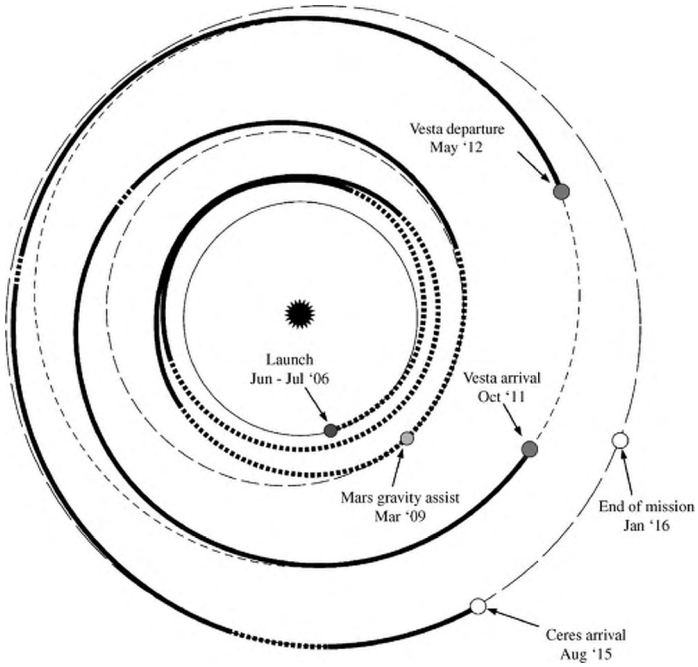

Fig. 1.2 Baseline trajectory of NASA's Dawn mission [11]

Low thrust propulsion with high specific impulse opens up clearly new possibilities for future missions. Their combination with gravity assists makes it clearly possible to fly missions necessitating high Δvs while keeping a high scientific return.

The more missions are flown the more technology readiness levels rise and manufacturing costs reduce, endowing electric propulsion with even more potential for future flights.

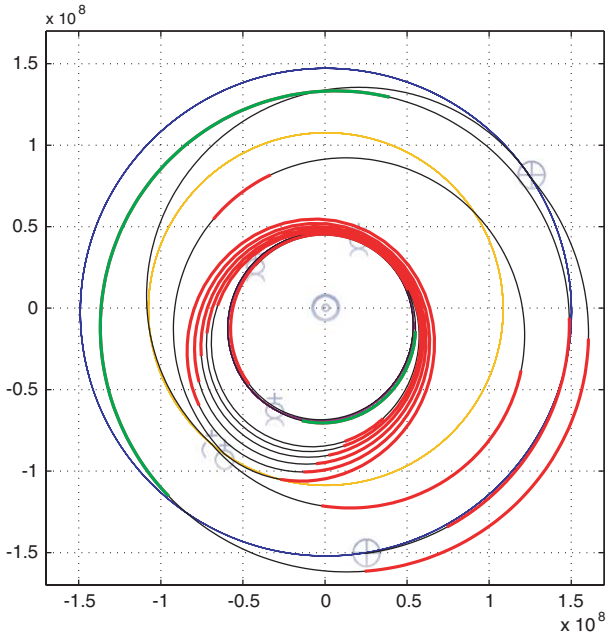

Fig. 1.3 One of the studied trajectories for the BepiColombo mission [14]. Thrust arcs are in red and green. Axes' unit is km.

1.3 Gravity loss

When dealing with low thrust manoeuvres, the change in momentum of the spacecraft happens continuously while the duration of the manoeuvre can be substantial. The manoeuvre cannot be considered instantaneous anymore and is modelled by a vector function of time. The consequence of the continuous thrust model is that both the engine and the gravity field act on the spacecraft simultaneously along the trajectory, so in order to achieve a given change in momentum, the manoeuvre must take into account the gravity's continuous effect. This phenomenon is called gravity loss. There is however no general mathematical definition for it, because it is not straightforward to define the impulsive manoeuvre to be used as reference for a manoeuvre lasting longer.

It can be argued however that gravity loss can be both positive and negative, depending on whether gravity acts along or opposite the direction of the thrust. Therefore the term gravity loss is inappropriate, since gravity can also help achieve the desired change in velocity. The expression gravity loss originally comes from the pull that gravity exerts on a launcher while climbing. Indeed, in that scenario, to

obtain the rocket's change in velocity, the Δv due to gravity needs to be subtracted from the Δv imparted by the rocket's engines.

Qualitatively one expects higher absolute value of gravity loss when the local gravity field gets higher and when the thrust time gets longer. So the lower the thrust level provided by the propulsion system, the more gravity loss should be taken into account. Gravity loss also depends on the direction of thrust. Indeed, an infinitesimal change of momentum in a direction perpendicular to the local gravity field can be obtained without having to compensate for gravity, whereas for the same change in momentum in a direction along the local gravity line requires a priori a small manoeuvre that compensates the effect of gravity.

A similar phenomenon also occurs when the spacecraft is subject to atmospheric drag, whereby the manoeuvre has to take into account the effect of the drag. This analogy explains why gravity loss is sometimes also called gravity drag.

After designing a low thrust manoeuvre, gravity loss is generally not computed because it does not provide any information that can be made use of, it just tells whether gravity has been acting in average with the manoeuvre or against it.

There is a case when assessing the gravity loss can be useful. When manoeuvres are initially modelled by impulses, due to the instantaneous nature of the manoeuvres, there is no gravity loss. But when the real manoeuvres are recomputed with a constraint on the thrust magnitude, the engines fire for non-zero durations. The difference in Δv can be interpreted as gravity loss. A mission analyst who uses an impulsive model should add a line in the Δv budget for the margin due to gravity loss, because it is not taken into account in the model. That margin, as described above, will depend on the maximum thrust magnitude, which impacts the duration of firing to achieve the desired Δv.

An important observation arises from the latter consideration. When modelling a low thrust transfer with a succession of impulsive Δvs, no matter how densely the impulsive Δvs are distributed, the model will never take into account the effect of gravity, because gravity is never allowed to affect the manoeuvres' efficiency at any time. Indeed, if one isolates an arc between two impulsive manoeuvres, the arc can be considered as a Lambert arc with an initial and a final Δv. But if the two impulsive manoeuvres at the tips are recomputed and spread out to account for the thrust limit, the total Δv is generally different from the Lambert arc's Δv. This is true no matter

how low the Lambert arc's Δv is, although the model's error converges to zero if the density of impulsive manoeuvres gets high.

1.4 Preliminary design of low thrust trajectories

The need to design low thrust transfers dates back to the late 90s with the Deep Space 1 mission. At that point, the techniques relied heavily on the initial inputs from experienced mission analysts. Modelling thrust arcs is inherently more complicated than modelling impulsive manoeuvres, therefore optimising them can become tricky, because one not only needs to make sure that the optimiser converges, but also that it does not converge to an unfavourable local optimum.

A plethora of techniques have been developed to optimise low thrust trajectories [15]. These can be classified into local and global methods and the former into direct and indirect methods. The following literature review does not cover the optimisation of low thrust trajectories per se, but the methods used to create efficiently suboptimal trajectories, which can eventually be fed into optimisers as a starting point.

Due to the nonlinearity of the low thrust dynamics, it is clear that generating acceptable initial guesses for local optimisers is essential and it has therefore been the focus of several research groups for the last 15 years. Two main approaches exist, that work in generic mission scenarios. The first approach, pioneered by Sims and Flanagan [16], represents thrust arcs by a series of impulsive manoeuvres, which are then optimised by a direct optimiser. An improvement to the initial approach was brought by Yam et al. [17] by replacing the sequence of impulsive manoeuvres by series of low thrust arcs propagated on segments with fixed thrust directions.

The problem with this approach is that an optimisation is required for each trajectory otherwise it does not represent a feasible low thrust transfer: the trajectory would not be continuous or would not satisfy boundary constraints. Therefore it cannot be used within global optimisers without sacrificing computing speeds.

The other approach that has been proposed is through the use of the so-called shaping method [18][19], which is discussed in more detail in the next subsection. This method turns out to be both able to initialise local optimisers and to represent a large array of suboptimal trajectories, such that they can be used either for systematic searches or for global optimisations.

Both these methods have been applied to multiple gravity assist scenarios, as will be elaborated below.

The general approach in the literature is to generate an initial guess using one of the two listed methods for analysing the search space directly or to use it as input to a local optimiser. This can be considered as being a two-step approach. Although the trajectories can be generated fast, their quality can be a problem, in which case the optimiser may not converge, converge to an unfavourable local optimum or converge slowly. It can be then argued that an intermediate step may be of use, whereby the generated trajectories are improved in an efficient way before starting the optimisation. The time lost by improving the first guess would then be compensated by the robustness and speed of the optimisation. This three-step approach has not been addressed in the literature.

1.4.1 Shaping methods

During the preliminary assessment of a new mission concept, a large number of scenarios need to be investigated. As a result, the associated search space can be very large. For instance, launch and arrival windows can each span several years. The assessment of different scenarios over a wide range of design parameters requires the efficient generation and evaluation of a large number of feasible trajectories. Finally, common techniques for low-thrust trajectory design [15] require some form of initial guess. However, the generation of suitable initial guess trajectories during the preliminary mission design phase is not trivial.

To make this step more efficient, modelling trajectories analytically has proven to be a viable option. Markopoulos [18] found a class of planar trajectories with a specific expression for the thrust, which he calls Keplerian thrust, with which the trajectory can be expressed analytically while imposing boundary constraints. Markopoulos's results remained, however, academic, and were not applied to the systematic design of transfers. Petropoulos and Longuski [19] proposed to model low-thrust trajectories with exponential sinusoids and obtain the thrust profile from the dynamics, with the aim of designing propellant-optimal low-thrust gravity-assist trajectories. Petropoulos and Longuski's model is planar; the out-of-plane components are only approximated. Moreover the constraints on the total time of flight cannot be satisfied together with the boundary constraints on the velocity vector. However, the

exponential sinusoids turned out to provide valuable solutions in the pure point-to-point low-thrust problem. Wall and Conway [20] introduced an inverse polynomial to model the radius of a planar trajectory in polar coordinates, under the assumption of a variable unbounded tangential thrust. The advantage of this approach compared with Petropoulos and Longuski's is the possibility to satisfy all boundary conditions. Later in 2008, Wall extended their approach to cylindrical coordinates [21]. De Pascale and Vasile proposed to shape the variations of the non-singular equinoctial elements due to small perturbations [22]. This shaping approach could model three-dimensional trajectories and satisfy boundary, time of flight and thrust constraints. Furthermore, it was demonstrated that the initial guess was good enough to initialize both direct and indirect methods [23].

1.4.2 MGA transfers

Before the eighties, multiple gravity assist (MGA) trajectories were computed with ad hoc methods. It was during the design of the Galileo mission in the eighties that the first codes to compute large sets of trajectories, using impulsive maneuvers, were initially run. These codes gave rise later to STOUR [24]. Williams and Longuski [25] automated the MGA search. STOUR was then used extensively by Petropoulos et al. [26] for assessing a large number of mission scenarios to Jupiter. They also applied STOUR with a model for low thrust transfers called exponential sinusoids [27]. With the development of the field of global optimization, different approaches were tested in order to reduce the computational time to find interesting regions in the search space, for both high thrust and low thrust transfers. These approaches included differential evolution [28], particle swarm optimization [28], evolutionary branching [29] and simulated annealing [30]. Evolutionary neurocontrol was also applied successfully by Carnelli et al. [31] to the low thrust MGA (LTMGA) problems. Depending on the mathematical transcription of the LTMGA transfers, the swingbys can be powered [32]. If the swingby is not powered, consecutive legs are linked together one after the other by specifying the swingby parameters as part of the search space [29], or by computing the best swingby parameters in an inner loop [30][31].

In order to reduce the size of the search space, incremental pruning has been proposed by Becerra et al. [33] on MGA missions and is based on the construction of sets of MGA trajectories, one leg at a time, and removing subsets that do not satisfy a

given criterion, e.g. Δv of the leg too high. The approach exploits the decoupling of the transfer arcs offered by the powered swing-by model. Such decoupling removes the dependency of one arc from the preceding ones, and allows for pruning the search space in polynomial time. The final pruned space can then be explored with a global optimizer. Vasile, Schütze et al. used the exponential sinusoid model [34] to apply incremental pruning to LTMGA problems with powered swingbys.

However the disadvantage in the current techniques using incremental pruning is that gravity assists involve impulsive manoeuvres, such that both a low thrust and a high thrust propulsion system is assumed on board. The problem resides in the lack of flexibility of the low-thrust trajectory models. The exponential sinusoids [27] have the disadvantage of being a planar model and one cannot impose boundary constraints on velocity and time of flight together. Pseudo-equinoctial elements, proposed by Vasile et al. [29] can provide first guess trajectories satisfying boundary constraints, time of flight constraint and thrust constraints. However, the satisfaction of the boundary constraints relies on the convergence of a Newton loop, due to the fact that pseudo-equinoctial elements are not osculating. Indeed, the pseudo-equinoctial elements cannot be solved analytically because the presence of a thrust makes the velocity vector associated to the pseudo-equinoctial elements becomes different from the one associated to the osculating elements without presence of thrust.

1.5 Objectives

The primary objective of this thesis is to identify regions of a large search space that contain potentially interesting transfers and not to develop the tools to find the globally optimal trajectory of a low thrust mission. Indeed, in the preliminary phases of mission design many parameters, e.g. launch parameters or propulsion system parameters, are not fixed yet, and finding globally optimal solutions for all combinations of values would be too time consuming, if not impossible. A reduced model representing the main features of a trajectory is therefore central to preliminary low thrust mission analysis.

Along this thesis, the spacecraft is represented as a point subject to the gravitational pull of a single celestial body and to the acceleration generated by a propulsion system. Not including the mass of the spacecraft in the system allows

reducing the number of equations of motion from seven to six. Proceeding this way leaves the trajectory design method independent of the propulsion system's properties. Indeed, the change of mass and the thrust profile of the spacecraft can be computed from the acceleration once an initial mass and the specific impulse are provided. Simple propulsion system models where the specific impulse is constant to complicated ones where the specific impulse depends on the available power on board, which in turn depends on the heliocentric distance of the spacecraft, can also be accommodated a posteriori. This provides flexibility to evaluate in the preliminary stages of the mission study if certain propulsion systems are more appropriate than others.

Often the objective during transfer design is a minimal propellant mass. From the rocket equation one can see that, assuming a constant specific impulse, a lower the Δv the lower the propellant mass, however an optimal trajectory for the Δv can differ from an optimal one for the propellant mass. In fact, optimising for the Δv would be equivalent to setting the specific impulse to infinity, such that the mass of the spacecraft stays constant and therefore the acceleration and the thrust profile are proportional. If the specific impulse is changed into a finite value, the thrust becomes more efficient towards the end of the transfer, when the spacecraft mass is lower and the acceleration is higher, so one would expect intuitively to see the major manoeuvres have the tendency to be shifted towards the end of a transfer. However, the difference between the two optimal trajectories becomes lower the higher the specific impulse.

The level of specific impulse for low thrust missions is usually of the order of thousands of seconds and the thrust magnitude up to a few hundreds of mN, so for a one-ton spacecraft which thrusts for one year in total, one can expect to have a relative change in mass of up to 30%. None of the missions described in subsection 1.2.4 has a mass change ratio above that. Therefore it is not unreasonable to use the Δv as a measure of merit for a trajectory.

A primary objective of this thesis is to present tools to generate three-dimensional trajectories quickly from scratch such that they satisfy boundary constraints on position and velocity as well as time of flight constraints. The trajectory shaping approach has been chosen to tackle this, for which a general mathematical framework has been laid out, covering the shaping methods existing in the literature. A

generalisation of Petropoulos' exponential sinusoids and Wall's inverse polynomials to three-dimensional motion has been performed with success.

It is important that the shaped trajectories represent with reasonable fidelity the feasibility and the optimality of a scenario. Hence it is expected for example for Lambert arcs not to be altered too much if the boundary conditions change slightly. It then becomes possible to assess search spaces without the need to optimise each individual trajectory. Moreover, having the flexibility to construct such trajectories is important for launching local optimisers that usually require an initial guess to converge. The shaping methods within this thesis are shown to behave well in that regard.

It is important to note the Lambert problem for low thrust trajectories, unlike for coast arcs, is not completely defined as long as one does not assign additional constraints or objectives, such as the requirement of a minimal Δv, such that the degree of freedom arising from the possible existence of a thrust arc is dealt with.

In real missions there are limits on the thrust magnitude, so one would want to have the possibility to discard whole regions of the search space if the initial guess trajectories have much higher peak thrust than the theoretical optimal one. Therefore it has been decided to develop a tool that improves the thrust magnitude, and generally the Δv with it, while not performing a complete optimisation. Focus is put on the computational speed of the tool.

The ultimate objective within this thesis is to be able to assess search spaces not only for direct transfers but for MGA transfers as well. Dimensionality can quickly become a problem when the number of encountered planets increases. Recognising the advantages of the incremental pruning of Becerra et al, an adaptation of it has been done by eliminating from the swingby model the impulsive manoeuvre and by using the newly developed trajectory generation tools to model each leg. In this way, the dimension of the search space remains polynomial with respect to the number of planets.

1.6 Outline

The present thesis is structured following an order such the newly introduced tools only make use of tools presented beforehand. The first two chapters are dedicated

respectively to the generation and improvement of low thrust trajectory legs and the third one presents a method using the techniques of the first two chapters to find sets of MGA transfers interesting for a mission analyst.

Trajectory shaping is used to construct low thrust trajectories. A general mathematical framework is built, within which any type of trajectory shaping can be described. A new shaping method is presented whereby the trajectories are described in spherical coordinates. The radius and the elevation angles are expressed as functions of the azimuthal angle. Such an approach is shown to be a more realistic modelling than with of the exponential sinusoids and the inverse polynomials. Following that, the pseudo-equinoctial shaping method is revisited with theoretical insights, which help predict the scenarios in which the generation of acceptable trajectories would fail. For both shaping methods, particular attention is given to the satisfaction of boundary constraints on position and velocity. The satisfaction of time of flight constraints is addressed in a separate subsection, since a new technique is presented that can be applied to any kind of shaping method. Finally both shaping methods studied are applied to test cases of transfers to Mars, a near Earth asteroid, a comet with eccentric orbit and to Neptune.

The following chapter is dedicated to the improvement of low thrust, initial guess trajectories. The new technique can be applied to any trajectory governed by the dynamics of the two-body problem, in particular to trajectories generated by a shaping method. The main aim is to use the initial guesses to lower the peak thrust magnitude. It is shown that in the majority of the cases, a lower thrust profile results in reduced Δv. It is to be stressed that the objective at this stage is not to optimise the initial guesses but to improve them in a computationally efficient manner by reducing peak thrust and total Δv. For this reason, the most is done to make use of analytical results. The technique relies on the linearisation of the equations of motion around the initial trajectory and assigning a quadratic cost function. Theoretical results are provided on the limits of validity of the linearisations. An important theorem is also derived in a series of steps, linking the L_2 optimality of the trajectories described with the linearised equations of motion with the L_2 optimality of the trajectories described with the original equations of motion. The new technique of improvement is tested with initial trajectories generated by the two shaping methods of the first chapter.

The third chapter presents an algorithm to prune out large search spaces arising in MGA trajectories. The method, based on the discretisation of the search space into a

grid, is particularly adapted to transfers that employ low thrust only. The trajectory generation and improvement techniques presented in the first two chapters can be used to design each leg of the MGA transfers. In order to avoid powered swingbys, a special technique is developed that links incoming and outgoing velocities. The retained trajectories of the pruned space are classified such that a discretised launch window is created with the best possible trajectory at each node. Several test cases are provided to prove the efficiency of the algorithm.

Mathematical results that are necessary or useful to support the main text of the thesis are provided in appendix, as well as the framework for a third type of shaping function, called hybrid shaping, which combines the features of both the spherical and pseudo-equinoctial shaping, but for which no shaping function was found so far that would result in thrust profiles low enough to be considered practical.

CHAPTER 2 LOW THRUST TRAJECTORY SHAPING

This chapter lays down the basic framework in which any trajectory shaping method can be described and analysed. An abstract mathematical formulation is constructed because it ensures rigor and generality. The two trajectory shaping methods that follow are formulated within that framework: a spherical shaping and a pseudo-equinoctial shaping. Numerous test cases are provided which prove the utility of the spherical shaping and the pseudo-equinoctial shaping. A shaping that can be considered hybrid between the first two is also presented in 5.2APPENDIX C. However, no result is given for the hybrid shaping due to the difficulty to find transfers with it with a Δv low enough.

2.1 General framework

The main motivation for the shaping method is to find solutions to a controlled dynamical system, satisfying some conditions on the state vector, by avoiding both the numerical integration of the equations of motion and the solution of an optimal control problem. The underlying idea is to first assign a parameterised shape to the state vector and then compute the control law. This process is normally known as an inverse control problem in aeronautics [35]. In mathematical terms, given the controlled dynamical system $\dot{\mathbf{x}} = f\left(\mathbf{x},\mathbf{u}\right)$ where $\mathbf{x} \in W$ and $\mathbf{u} \in \mathbb{R}^m$, m is the dimension of $\mathbf{u}$, n the dimension of $\mathbf{x}$ and $W \subset \mathbb{R}^n$, one needs to perform the inverse transformation:

$$\forall \mathbf{x} \in W, g_{\mathbf{x}} : \begin{cases} \Omega_{\mathbf{x}} \to \mathbb{R}^m \\ \dot{\mathbf{x}} \mapsto \mathbf{u} = g_{\mathbf{x}}\left(\dot{\mathbf{x}}\right) \end{cases} \tag{2.1}$$

such that the control law $\mathbf{u}$ is obtained as a function of the state vector $\mathbf{x}$ and its derivative $\dot{\mathbf{x}}$. In the following it is assumed that $m < n$ and $f_{\mathbf{x}}$ represents the function f when $\mathbf{x}$ is given. Note that $\mathbf{u} \in \mathbb{R}^m$, which means that no constraints on the control are applied at this stage.

One of the main issues when shaping the state vector **x** is the definition of the set $\Omega_{\mathbf{x}}$. In fact, a necessary condition to have a physical control vector **u** is that the image of $\mathbb{R}^m$ under $f_{\mathbf{x}}$ is included in $\Omega_{\mathbf{x}}$, or $\mathrm{Im} f_{\mathbf{x}} \subset \Omega_{\mathbf{x}}$, for all state vectors **x**, and the corresponding sufficient condition is that the function $g_{\mathbf{x}}$ is defined on $\Omega_{\mathbf{x}} = \mathrm{Im}(f_{\mathbf{x}})$. If $g_{\mathbf{x}}$ exists and is defined on $\Omega_{\mathbf{x}} = \mathrm{Im}(f_{\mathbf{x}})$ then the composition $g_{\mathbf{x}} \circ f_{\mathbf{x}}$ is bijective (both one-to-one and onto) and therefore $f_{\mathbf{x}}$ is injective (one-to-one) and $g_{\mathbf{x}}$ is surjective (onto). This property means that for the same state vectors, two different control vectors will yield different derivatives of the state vector, which will be easily verified in the scenarios presented later. In practice, given a coordinate system, a shaping method and a set of dynamic equations, it is required that $f_{\mathbf{x}}$ is surjective, and that $g_{\mathbf{x}}$ is defined on $\mathrm{Im}(f_{\mathbf{x}})$. If, furthermore, $g_{\mathbf{x}}$ is bijective, then the control law is unique.

The dynamical equations dealt with here are the ones describing the three dimensional motion of a spacecraft subject to the gravitational pull of a central body and to a controllable acceleration. The spacecraft and the central body are assumed to be point masses, with the mass of the spacecraft negligible compared to the one of the planet. The gravity constant of the central mass is denoted by μ. No assumption is made on the propulsion system: the thrust magnitude and the propellant consumption are obtained from the control law once an initial spacecraft mass and a value for the specific impulse are provided.

Independent of whether Cartesian, spherical coordinates, Keplerian or Equinoctial elements are used to parameterize the motion of the spacecraft, the equations of motion around the central body can be expressed as:

$$\dot{\mathbf{x}} = \mathbf{A}(\mathbf{x}) + \mathbf{B}(\mathbf{x})\mathbf{u} \tag{2.2}$$

with the number of states $n = 6$ and the number of controls $m = 3$. The space in which the state vectors **x** are defined, W, is an open subset of $\mathbb{R}^6$. Note that $f_{\mathbf{x}}$ in this case is affine. The physics of the problem are such that each of the three components of the control vector has an effect on the state vector, thus $f_{\mathbf{x}}$ is injective. $\mathrm{Im}(f_{\mathbf{x}})$ is a three dimensional manifold of $\mathbb{R}^6$, which can be defined by three equations of the type $\mathbf{C}_{\mathbf{x}}(\dot{\mathbf{x}}) = 0$. A general expression for $g_{\mathbf{x}}$ can be given by:

$$\mathbf{u} = \left[\mathbf{B}(\mathbf{x})^T \mathbf{B}(\mathbf{x})\right]^{-1} \mathbf{B}(\mathbf{x})^T \left[\dot{\mathbf{x}} - \mathbf{A}(\mathbf{x})\right] \tag{2.3}$$

Note that $\left[\mathbf{B}(\mathbf{x})^T \mathbf{B}(\mathbf{x})\right]^{-1} \mathbf{B}(\mathbf{x})^T$ is the Moore-Penrose pseudo-inverse of $\mathbf{B}(\mathbf{x})$. It will be shown that for all $\mathbf{x} \in W$, $\mathbf{B}(\mathbf{x})^T \mathbf{B}(\mathbf{x})$ is invertible and $g_{\mathbf{x}}$ is surjective since $g_{\mathbf{x}}$ is affine and each component of the control vector will be influenced by at least one component of $\dot{\mathbf{x}}$.

Finally, the particular type of dynamical system that will be considered in this document is described by a set of three second-order differential equations. In that case, three independent coordinates $\mathbf{q}$ and their respective derivatives $\dot{\mathbf{q}}$ define the state vector $\mathbf{x} = [\mathbf{q}^T, \dot{\mathbf{q}}^T]^T$. The vector $\mathbf{q}$ represents the state of the spacecraft in the configuration space expressed either in Cartesian or spherical coordinates.

Let us assume that the trajectory is parameterised by a variable *s*, defined on a closed interval $[s_i \; s_f]$ and that there is a smooth mapping, i.e. diffeomorphism, between the time *t* and *s*. Denoting by a prime the derivatives with respect to *s*, one would have the relationship $\dot{s}(s) = 1/t'(s)$ and $\ddot{s}(s) = -t''(s)/\left(t'(s)\right)^3$. Hence, the state vector becomes $\mathbf{x} = [\mathbf{q}^T, \dot{s}\mathbf{q}'^T]^T$ and the dynamical equations can be written as:

$$\dot{s}^2 \mathbf{q}'' + \ddot{s}\mathbf{q}' = \tilde{\mathbf{A}}\left(\mathbf{q}, \dot{s}\mathbf{q}'\right) + \tilde{\mathbf{B}}\left(\mathbf{q}, \dot{s}\mathbf{q}'\right)\mathbf{u} \tag{2.4}$$

such that **A** and **B** in (2.2) would be $\mathbf{A} = \left[\dot{\mathbf{q}}^T, \tilde{\mathbf{A}}^T\right]^T$ and $\mathbf{B} = \left[\mathbf{O}_{1\times 3}, \tilde{\mathbf{B}}^T\right]^T$.

This kind of reparameterisation was first used by Baumgarte in 1972 [36] for the purpose of stabilizing the numerical integration of equations of motion. The general formulation in Eqs. (2.3) and (2.4) will be translated into three specific shaping approaches in spherical coordinates and Cartesian coordinates.

2.2 Spherical shaping

This section is devoted to a newly developed shaping method based on the shaping of spherical coordinates. The method can be regarded as the generalisation of the approach used by Petropoulos with the exponential sinusoids [27] and of the shaping

in polar coordinates with inverse polynomials by Wall and Conway [29]. It will be shown that the latter two can be described within the framework of the spherical shaping.

The equations of motion are written in the radial-orthoradial-out-of-plane reference frame and the control vector is present through its components in the tangential-normal-out-of-plane frame. An important relationship is derived, whereby the magnitude of the velocity is related to the geometrical properties of the trajectory and to the normal component of the control vector. Assuming that the normal component of the control vector is zero, it will be shown that the physical trajectory and therefore velocity is completely defined by the pure geometry of the trajectory, without any consideration on the dynamical properties along the trajectory.

A scalar criterion on the geometry of the trajectory is derived such that a physically feasible trajectory exists with a solely tangential control profile.

Once the general setting of the spherical shaping is established, it can be applied to any particular analytical expression for the radius and the elevation angle as a function of the azimuthal angle, such that the aforementioned criterion is satisfied. In particular, an expression for the radius is used such that the uncontrolled Keplerian motion is covered, and the expression of the elevation angle approximates a linear evolution of the angular momentum vector when the inclination changes are small.

Finally, particular cases are addressed where some interesting physical properties are found.

2.2.1 Derivation of the spherical shaping method

The spherical shaping method describes the spatial properties of the trajectories using spherical coordinates.

The trajectory of the spacecraft in the three dimensional space is uniquely defined by the spherical coordinates $(r,\theta,\varphi) \in \mathbb{R}^+ \times \mathbb{R}/2\pi\mathbb{Z} \times \left(-\pi/2 + \mathbb{R}/\pi\mathbb{Z}\right)$, where r is the distance from the central body, θ is the azimuthal angle and φ is the elevation angle (see Fig. 2.1). In the following the two angular components of the coordinates will be allowed to have any real value, since there will be no necessity for a unique representation for positions. If the variation of the position is taken with respect to time, the state vector is $[r,\theta,\varphi,\dot{r},\dot{\theta},\dot{\varphi}]^T$.

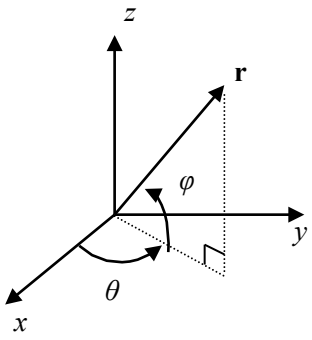

Fig. 2.1 Illustration of the spherical coordinate system

If, instead, the angle θ is taken as parameter s to parameterize the trajectory, then $r = R(\theta)$, $\varphi = \Phi(\theta)$ and $t = T(\theta)$. The transformation between t and θ holds if there is a smooth one-to-one mapping, also called diffeomorphism, between t and θ, which implies that θ is strictly monotonous with respect to time. The state vector becomes $\mathbf{x} = [r, t, \varphi, r', t', \varphi']^T$ where the prime represents the derivative with respect to $s = \theta$. This parameterisation is non-singular if the poles and the origin are excluded from the set of admissible positions. Moreover, the angle θ will account for the n_r revolutions of the trajectory. Hence, the space W is defined as:

$$W = \mathbb{R}_+^* \times \left[\theta_i \quad \theta_f + 2n_r\pi\right] \times \left(-\pi/2 \quad \pi/2\right) \times \mathbb{R}^3$$

The equations of motion in an inertial reference frame are:

$$\frac{d^2\mathbf{r}}{dt^2} = -\mu\frac{\mathbf{r}}{r^3} + \mathbf{u} \tag{2.5}$$

where the position vector is $\mathbf{r} = \left[r\cos\theta\cos\varphi, r\sin\theta\cos\varphi, r\sin\varphi\right]^T$. Since the position vector is parametrised with θ, then:

$$\dot{\theta}^2\frac{d^2\mathbf{r}}{d\theta^2} + \ddot{\theta}\frac{d\mathbf{r}}{d\theta} = -\mu\frac{\mathbf{r}}{r^3} + \mathbf{u} \tag{2.6}$$

with $\dot{\theta} = 1/t'$ and $\ddot{\theta} = -t''/t'^3$. Here $W = \mathbb{R}_+^* \times \left[t_i \quad t_f\right] \times \left(-\pi/2 \quad \pi/2\right) \times \mathbb{R}^3$. Finally, the control vector **u** is obtained straight from Eq. (2.6), after having inserted the expression of **r** as a function of the spherical coordinates.

2.2.2 Properties of the trajectory of a tangentially controlled spacecraft

If the geometrical trajectory is given, then one still needs to set the evolution of the spacecraft along that trajectory in order to define completely the physical transfer. This is done by providing $\dot{\theta}$ as a function of θ. Then one also has $\ddot{\theta}$, and through (2.6), the control profile **u** is extracted. Therefore, if the shape of a trajectory is fixed, only one degree of freedom remains for defining the transfer completely. However, it is not straightforward to set the time evolution a priori, such that the final control profile is systematically low, or even close to optimal.

In this section a simple relationship will be established between $\dot{\theta}$ and the normal component of **u**, in the tangential-normal-out-of-plane frame. This relationship turns out to be useful to set a "shape" for the time evolution t based on physical considerations.

The velocity vector **v** is expressed as:

$$\mathbf{v} = \frac{d\mathbf{r}}{dt} = \dot{\theta}\frac{d\mathbf{r}}{d\theta} \tag{2.7}$$

and the acceleration vector **a** as:

$$\mathbf{a} = \frac{d\mathbf{v}}{dt} = \ddot{\theta}\frac{d\mathbf{r}}{d\theta} + \dot{\theta}^2\frac{d^2\mathbf{r}}{d\theta^2} \tag{2.8}$$

In the following, the vectors $d\mathbf{r}/d\theta$ and $d^2\mathbf{r}/d\theta^2$ will be denoted by $\tilde{\mathbf{v}}$ and $\tilde{\mathbf{a}}$ respectively. They are entirely described by the geometry of the trajectory and therefore by r, φ and their first and second derivatives with respect to the azimuthal angle. The vector $\tilde{\mathbf{h}} = \mathbf{r} \wedge \tilde{\mathbf{v}}$ is also introduced, its magnitude is noted $\tilde{h}$.

The unit vectors $(\mathbf{e}_t, \mathbf{e}_n, \mathbf{e}_h)$ defining the tangential-normal-out-of-plane reference frame are introduced and the equations of motion (2.6) are projected onto it:

$$\mathbf{u} = \begin{pmatrix} u_t \\ u_n \\ u_h \end{pmatrix} = \begin{pmatrix} \frac{\mu}{r^2}\mathbf{e}_r \cdot \mathbf{e}_t + \ddot{\theta}\tilde{\mathbf{v}} \cdot \mathbf{e}_t + \dot{\theta}^2 \tilde{\mathbf{a}} \cdot \mathbf{e}_t \\ \frac{\mu}{r^2}\mathbf{e}_r \cdot \mathbf{e}_n + \dot{\theta}^2 \tilde{\mathbf{a}} \cdot \mathbf{e}_n \\ \dot{\theta}^2 \tilde{\mathbf{a}} \cdot \mathbf{e}_h \end{pmatrix} \tag{2.9}$$

The second and the third component of **u** in (2.9) are of interest because they only involve $\dot{\theta}^2$ while $\ddot{\theta}$ is absent. The projection on the out-of-plane component does not provide much information. However, since $\mathbf{e}_n = \mathbf{e}_h \wedge \mathbf{e}_t$, the normal component of **u** can be rewritten as:

$$u_n = \frac{\mu}{r^2}\mathbf{e}_r \cdot \mathbf{e}_n + \dot{\theta}^2 \frac{\tilde{\mathbf{a}} \cdot \left(\tilde{\mathbf{h}} \wedge \tilde{\mathbf{v}}\right)}{\tilde{h}\tilde{v}} \tag{2.10}$$

At this stage the flight path angle γ is introduced, which is the angle between the velocity vector and the local horizon. An illustration is provided in Fig. 2.2.

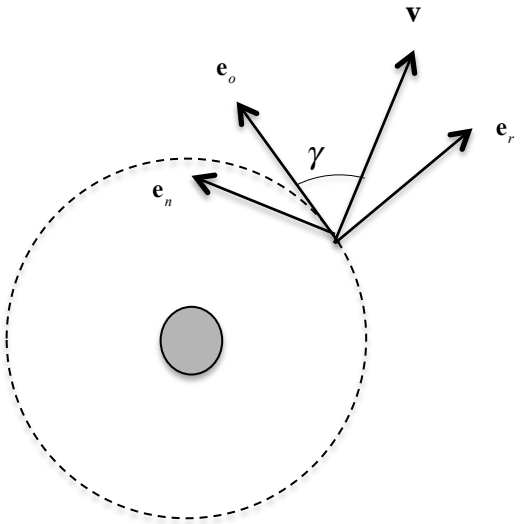

Fig. 2.2 Illustration of the flight path angle. The local horizon is tangent to the dashed circle

One obtains then $\mathbf{e}_r \cdot \mathbf{e}_n = -\cos\gamma$ and $\tilde{h} = r\tilde{v}\cos\gamma$, one obtains:

$$D\dot{\theta}^2 = \frac{\mu}{r^2} + \frac{u_n}{\cos\gamma} \tag{2.11}$$

where

$$D = \frac{r}{\tilde{h}^2}\tilde{\mathbf{a}} \cdot \left(\tilde{\mathbf{h}} \wedge \tilde{\mathbf{v}}\right) \tag{2.12}$$

This expression depends uniquely on R, R', R'', Φ, Φ' and Φ'', so on the pure geometrical shape of the trajectory. Finally, if one uses the physical velocity **v**, acceleration **a** and angular momentum **h**, then:

$$\begin{aligned} \mathbf{a} \cdot \left(\mathbf{h} \wedge \mathbf{v}\right) &= \left(\ddot{\theta}\tilde{\mathbf{v}} + \dot{\theta}^2\tilde{\mathbf{a}}\right) \cdot \left(\dot{\theta}\tilde{\mathbf{h}} \wedge \dot{\theta}\tilde{\mathbf{v}}\right) \\ &= \dot{\theta}^4 \tilde{\mathbf{a}} \cdot \left(\tilde{\mathbf{h}} \wedge \tilde{\mathbf{v}}\right) \end{aligned} \tag{2.13}$$

and D can then be rewritten as:

$$D = \frac{r}{\dot{\theta}^2 h^2}\mathbf{a} \cdot \left(\mathbf{h} \wedge \mathbf{v}\right) \tag{2.14}$$

The quantity D has the sign of $\mathbf{a} \cdot \left(\mathbf{h} \wedge \mathbf{v}\right)$, which is the same as the sign of $\tilde{\mathbf{a}} \cdot \left(\tilde{\mathbf{h}} \wedge \tilde{\mathbf{v}}\right)$, thus D is positive when the trajectory is curved towards the central body. One can exhibit the symmetry within the expression of D by reformulating (2.12) as:

$$\frac{D}{r} = \frac{\tilde{\mathbf{a}} \cdot \left(\tilde{\mathbf{h}} \wedge \tilde{\mathbf{v}}\right)}{\tilde{h}^2} = \frac{\mathbf{r}'' \cdot \left(\left(\mathbf{r} \wedge \mathbf{r}'\right) \wedge \mathbf{r}'\right)}{\left\|\mathbf{r} \wedge \mathbf{r}'\right\|^2} = \frac{\left(\mathbf{r} \wedge \mathbf{r}'\right) \cdot \left(\mathbf{r}' \wedge \mathbf{r}''\right)}{\left\|\mathbf{r} \wedge \mathbf{r}'\right\|^2} = \frac{\left(\mathbf{r} \cdot \mathbf{r}'\right)\left(\mathbf{r}' \cdot \mathbf{r}''\right) - r'^2\left(\mathbf{r} \cdot \mathbf{r}''\right)}{r^2 r'^2 - \left(\mathbf{r} \cdot \mathbf{r}'\right)^2} \tag{2.15}$$

The scalar D is independent of the reference frame, and can be expressed using the components of the position, velocity and acceleration in any one reference frame. Using the radial-orthoradial-out-of-plane coordinate system $(\mathbf{e}_r, \mathbf{e}_o, \mathbf{e}_h)$, one has $\tilde{v}_h = 0$, such that:

$$D = \frac{\tilde{v}_r \tilde{a}_o - \tilde{v}_o \tilde{a}_r}{\tilde{v}_o} \tag{2.16}$$

It is shown in appendix that $\tilde{\mathbf{v}}$ and $\tilde{\mathbf{a}}$ are written in $(\mathbf{e}_r, \mathbf{e}_o, \mathbf{e}_h)$ as

$$\tilde{\mathbf{v}} = \begin{pmatrix} \tilde{v}_r \\ \tilde{v}_o \\ \tilde{v}_h \end{pmatrix} = \begin{pmatrix} r' \\ r\sqrt{\varphi'^2 + \cos^2\varphi} \\ 0 \end{pmatrix} \tag{2.17}$$

$$\tilde{\mathbf{a}} = \begin{pmatrix} \tilde{a}_r \\ \tilde{a}_o \\ \tilde{a}_h \end{pmatrix} = \begin{pmatrix} r'' - r\left(\varphi'^2 + \cos^2\varphi\right) \\ 2r'\sqrt{\varphi'^2 + \cos^2\varphi} + r\varphi' \dfrac{\varphi'' - \sin\varphi\cos\varphi}{\sqrt{\varphi'^2 + \cos^2\varphi}} \\ \dfrac{r}{\sqrt{\varphi'^2 + \cos^2\varphi}}\left(\cos\varphi\left(\varphi'' - \sin\varphi\cos\varphi\right) + 2\sin\varphi\left(\varphi'^2 + \cos^2\varphi\right)\right) \end{pmatrix} \tag{2.18}$$

The expression for D becomes then:

$$D = -r'' + 2\frac{r'^2}{r} + r'\varphi' \frac{\varphi'' - \sin\varphi\cos\varphi}{\varphi'^2 + \cos^2\varphi} + r\left(\varphi'^2 + \cos^2\varphi\right) \tag{2.19}$$

The functions R, Φ and T are introduced as the shaping functions of r, φ and t respectively and the corresponding control profile can be obtained, along with the Δv and the propellant consumption if the spacecraft's initial mass and specific impulse are provided. R and Φ model the pure geometry of the trajectory, while T shapes the time evolution along the trajectory. It is assumed that the shaping functions R, Φ and T belong to sets of admissible functions S_R, S_Φ and S_T that are twice continuously differentiable. Now, if the function T, defined through its derivative:

$$T' = \sqrt{\frac{DR^2}{\mu}} \tag{2.20}$$

is used to shape t, then from Eq. (2.11) it can be seen that the control vector corresponding to the geometrical trajectory defined by R and Φ will have no component out of the tangential plane to the trajectory (i.e. $u_n = 0$). This is an important novel result: no matter how the trajectory is shaped, there is no normal component to the control vector if and only if the satellite evolves along the trajectory according to (2.20).

Note that shaping of the derivative T' instead of T is not an issue because the origin of time can be set as an additive constant to T. Eq. (2.20) requires the condition $D > 0$ in order to have a real time of flight. Geometrically speaking, this means that the plane defined by **v** and **h** (or in other words by the admissible control vectors) divides the space in two, and the trajectory must be curved towards the half-space containing the center of gravity. In fact, if the acceleration vector pointed towards the opposite half-space, a control component outside of the separating plane would be

required to balance the gravitational pull of the central body, therefore $u_n \neq 0$ (see Fig. 2.3).

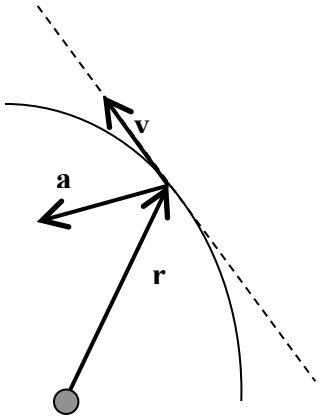

Fig. 2.3 Illustration in 2D of the condition *D > 0*. The trajectory is the arc, the velocity vector is aligned with the tangent (dashed line).

The time of flight and the Δv corresponding to the shaped trajectory are obtained by integrating respectively T' and $|\mathbf{u}|T'$ over the interval $\left[\theta_i \;\; \theta_f + 2n_r\pi\right]$.

It should be noted that by shaping the time evolution T with the expression in Eq. (2.20), R and Φ define completely T' and the time of flight $T(\theta_f) - T(\theta_i)$. This can be problematic when a constraint on the time of flight exists. However it is generally difficult to shape a priori T in such a way to obtain a control that is not too far from optimal, i.e. interesting in practice. Using such an expression for T' will result, for certain transfers, in reasonable thrust profiles and Δv.

2.2.3 Particular case of planar trajectories

Planar trajectories have already been addressed in the literature and the corresponding models are, as expected, technically less cumbersome. However, the problem has not been approached using the present the vectorial framework. The general three-dimensional model is simplified to two dimensions here and interesting relationships are found, which, when applied to existing models in the literature, go further in the physical understanding of the models and the predictions they enable.

The spherical coordinate system and the radial-orthoradial-out-of-plane one become confounded in the 2D model and are commonly called polar coordinate system. The basis of the system is denoted by $(\mathbf{e}_r, \mathbf{e}_\theta)$.

After reducing the three dimensional model, the velocity and acceleration from (2.17) and (2.18) become

$$\tilde{\mathbf{v}} = \begin{pmatrix} \tilde{v}_r \\ \tilde{v}_\theta \end{pmatrix} = \begin{pmatrix} r' \\ r \end{pmatrix} \tag{2.21}$$

$$\tilde{\mathbf{a}} = \begin{pmatrix} \tilde{a}_r \\ \tilde{a}_\theta \end{pmatrix} = \begin{pmatrix} r'' - r \\ 2r' \end{pmatrix} \tag{2.22}$$

D in expression (2.11) linking the dynamics along the trajectory with the normal component of the control vector has now the simpler expression

$$D = \frac{\tilde{v}_r \tilde{a}_\theta - \tilde{v}_\theta \tilde{a}_r}{\tilde{v}_\theta} = r - r'' + 2\frac{r'^2}{r} = \frac{r^{-1} + \left(r^{-1}\right)''}{\left(r^{-1}\right)^2} \tag{2.23}$$

If one introduces the signed curvature c defined by [37]:

$$c = \frac{r^2 + 2r'^2 - rr''}{\left(r^2 + r'^2\right)^{3/2}} = \frac{rD}{\left\|\tilde{\mathbf{v}}\right\|^3} \tag{2.24}$$

then one obtains another expression for D:

$$D = \frac{c\left\|\tilde{\mathbf{v}}\right\|^3}{r} \tag{2.25}$$

The latter equation shows that D has the sign of the curvature. Therefore, a spacecraft can stay on a prescribed trajectory using only tangential thrust as long as the trajectory bends towards the central body.

A simple expression can be obtained for the osculating semi-latus rectum p. It is linked to the norm h of the angular velocity vector by $p = h^2 / \mu = r^4 / \mu t'^2$. If the radius is shaped by a function R and if it is assumed that the thrust is tangential, in which case the time evolution is shaped as in Eq. (2.20), then the semi-latus rectum becomes $p = R^2 / D$. Using Eq. (2.23) one gets:

$$p = \frac{1}{R^{-1} + \left(R^{-1}\right)''} \tag{2.26}$$

The semi-latus rectum is a positive quantity so the previous formula is valid only if $D > 0$. Otherwise the assumption of having only tangential thrust is incompatible with the shape of the trajectory defined by R.

Finally, a result can be found on the range of eccentricities that can be reached by the osculating orbits, when the transfer is planar and the control vector is assumed to be tangential. The osculating eccentricity is defined by the osculating semi-latus rectum and the osculating semi-major axis a:

$$e = \sqrt{1 - \frac{p}{a}} \tag{2.27}$$

The energy of the spacecraft is defined by:

$$E = -\frac{\mu}{2a} = \frac{\mathbf{v}^2}{2} - \frac{\mu}{r} \tag{2.28}$$

therefore the eccentricity becomes

$$e = \sqrt{1 + \frac{2p}{\mu}\left(\frac{\mathbf{v}^2}{2} - \frac{\mu}{r}\right)} = \sqrt{1 + \frac{2p}{\mu}\left(\frac{\tilde{\mathbf{v}}^2}{2t'^2} - \frac{\mu}{r}\right)} \tag{2.29}$$

If the planar trajectory is shaped by R and the control vector is tangential, by using (2.20), (2.21) and (2.26) and after some algebraic manipulations, the following expression is obtained:

$$e = \sqrt{\frac{\left(R^{-1}\right)'^2 + \left(R^{-1}\right)''^2}{\left(R^{-1} + \left(R^{-1}\right)''\right)^2}} \tag{2.30}$$

The result is reassuring in the sense that the eccentricity is always defined because it is the root of a positive number. It is easy to verify the formula by observing that the eccentricity is zero if and only if R is constant. Moreover, the eccentricity is not defined when the function $R^{-1} + \left(R^{-1}\right)''$ takes the value zero. This corresponds to the case when the curvature of the trajectory is zero.

In the next two sections the shaping approaches of Petropoulos and Wall and Conway will be revisited in the light of the generalised three-dimensional spherical model. The two methods describe trajectories in 2 dimensions only and Petropoulos's and Wall and Conway's shaping can be obtained from the novel spherical shaping method which is valid in 3 dimensions.

2.2.4 The exponential shaping of Petropoulos

In 2000 Petropoulos et al. [27] proposed the use of a two dimensional shape, expressed in polar coordinates, for low thrust trajectory design. The radius takes the following form:

$$R(\theta) = k_0 \exp\left(k_1 \sin\left(k_2\theta + \phi\right)\right) \tag{2.31}$$

A tangential thrust is assumed along the trajectory and, according to the theory developed for the three dimensional spherical model, this is possible only if the quantity D defined in Eq. (2.23) is strictly positive. If one inserts Eq. (2.31) into the expression of D and remembers that R is strictly positive, then the following inequality condition is obtained:

$$\frac{D}{R} = 1 + k_1 k_2^2 \sin\left(k_2\theta + \phi\right) + k_1^2 k_2^2 \cos^2\left(k_2\theta + \phi\right) > 0 \tag{2.32}$$

The above inequality must hold for all θ, and in particular for $\theta_1 = -(\phi + \pi/2)/k_2$ and $\theta_2 = -(\phi - \pi/2)/k_2$, in which case we get the two inequalities $-1 < k_1 k_2^2 < 1$, or in a compact form $|k_1| k_2^2 < 1$. Reciprocally, if $|k_1| k_2^2 < 1$, then one easily gets that D is strictly positive for all θ.

Petropoulos and Longuski found solutions to the two-point boundary value problem by tuning the value of k_2 such that the spiral intersects the target orbit at the right time, without necessarily matching the velocities at the boundaries [38]. Izzo [39] studied the Lambert problem for the exponential sinusoids and found that it could be solved for certain ranges of time of flight that depend on the initial flight path angles. Therefore, this method cannot satisfy all possible boundary conditions on position and velocity without an additional impulsive Δv at the tips.

2.2.5 The inverse polynomials of Wall and Conway

Wall and Conway [20] devised a shape-based method similar to Petropoulos, with the difference that they used inverse polynomials to model the radius instead of an exponential sinusoid. Their expression of R contains more free parameters such that the boundary conditions on both position and velocity can be accommodated. An additional parameter in R is used to satisfy the time of flight constraints. The function R has the form:

$$R = \frac{1}{a_0 + a_1\theta + a_2\theta^2 + a_3\theta^3 + a_4\theta^4 + a_5\theta^5 + a_6\theta^6} \tag{2.33}$$

The expression in Eq. (2.33) provides feasible transfers if and only if, for all θ, $R > 0$. This condition depends on the values of the coefficients and therefore on the boundary conditions and the required time of flight. One more condition to be satisfied for all θ is $D > 0$, otherwise no tangential control would be admissible with the given shape of the trajectory. From (2.23), $D > 0$ if $R^{-1} + \left(R^{-1}\right)'' > 0$, which translates into $\forall \theta \in \left[\theta_i ; \theta_f + 2n_r\pi\right]$:

$$\left(a_0 + 2a_2\right) + \left(a_1 + 6a_3\right)\theta + \left(a_2 + 12a_4\right)\theta^2 + \left(a_3 + 20a_5\right)\theta^3 + \left(a_4 + 30a_6\right)\theta^4 + a_5\theta^5 + a_6\theta^6 > 0 \tag{1.34}$$

If one uses the inverse polynomials for one particular trajectory only, then (2.34) is a necessary and sufficient conditions for the trajectory to be feasible with only tangential thrust. If one uses the same shaping for any planar transfer with any number of revolutions, then Eq. (2.34) must be valid on $\mathbb{R}^+$. Note that one necessary condition for this to hold true is $a_6 > 0$. Finally, the 6th degree polynomial in the expression of R can have at most 5 extrema. Therefore, if one models a transfer between two elliptical orbits using 3 revolutions or more, these inverse polynomials would not be able to model oscillations of the radius between successive pericenters and apocenters. If one uses a succession of these shaping functions then the latter deficiency is clearly removed.

2.2.6 Particular case of trajectories with constant radius

This case is addressed because the equations simplify a lot and interesting results can be extracted from the model. It is assumed that R is a constant function that takes the value R_0. The spacecraft moves on the sphere of radius R_0, $\tilde{v}_r = 0$ and the flight path angle γ is zero. However the radial acceleration is not zero because an acceleration along the radial direction is necessary in order to stay on the surface of the sphere.

From (2.16) one gets $D = -\tilde{a}_r$, so

$$D = R_0\left(\Phi'^2 + \cos^2\Phi\right) \tag{2.35}$$

The tangential-normal-out-of-plane frame and radial-orthoradial-out-of-plane frame are confounded, so assuming a control profile without a normal component is equivalent to assuming that the control direction is tangential to the sphere on which the spacecraft moves. In that case, the time evolution is written as:

$$T' = \sqrt{\frac{R_0^3}{\mu}\left(\Phi'^2 + \cos^2\Phi\right)} \tag{2.36}$$

The time of flight is the sum of T' along the trajectory and the following time equation is obtained:

$$\Delta T = \sqrt{\frac{R_0^3}{\mu}}\int_{\theta_i}^{\theta_i}\sqrt{\Phi'^2 + \cos^2\Phi}\,d\theta = n\int_{\theta_i}^{\theta_i}\sqrt{d\Phi^2 + d\theta^2\cos^2\Phi} = n\Delta\Theta \tag{2.37}$$

Θ is the arc length associated to the trajectory divided by the radius, so it can be considered as an 'angular length'. What is remarkable is that the angular velocity stays constant and is that of a Keplerian circular orbit of radius R_0. Hence the velocity of the spacecraft is constant. Indeed, Eq. (2.37) can be rewritten as:

$$\Delta T = \sqrt{\frac{R_0}{\mu}}\int_{\Theta_i}^{\Theta_f} R_0\,d\Theta = \frac{1}{v_0}\int_{l_i}^{l_f} dl = \frac{\Delta l}{v_0} \tag{2.38}$$

The consequence of this is that the kinetic energy of the spacecraft is constant, so the thrust does not provide work. The result is that the control vector can only be directed normally to the osculating orbital plane. This makes physical sense, because if a spacecraft were initially left on a circular orbit and had to change its trajectory by always staying on the sphere of the same radius as the initial orbit, then it would go through a succession of intermediate circular orbits, and for doing that, small amounts of Δvs orthogonal to the orbital plane are required.

It is possible to apply the results above to the case of a spacecraft that orbits on a circular orbit displaced towards one of the poles. In other words, the subsatellite point stays at a constant latitude Φ_0.

2.2.7 Application of the general framework to particular shaping functions

R and Φ can be in any function space such that $R>0$ and $-\pi/2<\Phi<\pi/2$, but it is judicious to choose expressions for which the boundary constraints on the position and velocity can be imposed analytically. The boundary conditions are:

$$\begin{cases} R(\theta_i)=R_i & , \quad R(\theta_f+2n_r\pi)=R_f \\ \Phi(\theta_i)=\Phi_i & , \quad \Phi(\theta_f+2n_r\pi)=\Phi_f \\ T'(\theta_i)=\dfrac{R_i\cos\Phi_i}{v_{\theta i}} & , \quad T'(\theta_f+2n_r\pi)=\dfrac{R_f\cos\Phi_f}{v_{\theta f}} \\ R'(\theta_i)=v_{ri} & , \quad R'(\theta_f+2n_r\pi)=v_{rf} \\ \Phi'(\theta_i)=\dfrac{v_{\varphi i}}{R_i} & , \quad \Phi'(\theta_f+2n_r\pi)=\dfrac{v_{\varphi f}}{R_f} \end{cases} \tag{2.39}$$

It is assumed at this stage that the control vector has no normal component, such that T' satisfies (2.20). The boundary conditions on T' are expressed as the boundary conditions on R and Φ and their first and second derivatives. Then linear constraints on R'' and Φ'' are found using the expression for D in (2.19) and (2.20):

$$\begin{cases} R''(\theta_i)+\alpha_i\Phi''(\theta_i)=C_i \\ R''(\theta_f)+\alpha_f\Phi''(\theta_f)=C_f \end{cases} \tag{2.40}$$

where

$$\alpha_{i/f} = -\frac{R'\Phi'\left(\theta_{i/f}\right)}{\Phi'^2\left(\theta_{i/f}\right)+\cos^2\Phi\left(\theta_{i/f}\right)} = -\frac{v_{ri/f}v_{\varphi i/f}}{R_{i/f}\left(v_{\varphi i/f}^2/R_{i/f}^2+\cos^2\Phi_{i/f}\right)} \tag{2.41}$$

and

$$\begin{aligned} C_{i/f} &= -\frac{\mu T'^2\left(\theta_{i/f}\right)}{R_{i/f}^2}+2\frac{R_{i/f}'^2}{R_{i/f}}+R_{i/f}\left(\Phi'^2\left(\theta_{i/f}\right)+\cos^2\Phi\left(\theta_{i/f}\right)\right)-R_{i/f}'\Phi'\left(\theta_{i/f}\right)\frac{\sin\Phi\left(\theta_{i/f}\right)\cos\Phi\left(\theta_{i/f}\right)}{\Phi'^2\left(\theta_{i/f}\right)+\cos^2\Phi\left(\theta_{i/f}\right)} \\ &= -\frac{\mu\cos^2\Phi_{i/f}}{v_{\theta i/f}^2}+2\frac{v_{ri/f}^2}{R_{i/f}}+R_{i/f}\left(\frac{v_{\varphi i/f}^2}{R_{i/f}^2}+\cos^2\Phi_{i/f}\right)-\frac{v_{ri/f}v_{\varphi i/f}}{R_{i/f}}\frac{\sin\Phi_{i/f}\cos\Phi_{i/f}}{\frac{v_{\varphi i/f}^2}{R_{i/f}^2}+\cos^2\Phi_{i/f}} \end{aligned} \tag{2.42}$$

There are therefore ten boundary conditions: four on the radius, four on the elevation angle and two combined between the two. Thus, the functions R and Φ must have at least 10 free parameters altogether to satisfy all boundary conditions, with at least four for R and four for Φ. In three dimensions, one would expect to have a total of 12 boundary conditions, the last two would be $t\left(\theta_i\right)=t_i$ and $t\left(\theta_f\right)=t_f$. These two can be imposed as design constraints, however if one fixes T' as in (2.20), then the time of flight t_f-t_i is fixed by the shaping functions R and Φ.

2.2.8 Choice of the shaping functions and analytical resolution of the boundary constraints

This section shows that a relatively wide set of shaping functions for R and Φ can be used such that the boundary conditions can be satisfied analytically. The boundary conditions expressed in (2.39) and (2.40) suggest that functions of the form $R(\theta)=\sum_{k=1}^{n}a_kR_k(\theta)$ and $\Phi(\theta)=\sum_{k=1}^{m}b_k\Phi_k(\theta)$ are interesting because their derivatives remain linear combinations of the unknown coefficients and therefore the boundary conditions can be solved by inverting a 10 by 10 matrix. Note that one needs to have $n\geq 4$, $m\geq 4$ and $n+m=10$.

However there is a wider set of functions that allow satisfying constraints in such a way. If one considers those functions that can be written as $R(\theta)=R_0\left(\sum_{k=1}^{n}a_kR_k(\theta)\right)$ and

$\Phi(\theta)=\Phi_0\left(\sum_{i=1}^{m} b_k\Phi_k(\theta)\right)$, where R_0 and Φ_0 can be analytically inverted, then it can be shown that the coefficients can be solved for analytically as well. Indeed, in that case, first the boundary conditions on R and Φ need to be rewritten as $\sum_{k=1}^{n} a_k R_k\left(\theta_{i/f}\right)=R_0^{-1}\left(R_{i/f}\right)$ and $\sum_{i=1}^{m} b_k\Phi_k\left(\theta_{i/f}\right)=\Phi_0^{-1}\left(\Phi_{i/f}\right)$, those on R' and Φ' become:

$$\begin{aligned}\sum_{k=1}^{n} a_k R_k'\left(\theta_{i/f}\right)&=\frac{v_{ri/f}}{R_0'\left(\sum_{k=1}^{n} a_k R_k\left(\theta_{i/f}\right)\right)}=\frac{v_{ri/f}}{R_0'\left(R_0^{-1}\left(R_{i/f}\right)\right)}\\ \sum_{i=1}^{m} b_k\Phi_k'\left(\theta_{i/f}\right)&=\frac{v_{\varphi i/f}/R_{i/f}}{\Phi_0'\left(\sum_{i=1}^{m} b_k\Phi_k\left(\theta_{i/f}\right)\right)}=\frac{v_{\varphi i/f}/R_{i/f}}{\Phi_0'\left(\Phi_0^{-1}\left(\Phi_{i/f}\right)\right)}\end{aligned} \tag{2.43}$$

Finally the boundary conditions on T' in (2.40), where the second derivatives of R and Φ are present, become

$$\begin{aligned}&\sum_{k=1}^{n} a_k R_k''\left(\theta_{i/f}\right)\cdot R_0'\left(\sum_{k=1}^{n} a_k R_k\left(\theta_{i/f}\right)\right)+\left(\sum_{k=1}^{n} a_k R_k'\left(\theta_{i/f}\right)\right)^2\cdot R_0''\left(\sum_{k=1}^{n} a_k R_k\left(\theta_{i/f}\right)\right)\\ &+\alpha_{i/f}\left(\sum_{i=1}^{m} b_k\Phi_k''\left(\theta_{i/f}\right)\cdot\Phi_0'\left(\sum_{i=1}^{m} b_k\Phi_k\left(\theta_{i/f}\right)\right)+\left(\sum_{i=1}^{m} b_k\Phi_k'\left(\theta_{i/f}\right)\right)^2\cdot\Phi_0''\left(\sum_{i=1}^{m} b_k\Phi_k\left(\theta_{i/f}\right)\right)\right)=C_{i/f}\end{aligned} \tag{2.44}$$

and after rearranging, the following linear equations are obtained:

$$\begin{aligned}&\sum_{k=1}^{n} a_k R_k''\left(\theta_{i/f}\right)\cdot R_0'\left(R_0^{-1}\left(R_{i/f}\right)\right)+\alpha_{i/f}\sum_{i=1}^{m} b_k\Phi_k''\left(\theta_{i/f}\right)\cdot\Phi_0'\left(\Phi_0^{-1}\left(\Phi_{i/f}\right)\right)=\\ &=C_{i/f}-\frac{v_{ri/f}^2}{R_0'\left(R_0^{-1}\left(R_{i/f}\right)\right)^2}\cdot R_0''\left(R_0^{-1}\left(R_{i/f}\right)\right)-\alpha_{i/f}\frac{v_{\varphi i/f}^2/R_{i/f}^2}{\Phi_0'\left(\Phi_0^{-1}\left(\Phi_{i/f}\right)\right)^2}\cdot\Phi_0''\left(\Phi_0^{-1}\left(\Phi_{i/f}\right)\right)\end{aligned} \tag{2.45}$$

Therefore one has a relatively wide array of possibilities for the shaping functions and boundary conditions on position and velocity can be satisfied by inverting a 10 by 10 matrix.

One is not obliged to constrain the tips of the transfer both on position and velocity. Indeed, with the aforementioned form for the shaping functions, one has the flexibility to impose any combination of constraints within (2.39). For example it is possible to impose the initial and arrival position and only the arrival velocity. In that case the number of coefficients to be determined in R will be lower by two and in Φ by one. The number of coefficients can also be increased by adapting the shaping

functions and solving for additional constraints like the time of flight or maximum thrust.

2.2.9 Selection of the function shaping the radius

At this point it is possible to use any shaping function that has the form described above, but the expression has to be judiciously chosen, otherwise the trajectory would be curved badly and normal thrust would be required to stay on it, or the corresponding control profile would result in unacceptably high magnitudes and Δvs.

Considering that the Keplerian motion described in polar coordinates satisfies

$$r = \frac{p}{1 + e\cos(\theta - \omega)} \tag{2.46}$$

where ω is the argument of pericenter, the following expression is promising to be suitable for the shaping function R:

$$R(\theta) = \frac{1}{\alpha(\theta) + \beta(\theta)\cos\theta + \gamma(\theta)\sin\theta} \tag{2.47}$$

The above expression covers the case of the Keplerian motion, which corresponds to the case when the coefficients are constant, i.e. the initial and final boundary conditions are such that the Keplerian elements are constant.

It must be noted that in the particular case of planar transfers, the osculating semi-latus rectum and eccentricity are not obtained directly from (2.47) as being $p = 1/\alpha$ and $e = \sqrt{\beta^2 + \gamma^2}/\alpha$, because if it were the case, then they would only take into account the geometry of the trajectory and not the physical velocity as well. The osculating semi-latus rectum is obtained from Eq. (2.26).

For the particular transfers defined by Eq. (2.47), the following equation is obtained:

$$\frac{1}{p} = \alpha + \alpha'' + (\beta'' + 2\gamma')\cos\theta + (\gamma'' - 2\beta')\sin\theta \tag{2.48}$$

Therefore the osculating semi-latus rectum, in the particular case of tangential thrust, is not, in general $p = 1/\alpha$. It can be shown that the latter is the case if and only if *R* has the expression

$$R(\theta) = \frac{1}{a_0 + a_1\theta + b_0\cos\theta + c_0\sin\theta} \tag{2.49}$$

In that case, the semi-latus rectum will be $p = 1/(a_0 + a_1\theta)$, and it will always be strictly positive once a_0 and a_1 are set by the boundary conditions.

Keeping the expression in (2.49) for *R* would leave four degrees of freedom to define a transfer. That is not enough if initial and final boundary conditions need to be set for both position and velocity, so at least two more free parameters are required. Hence the following form has been chosen for *R*:

$$R = \frac{1}{a_0 + a_1\theta + a_2\theta^2 + (a_3 + a_4\theta)\cos\theta + (a_5 + a_6\theta)\sin\theta} \tag{2.50}$$

The coefficient a_2 is set to *0* by default, but it can be used as an additional degree of freedom to satisfy other constraints on the transfer.

2.2.10 Choice of the shaping functions

In the presented test cases, S_R is the set of functions expressed in a form that is reminiscent of the expression of the radius in Keplerian elements, and S_Φ is such that Φ oscillates:

$$\begin{cases} R = \dfrac{1}{a_0 + a_1\theta + a_2\theta^2 + (a_3 + a_4\theta)\cos\theta + (a_5 + a_6\theta)\sin\theta} \\ \Phi = (b_0 + b_1\theta)\cos\theta + (b_2 + b_3\theta)\sin\theta \end{cases} \tag{2.51}$$

The motivation for this choice is that the minimum-thrust arc is the Keplerian arc. Moreover, the proposed expression for *R* can account for oscillations of the radius between pericenter and apocenter. No singularity was encountered for *R* in the test cases of this document, the value for the radius remained strictly positive. In the same

way, Φ always remained in the interval $(-\pi/2;\pi/2)$. The choice of the expression for Φ is motivated in detail in 5.2APPENDIX B and covers the case of Keplerian arcs.

Note that, in (2.51), the total number of free parameters is 11 and not 10. The extra parameter can be used as an additional degree of freedom to modify the shape of the trajectory. It can for instance be used to satisfy a constraint on the time of flight.

However, if fewer boundary conditions are imposed on the trajectory, the number of coefficients to fix would be lower, and some would be fixed to a default value of zero. For example, if one intends to impose only the initial position, the initial velocity and the final position, then four coefficients should be fixed for R and three for Φ. In this particular case, the R and Φ could have the following expression:

$$\begin{cases} R = \dfrac{1}{a_0 + a_1\theta + a_2\cos\theta + a_3\sin\theta} \\ \Phi = (b_0 + b_1\theta)\cos\theta + b_2\sin\theta \end{cases} \tag{2.52}$$

The boundary conditions would be solved using the appropriate subset of equations in (2.39), after using the expression of T' in (2.20).

2.3 Pseudo-equinoctial shaping

In 2006, De Pascale and Vasile proposed a different shaping approach based on the variation of the orbital elements [29]. Their shaping approach makes use of a set of pseudo-equinoctial elements to shape the Cartesian coordinates. Here, the pseudo-equinoctial shaping is revisited in the general framework laid out in section 2.1. The equations of motion used to calculate the control vector are the same as Eqs. (2.6). The expression of the equinoctial elements with respect to the Keplerian elements $(a \quad e \quad i \quad \Omega \quad \omega \quad \nu)$ is reminded here:

$$\begin{aligned} p &= a(1-e^2) \\ f &= e\cos(\omega+\Omega) \\ g &= e\sin(\omega+\Omega) \\ h &= \tan\frac{i}{2}\cos\Omega \\ k &= \tan\frac{i}{2}\sin\Omega \\ L &= \Omega+\omega+\nu \end{aligned} \tag{2.53}$$

The longitudinal anomaly L is used as parameter s instead of the azimuthal angle θ. The state vector is defined as $\mathbf{x}=\left[p,f,g,h,k,t\right]^T$ and one can obtain the Cartesian position vector from the transformation [40]:

$$\mathbf{r}\left(\mathbf{x},L\right)=\begin{pmatrix}\dfrac{p\left[\left(1+h^2-k^2\right)\cos L+2hk\sin L\right]}{\left(1+f\cos L+g\sin L\right)\left(1+h^2+k^2\right)}\\ \dfrac{p\left[\left(1-h^2+k^2\right)\sin L+2hk\cos L\right]}{\left(1+f\cos L+g\sin L\right)\left(1+h^2+k^2\right)}\\ \dfrac{2p\left(h\sin L-k\cos L\right)}{\left(1+f\cos L+g\sin L\right)\left(1+h^2+k^2\right)}\end{pmatrix} \tag{2.54}$$

A trajectory can be described as a continuous succession of points, parameterised by L here, where each point is on an instantaneous ellipse. So a succession of ellipses can be used to characterize a trajectory. However, at each point more than one ellipse can be chosen since one has the freedom to choose in what direction the instantaneous ellipse is going through the point, i.e. what is the velocity at that point on that instantaneous ellipse. There are therefore three degrees of freedom when choosing to characterize a trajectory as a succession of ellipses. This flexibility is called gauge freedom.

Among all the possible ellipses one can choose from at each instant, there is a special choice whereby the velocity of the instantaneous ellipse is equal to the physical velocity $\mathbf{v}$ along the trajectory. That special ellipse is qualified as osculating. This description of the trajectory is explained in detail by Efroimsky [41].

If one uses equinoctial elements and assigns a function of L to each of them to describe the evolution of the ellipses, then one can write the physical velocity as:

$$\mathbf{v}=\frac{d\mathbf{r}}{dL}\frac{dL}{dt}=\frac{1}{t'}\left(\frac{\partial\mathbf{r}}{\partial\mathbf{x}}\frac{d\mathbf{x}}{dL}+\frac{\partial\mathbf{r}}{\partial L}\right) \tag{2.55}$$

Primes denote differentiations with respect to L. The physical, osculating, velocity can be decomposed into two components: a velocity on an instantaneous non-osculating ellipse described by the shaped elements and a gauge term. The expression

of the velocity along the non-osculating ellipse is obtained by differentiating (2.54) with respect to L, while assuming that all other elements are fixed. Therefore one has:

$$\mathbf{v}_0 = \frac{1}{t_0'}\frac{\partial \mathbf{r}}{\partial L} \tag{2.56}$$

$t_0' = \dot{L}_0$ is the value obtained from the conservation of angular momentum and so:

$$t_0' = \frac{r^2}{\sqrt{\mu p}} = \frac{1}{\sqrt{\mu p}}\left(\frac{p}{1+f\cos L + g\sin L}\right)^2 \tag{2.57}$$

Since the physical velocity can be written as the sum of the non-osculating term and a gauge term $\mathbf{v}_{gauge}$, one obtains the following expression for the latter:

$$\mathbf{v}_{gauge} = \frac{1}{t'}\left(\frac{\partial \mathbf{r}}{\partial \mathbf{x}}\frac{d\mathbf{x}}{dL} + \frac{\partial \mathbf{r}}{\partial L}\right) - \frac{1}{t_{osc}'}\frac{\partial \mathbf{r}}{\partial L} = \frac{1}{t'}\left[\left(1 - \frac{t'}{t_{osc}'}\right)\frac{\partial \mathbf{r}}{\partial L} + \frac{\partial \mathbf{r}}{\partial \mathbf{x}}\frac{d\mathbf{x}}{dL}\right] = \frac{1}{t'}\mathbf{\Phi} \tag{2.58}$$

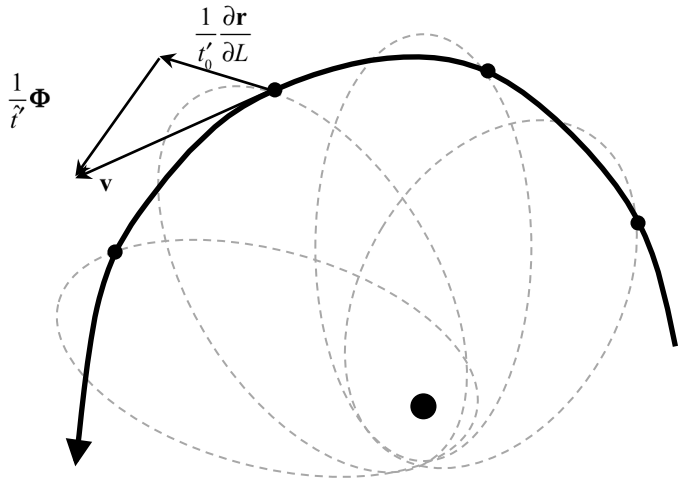

Fig. 2.4: Plot of a trajectory (bold line) whose points pass through instantaneous ellipses. In the illustrated case, the ellipses are not osculating because $\mathbf{\Phi} \neq \mathbf{0}$.

Fig. 2.4 illustrates the decomposition of the velocity into $\mathbf{v}_0$ and $\mathbf{v}_{gauge}$. The osculating condition imposes $\mathbf{v}_{gauge} = 0$.

If one sets functions of L to describe the evolution of the respective equinoctial elements, then the osculating condition will not necessarily be satisfied. These functions shall be called shaping functions and shall be denoted by the capital letters.

Developing (2.58) in a system of three nonlinear differential equations that define $\mathrm{Im}(f_x)$, and assuming that the equinoctial elements are governed by shaping functions, after simplification, the osculating conditions are written as:

$$\begin{cases} \dfrac{P'}{r} - F'\cos L - G'\sin L = \left(T'\dfrac{\sqrt{\mu P}}{r^2} - 1 \right)\left(F\sin L - G\cos L \right) \\ \dfrac{HK' - KH'}{1 + H^2 + K^2} = 1 - T'\dfrac{\sqrt{\mu P}}{r^2} \\ H'\sin L - K'\cos L = 0 \end{cases} \tag{2.59}$$

where

$$r = \frac{P}{1 + F\cos L + G\sin L} \tag{2.60}$$

It is generally accepted to call the set of elements described by P, F, G, H, K and L equinoctial only when they describe osculating orbits, and pseudo-equinoctial otherwise. The Gauss planetary equations are obtained from the three equations of motion and the three osculating conditions. Therefore if the parameters defining **x** were computed from the propagation of Gauss planetary equations, under a low-thrust action, then they would be conventional osculating non-singular equinoctial elements.

In the pseudo-equinoctial shaping, however, the dependency of all five elements p, f, g, h and k on L is defined by arbitrary shaping functions. In particular, the following functions were proposed in [29]:

$$\begin{cases} P(L) = p_0 + p_1 \exp \lambda_1 L \\ F(L) = f_0 + f_1 \exp \lambda_2 L \\ G(L) = g_0 + g_1 \exp \lambda_2 L \\ H(L) = h_0 + h_1 \exp \lambda_3 L \\ K(L) = k_0 + k_1 \exp \lambda_3 L \end{cases} \tag{2.61}$$

The parameters $\lambda_1, \lambda_2, \lambda_3$ are called shaping parameters and they are additional degrees of freedom that one can use to modify the shape of the trajectory.

The shaping function for the time component of the state vector, as in the spherical shaping method, is defined through its derivative with respect to the parameter *L*, for which the following expression was used:

$$T' = t_0' = \frac{1}{\sqrt{\mu P}}\left(\frac{P}{1+F\cos L+G\sin L}\right)^2 \tag{2.62}$$

Adopting the latter expression is like assuming that the out-of-plane component of the control vector is negligible with respect to the magnitude of the gravity field. The gauge function has then the expression $\mathbf{\Phi} = \left(\partial \mathbf{r} / \partial \mathbf{x}\right)\left(d\mathbf{x} / dL\right)$.

It can be verified that the shaping of the elements in Eqs. (2.61) and (2.62) does not satisfy $\mathbf{\Phi} = 0$ and therefore these elements do not represent an osculating orbit. Hence, they represent an orbit which passes through the same point as the osculating one but with a different velocity. It can be shown indeed that if (2.62) is chosen for the expression of T', then osculating conditions would impose $H' = K' = 0$ $H' = K' = 0$, i.e. the transfer is planar, and

$$\frac{P'}{P}\left(1+F\cos L+F\sin L\right)-F'\cos L-G'\sin L=0 \tag{2.63}$$

What actually happens is that by imposing a shape for the elements in **x** one fixes the gauge function $\mathbf{\Phi}$. If that function is not zero, i.e. the Lagrange constraint is not satisfied, then the elements in **x** are not osculating and do not satisfy the Gauss planetary equations.

Providing *T* from (2.62) and arbitrary shaping functions *P*, *F*, *G*, *H* and *K* defines the position through Eq. (2.54), the gauge function $\mathbf{\Phi}$ and the velocity through $\mathbf{v} = \left(\partial \mathbf{r} / \partial L + \mathbf{\Phi}\right) / T'$. Reciprocally, it can be shown that if one provides the position **r**, the velocity **v** and an arbitrary gauge function $\mathbf{\Phi}$, and assumes that *T* is defined as in (2.62), then the corresponding profiles for *P*, *F*, *G*, *H* and *K* exist and are unique. In fact, *P*, *F*, *G*, *H, K* and *L* are the osculating equinoctial elements corresponding to the position **r** and the velocity $\mathbf{v} - \mathbf{\Phi}\left\|\mathbf{v}\right\| / \left\|\partial \mathbf{r} / \partial L + \mathbf{\Phi}\right\|$. The special case of $\partial \mathbf{r} / \partial L + \Phi = 0$ corresponds to **v** = 0, which is rarely encountered in practice. It is worth noting that the component *t* of **x** is absent in the expression of $\mathbf{\Phi}$ because $\partial \mathbf{r} / \partial t = 0$.

2.3.1 Satisfying the boundary constraints

The coefficients p_0, f_0, g_0, h_0, k_0 and p_1, f_1, g_1, h_1, k_1 are computed by satisfying the boundary conditions on position and velocity. A Newton loop is performed to satisfy the boundary conditions exactly, since the sextuplet of functions $(P \quad F \quad G \quad H \quad K \quad L)$ does not define osculating equinoctial elements. The Newton loop is initialised with values for the coefficients that provide the osculating values for $(P \quad F \quad G \quad H \quad K \quad T)$ at the boundaries. In mathematical terms, the osculating values correspond to the solution to:

$$\begin{cases} \mathbf{r}\left(\mathbf{x}_i, L_i\right) = \mathbf{r}_i \\ \dfrac{1}{t_o'\left(\mathbf{x}_i, L_i\right)} \dfrac{\partial \mathbf{r}}{\partial L}\bigg|_{(\mathbf{x}_i, L_i)} = \mathbf{v}_i \\ \mathbf{r}\left(\mathbf{x}_f, L_f\right) = \mathbf{r}_f \\ \dfrac{1}{t_o'\left(\mathbf{x}_f, L_f\right)} \dfrac{\partial \mathbf{r}}{\partial L}\bigg|_{(\mathbf{x}_f, L_f)} = \mathbf{v}_f \end{cases} \tag{2.64}$$

From $(\mathbf{x}_i, L_i)$ and $(\mathbf{x}_f, L_f)$ one gets the values of the coefficients by solving the linear system (2.61). These coefficients are used to initialize the Newton loop to satisfy the boundary constraints. If the coefficients inside the shaping functions are assembled into a vector **c** with 10 components, then the solution to the following system in $(\mathbf{c}, L_i, L_f)$ is searched for iteratively:

$$\begin{cases} \mathbf{r}\left(\mathbf{x}\left(\mathbf{c}, L_i\right), L_i\right) = \mathbf{r}_i \\ \dfrac{1}{T'\left(\mathbf{x}\left(\mathbf{c}, L_i\right), L_i\right)} \left[\dfrac{\partial \mathbf{r}}{\partial L}\bigg|_{(\mathbf{x}(\mathbf{c}, L_i), L_i)} + \boldsymbol{\Phi}\left(\mathbf{x}\left(\mathbf{c}, L_i\right), L_i\right) \right] = \mathbf{v}_i \\ \mathbf{r}\left(\mathbf{x}\left(\mathbf{c}, L_f\right), L_f\right) = \mathbf{r}_f \\ \dfrac{1}{T'\left(\mathbf{x}\left(\mathbf{c}, L_f\right), L_f\right)} \left[\dfrac{\partial \mathbf{r}}{\partial L}\bigg|_{(\mathbf{x}(\mathbf{c}, L_f), L_f)} + \boldsymbol{\Phi}\left(\mathbf{x}\left(\mathbf{c}, L_f\right), L_f\right) \right] = \mathbf{v}_f \end{cases} \tag{2.65}$$

Eqs. (2.65) are a system of 12 equations with 12 unknowns. Using the coefficients from the osculating elements can be expected to be a good starting point for solving the system as long as the gauge function remains small, i.e. the pseudo-equinoctial elements are not too far from being osculating. In mathematical terms, this condition translates into:

$$\|\mathbf{\Phi}\| \ll \left\|\frac{\partial \mathbf{r}}{\partial L}\right\| \tag{2.66}$$

Due to the fact that $\mathbf{\Phi} = \left(\partial \mathbf{r} / \partial \mathbf{x}\right)\left(d\mathbf{x} / dL\right)$ and that one can expect the orders of magnitude of each $\partial \mathbf{r} / \partial x_j$ be the same as the one of $\partial \mathbf{r} / \partial L$, the condition (2.66) becomes ultimately $\left|dx_i / dL\right| \ll \left|x_i\right|$. The meaning of the latter is that the shaping functions should not have too abrupt variations. Therefore, no matter which expressions for the shaping functions are used, the shorter the transfer in terms of $L_f - L_i$, the farther the osculating initial guess will be from the solution of (2.65) and the smaller will be the chance that the Newton loop converges. This observation of course threatens the applicability of the method. Further research needs to be performed however on quantifying more in detail how and when the Newton-Raphson iteration does not converge. It can be said nevertheless, that if the flight is short, i.e. significantly shorter than one revolution, and the difference between the initial and final orbits is large, the iteration would be expected to be deficient with a higher chance.

When one needs to satisfy fewer boundary conditions, then a Newton loop can be applied to a smaller number of coefficients in the expression of the shaping functions while fixing the value of all extra coefficients. The values for the latter can theoretically be any but it is judicious to choose values such that the Newton loop converges more robustly. The values corresponding to appropriate osculating initial and final orbits can be used as starting point for the Newton loop as discussed previously.

When selecting the coefficients on which the Newton loop would be run, one needs to be consistent with the boundary constraints to be satisfied. For example, if the z-component of the position vector is imposed, then at least one of the coefficients in *H* or *K* should be used inside the Newton loop.

Once the values of the longitudinal anomalies at the boundaries and the coefficients inside the shaping functions of the pseudo-equinoctial elements are obtained, the trajectory is completely characterised. T' is defined through Eq. (2.62) and the evolution of time is then computed by solving the integral:

$$t = T(L) = \int_{L_i}^{L} T'(l)\,dl \tag{2.67}$$

The time of flight is uniquely defined. If the time of flight is constrained, then a second Newton loop over one of the shaping parameters can be used to satisfy that constraint. Finally, the total Δv is obtained by integrating $|\mathbf{u}|T'$ over $\left[L_i \;\; L_f + 2n_r\pi\right]$. The magnitude of the Δv can vary substantially, depending on the time of flight to be satisfied.

2.4 Satisfaction of the time of flight constraint

The advantage of generating trajectories by shaping the state vectors is that the equations of motion provide the corresponding control law analytically. However there are physical quantities that are more difficult to obtain with this method, one of them is the time of flight corresponding to a given shape. The time of flight is defined as $T(s_f) - T(s_i)$ and is a function of the parameter s. If the derivative of T is provided, as in the case of the shaping methods described above, then the time of flight is the integral of T' over $[s_i \;\; s_f]$. The analytical integral of T' is not generally possible and has to be solved numerically.

The time of flight is often constrained as the spacecraft has to arrive at destination at a given time to rendezvous or fly by a celestial body. In order to satisfy that constraint, at least one additional parameter is required when shaping the trajectory. A way to satisfy automatically the time of flight constraint is by shaping T or T' such that the desired time of flight T_f is exactly $T(s_f) - T(s_i) = \int_{s_i}^{s_f} T'\,ds$. One would be tempted to choose an expression for T' that can be analytically reduced to quadrature. Although this approach would be computationally the ideal way to solve the time of flight constraints, the resulting thrust profiles would not necessarily have reasonable

magnitudes in practice. That explains why, in the previous subsections, the time evolution profiles were chosen to correspond either to a tangential thrust or a 2D motion.

If the parameterisation is performed using the time t, one could then trivially define the trajectory in the desired segment $[t_i \quad t_f]$. This approach would remove the need to address any time of flight constraints further down in the calculations. On the other hand, quantities like the azimuthal angle θ or the longitudinal anomaly L would need to be constrained to take values within the desired limits such that the boundary conditions are satisfied. The problem of satisfying the time of flight constraint is then replaced by the problem of satisfying the boundary conditions.

A two-step approach to address the time of flight constraints is presented in this subsection, the second step being applied if the first one fails. The two steps differ in the way the additional parameter is used in the formulation of the shaping. The first one includes the parameter within the expression of the functions shaping the state vector. The second approach consists of augmenting the initial time evolution function T in a way that the time of flight constraint is exactly satisfied.

2.4.1 Inserting an additional parameter within the shaping functions of the state vector

This approach can be applied to all the shaping methods described in this document. It consists of adding a degree of freedom to the expression of one of the functions shaping the state vectors. The idea is that when one varies the value of the additional parameter, the time of flight varies, and the problem translates into the search for the right value of the parameter that satisfies the time constraint. Due to the nonlinear relationship between the time of flight and the shaping parameters, it is generally impossible to solve the problem analytically. Here, the Newton iteration for the solution of nonlinear equations was used.

2.4.2 Augmenting the original time of flight evolution

If the time t is decoupled from the other state variables in Eq.(2.4), instead of inserting the additional parameter within the expression of the shaping function, one can insert the additional parameter in the definition of $t = T(s)$.

Let us suppose that an initial trajectory, provided by a shaping method, has a time profile $t = T(s)$. Without loss of generality, one can take $T(s_i) = 0$ and $T(s_f)$ equal to the computed time of flight. If T_f is the desired time of flight and $T_{viol} = T(s_f) - T_f$ is the time of flight violation, one can introduce a function χ satisfying $\chi(s_f) - \chi(s_i) = 1$ such that the time profile is $T_\chi = T - T_{viol}\chi$, with T that verifies $T_\chi(s_f) = T_f$. The shaping of the time must be such that T_χ is strictly monotonous and T'_χ never becomes 0, otherwise singularities occur when calculating the control law. The simplest form that χ can take is $\chi(s) = (s - s_i)/\Delta s$ where $\Delta s = s_f - s_i$, however it is often the case that boundary conditions exist on $\dot{s}$ and thus on T'_χ. Therefore, the function χ must satisfy three conditions:

$$\begin{aligned} &\chi'(s_i) = 0; \\ &\chi'(s_f) = 0; \\ &\chi(s_f) - \chi(s_i) = 1 \end{aligned} \tag{2.68}$$

The last condition can be rewritten as $\int \chi' ds = 1$. Eqs. (2.68) can be satisfied by choosing a polynomial of degree two for χ such as $\chi'(s) = -6(s - s_i)(s - s_f)/\Delta s$.

This method for satisfying the time of flight constraints is faster than the use of the Newton loop since only two iterations are needed to find the desired trajectory: the first iteration computes the time of flight violation T_{viol}, the second recalculates the dynamics with $T_\chi = T - T_{viol}\chi$.

It should be noted, however, that if this method was applied alone to satisfy the time of flight constraints, then undesired phenomena might occur. In fact, the addition of $-T_{viol}\chi$ to the time evolution profile can distort the initial low-thrust character of the dynamics, and the resulting control profile can have a high magnitude. The

method can also break down in some cases when $T_\chi = T - T_{viol}\chi$ stops being strictly monotonous, in which case singularities occur when calculating $\dot{s} = 1/t'$, moreover time can go backwards. These inconvenient behaviours led to the decision to use this method only when the Newton loop fails to satisfy the time of flight constraint. When both methods break down, then one should try to find a different, more adapted expression for χ on an eventually more case by case basis.

2.5 Test cases

Four mission scenarios were selected to test the shaping methods and the method to satisfy the time of flight constraint: a rendezvous mission from the Earth to Mars, to the near Earth asteroid 1989ML, to comet Tempel-1 and to Neptune. The orbital elements of the four target bodies are listed in Table 2.1.

Only results for the spherical and the pseudo-equinoctial shaping are provided because of the lack of success for finding expressions for the shaping functions in the case of the hybrid shaping that result in Δvs low enough to be considered interesting in practice.

Systematic searches were conducted on a wide range of launch windows and times of flight, in order to evaluate the overall capacity of the shaping methods to model low thrust transfers. The characteristics of the spacecraft and its dynamics are the same in all three cases. The spacecraft is represented by a point with a mass of 1000 kg. It carries a propulsion system with a specific impulse of 3000 s. No limit on the achievable thrust magnitude is assumed. The spacecraft is subject only to the gravitational pull of a central body (the Sun in all four cases) and to the propulsion system.

Table 2.1 Orbital elements of Mars, near Earth asteroid 1989ML, Tempel-1 and Neptune

	Mars	1989ML	Tempel-1	Neptune
Semi-major axis	1.524 AU	1.272 AU	3.124 AU	30.104 AU
Eccentricity	0.093	0.137	0.517	0.011
Inclination	1.850°	4.378°	10.527°	1.768°
Right ascension	49.557°	104.411°	68.933°	131.794°
Argument of periapsis	286.502°	183.267°	178.926°	265.647°

The shapes were implemented in a Matlab code with all computations performed on an Intel Core 2 Duo processor running Linux.

The best shaped solutions were then used as initial guess for the direct trajectory analysis tool DITAN. DITAN takes the control profile resulting from the shaping as input and transcribes the optimal control problem associated to low-thrust trajectories with finite elements in time generated on spectral bases [42]. In this subsection, DITAN was run taking as maximum thrust level the peak thrust obtained from the shaping approaches, and minimizing the propellant mass, with the aim of assessing how close to optimal the Δvs provided by the shaping methods are. Proceeding this way for optimising clearly gives a significant advantage when it comes to test how the optimiser can be initialised since the initial guess does not violate the constraint on maximum thrust. However, not only would it be an arbitrary act to select a maximum thrust and see if the shaped trajectories can initialise the optimiser, but also, by proceeding in the proposed way, it is a better measure of propellant mass optimality to remove the issue of satisfying the peak thrust limit.

2.5.1 Rendezvous with Mars

The launch date t_i considered for this mission covers the period between January 1st 2020 and December 31st 2027 and is discretised with a 15-day time step. This window is large enough to contain almost four synodic periods of Mars (2.14 years). The time of flight ranges between 500 and 2000 days and is discretised with a 20-day time step size. The number of revolutions n_r allowed for the transfers is between 1 and 4.

Table 2.2 Results of each shaping method for the Mars rendezvous mission.

	Spherical	Pseudo-equinoctial
Percentage of feasible trajectories	100%	89.1%
Δv of the best trajectory [km/s]	5.74	5.83
Peak thrust of the shaped trajectory with the best Δv [N]	0.22	0.16
DITAN optimised Δv [km/s]	5.69	5.68
Average computational time for shaping a trajectory [s]	0.316	0.238

Trajectories were deemed feasible if the time of flight constraints were satisfied. Table 2.2 shows the percentage of feasible trajectories obtained through the systematic search for both the spherical and pseudo-equinoctial shaping methods. The

Δv of the best solution from each shaping is also presented together with the corresponding optimal solution when fed into DITAN. Note that the trajectories with the lowest Δv provided by the spherical shaping and by the pseudo-equinoctial shaping are different. A limit on the thrust was set when performing the optimisation, equal to the peak thrust of the shaped trajectory. Table 2.2 also reports the average time required to generate a solution with the shaping approach. Fig. 2.5 represents all the feasible solutions with their associated Δv cost. Note how the spherical shape provides a wider set of feasible solution with lower Δv. On the other hand both shapes identify the same regions in the $t_i - T_f$ space where the transfer requires a high Δv. These regions are located towards the lower values of T_f. A periodic pattern can be observed in the plots, where the period corresponds to the Earth-Mars synodic period.

The regions where the Δv is lower than 8 km/s are very similar, however the similarities break down when comparing the regions where the Δv is below 7 km/s. The differences are even more compelling when considering regions with a Δv lower than 6 km/s.

The two methods capture almost identical minimal Δvs however the basins corresponding to the local minima are much flatter for the spherical shaping than the pseudo-equinoctial shaping. The exponential evolution of the pseudo-equinoctial shaping functions is a good assumption for representing the local minima but when it comes to compressing or stretching the range of longitudinal anomalies and correspondingly the times of flight, the exponential form is not anymore the best representation. In the spherical shaping changing the time of flight has only an effect on the coefficients inside the function shaping the radius while the function shaping the elevation is only affected by the changing azimuthal angle range, which in the case of an Earth-Mars transfer should remain small.

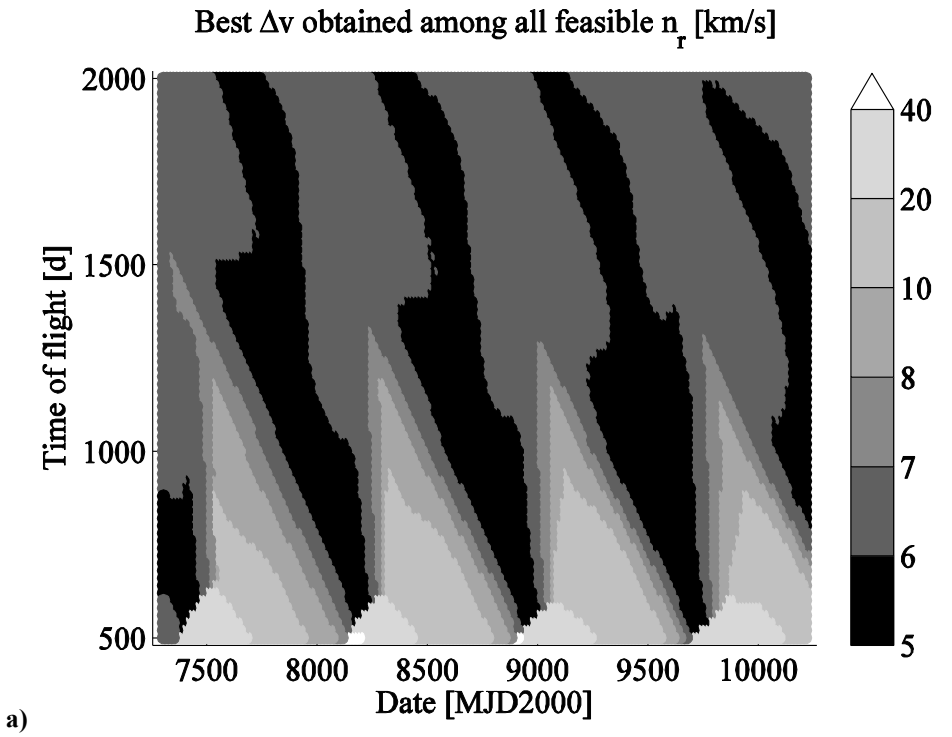

a)

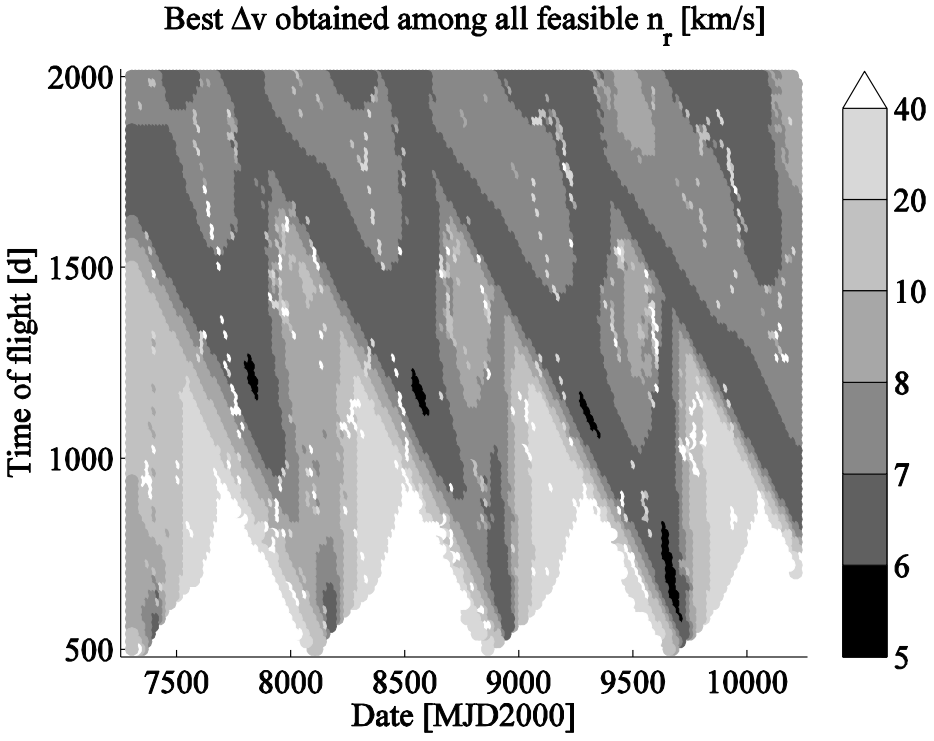

b)

Fig. 2.5 Illustration of the set of combinations of launch date and time of flight for which the spherical a) and the pseudo-equinoctial shaping b) found feasible solutions to rendezvous Mars.

2.5.2 Rendezvous with Near Earth Asteroid 1989ML

The launch window is the same as for the Mars case and was discretised with the same time step. The synodic period of asteroid 1989ML is 3.30 years, thus the launch window includes two full synodic periods. The range of the time of flight is between 100 and 1000 days, and is discretised with a 20-day time step size. The number of revolutions n_r allowed for the transfers is between 1 and 2.

Table 2.3 Results of each shaping method for the 1989ML rendezvous mission.

	Spherical	Pseudo-equinoctial
Percentage of feasible trajectories	83.7%	75.5%
Δv of the best trajectory [km/s]	4.47	4.82
Peak thrust of the shaped trajectory with the best Δv [N]	0.31	0.33
DITAN optimised Δv [km/s]	4.21	4.45
Average computational time for shaping a trajectory [s]	0.316	0.264

Table 2.3 presents the percentage of feasible solutions for both the spherical and pseudo-equinoctial shaping. The behaviour of the shaping method is similar to the case of the Mars rendezvous mission (see Fig. 2.5). The Δvs are on average lower than for the Mars mission, because the semi-major axis of 1989ML is lower. The difference in orbital inclination between Mars and 1989ML is only 2.5 degrees and it has a weaker impact on the total Δv than a difference of semi-major axis of 0.25 AU. The percentage of feasible trajectories is lower than for the Mars mission because the second step of the method to satisfy the time of flight results in a singularity, due to the behaviour explained in Section 2.4. Indeed, the Newton loop for satisfying the time of flight does not converge for the cases where the desired time of flight is very low compared to the number of revolutions. The reshaping of the time evolution T takes over in that case. However, the value of T_{viol} is too high causing T' to tend towards 0, and the resulting trajectory is not physical. Fig. 2.6 is a plot of the departure dates and times of flight of the feasible trajectories for both shaping methods. It can be observed that the spherical shaping always provides at least one feasible trajectory if the time of flight is above 300 days. For numbers of revolution that are unreasonable compared to the desired time of flight, both shaping methods break down.

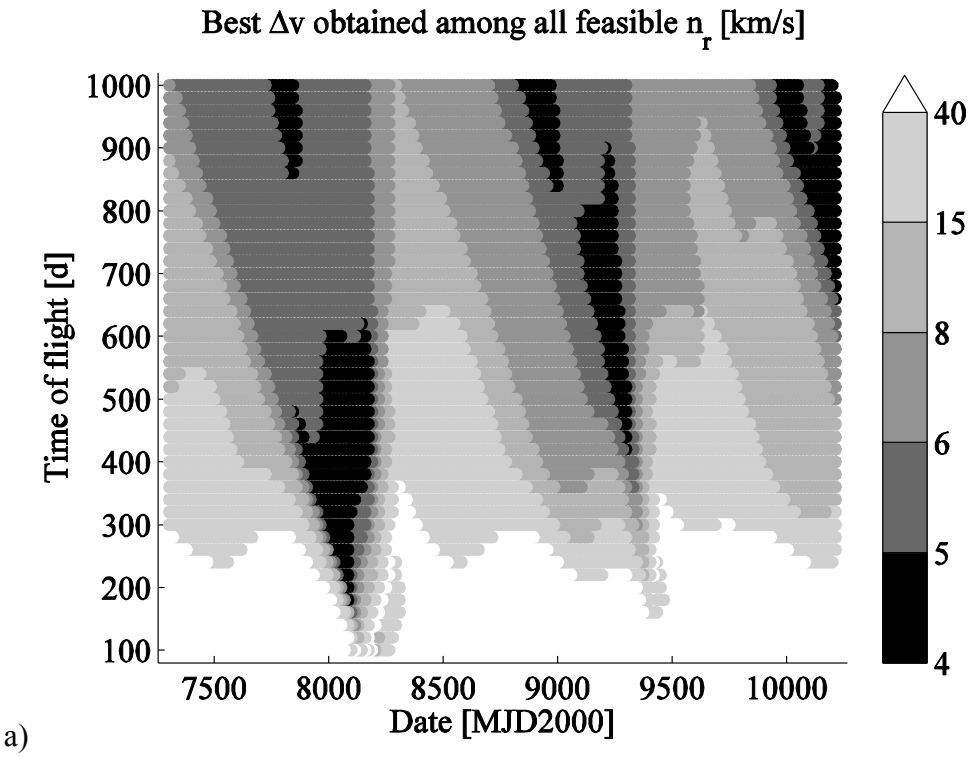

a)

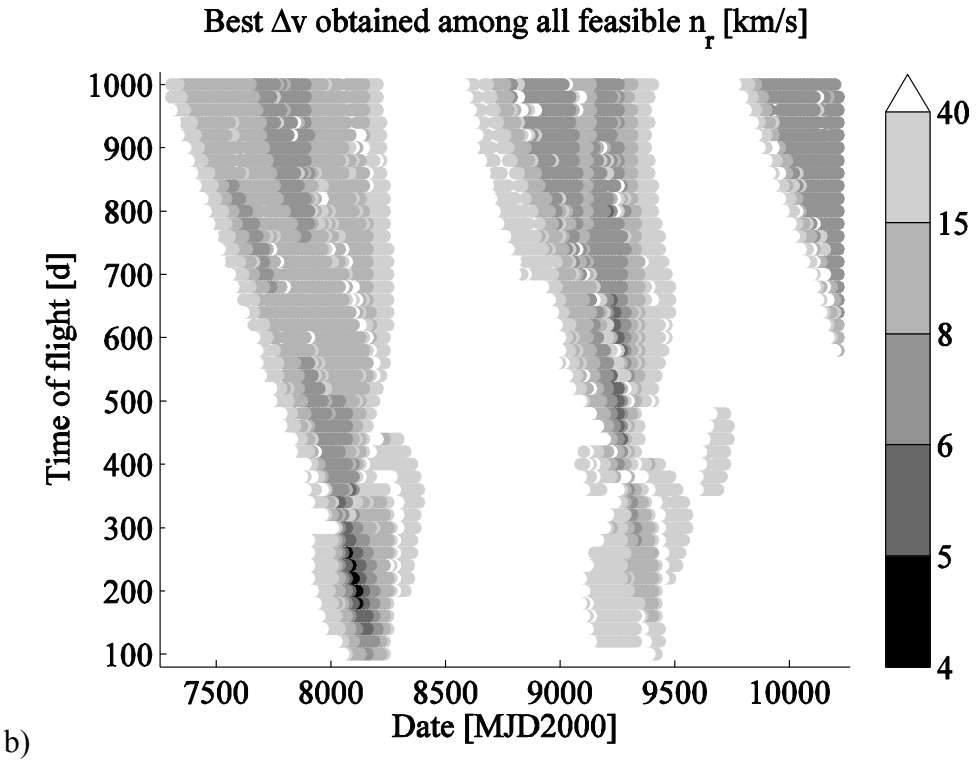

b)

Fig. 2.6 Illustration of the set of combinations of launch date and time of flight for which the spherical a) and the pseudo-equinoctial b) shaping method found feasible solutions to rendezvous 1989ML.

The pseudo-equinoctial shaping provides fewer feasible trajectories than the spherical shaping, because the shaping parameters do not give enough flexibility to change the shapes and attain wide ranges of times of flight. However similar patterns

can be observed in the results of both shaping methods, which hints to better suited relative configurations between Earth and 1989ML for a low-thrust transfer. The patterns show a periodicity equal to the value of the synodic period of the Earth-1989ML system.

2.5.3 Rendezvous with Comet Tempel-1

Tempel-1 was chosen as a target because it has a very eccentric and relatively inclined orbit. McConaghy et al. [43] used this test case for the exponential sinusoid shaping. A systematic search was performed on the same launch window proposed by McConaghy et al.: between 1 January 2000 and 3 January 2016. The range of the time of flight is between 400 and 1500 days, and the number of revolutions nr was set between 0 and 2.

Table 2.4 Results of each shaping method for the Tempel-1 rendezvous mission.

	Spherical	Pseudo-equinoctial
Percentage of feasible trajectories	68.1%	43.2%
Δv of the best trajectory [km/s]	11.13	13.44
Peak thrust of the shaped trajectory with the best Δv [N]	1.40	1.13
DITAN optimised Δv [km/s]	10.69	10.81
Average computational time for shaping a trajectory [s]	0.318	0.286

Table 2.4 presents the percentage of feasible solutions for both the spherical and pseudo-equinoctial shaping. The behaviour of the two shaping methods is similar to the previous two cases; however fewer trajectories are feasible because the Newton loop fails to converge more often, although for every launch date at least one feasible trajectory exists. McConaghy et al. present the propellant mass fractions resulting from the exponential sinusoids. A constant specific impulse of 3000 seconds is used to convert the low-thrust Δv from the exponential sinusoid. Using this value for the specific impulse, the Δv of 11.13 km/s of the best transfer from the spherical shaping converts into a propellant mass fraction of 31.5%. The pseudo-equinoctial's best Δv of 13.44 km/s converts into 36.7% of propellant mass fraction. No impulsive Δvs are to be taken into account because the boundary constraints on velocity are satisfied. A substantial improvement in the best Δv found is obtained compared to McConaghy et al. whose best shaped trajectory requires 50% of propellant mass fraction.

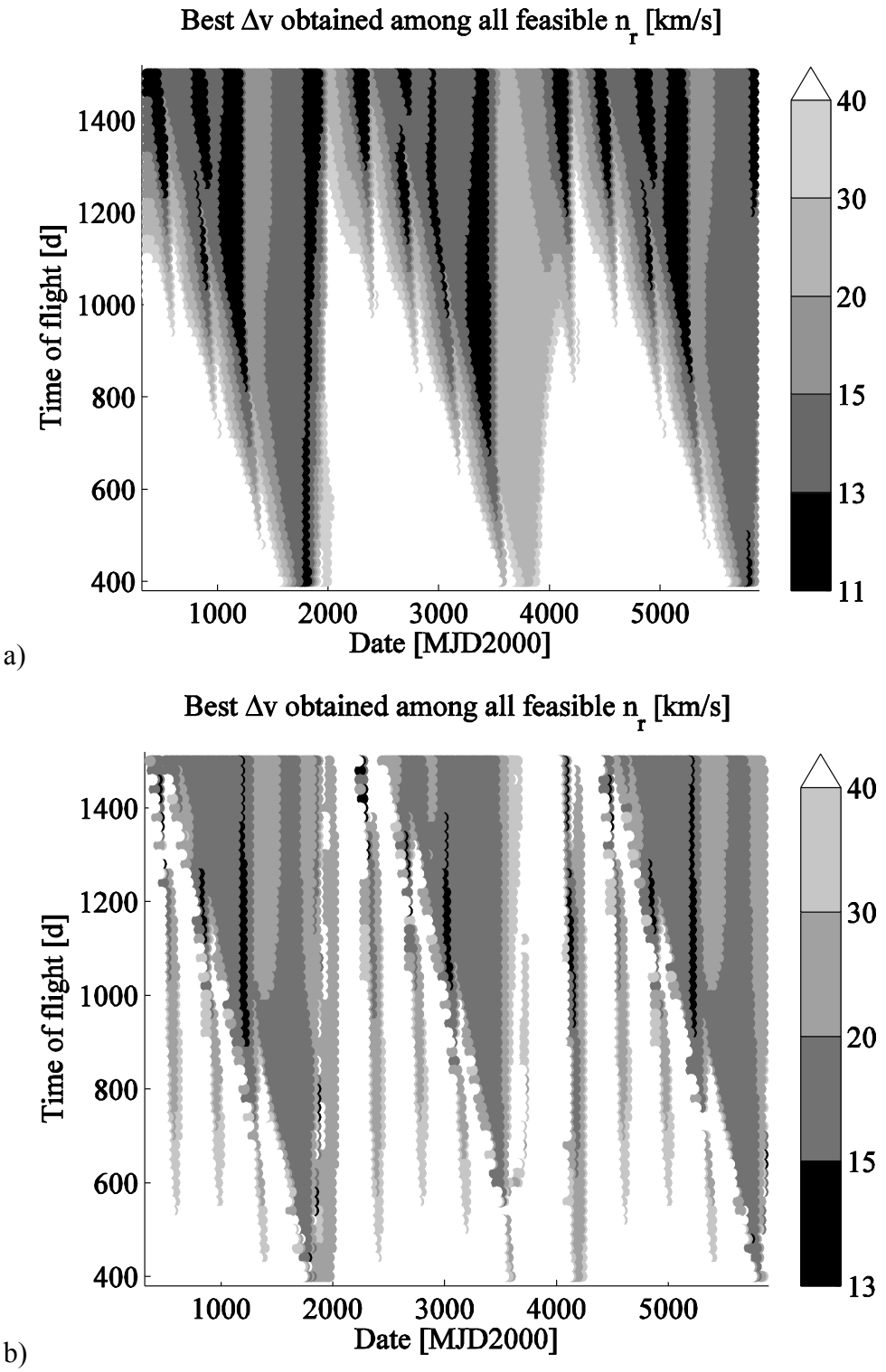

Fig. 2.7 Illustration of the set of combinations of launch date and time of flight for which the spherical a) and the pseudo-equinoctial b) shaping method found feasible solutions to rendezvous Tempel 1.

Fig. 2.7 illustrates the set of feasible combinations of launch dates and times of flight found by the spherical and the pseudo-equinoctial shaping methods. When more than one number of revolutions is feasible for a given combination of launch date and

time of flight then only the one with the lowest Δv is plotted. Both shaping methods identify the same region where the transfer is too costly in Δv. These regions are periodically distributed, with the period of Tempel 1. A smaller scale periodicity also exists, and corresponds to the Earth's period (and close to the synodic period of the Earth-Tempel 1 system).

It can be therefore deduced from the plots that the arrival position on Tempel 1's orbit has more impact than the departure position on Earth's orbit. There is physical sense in this observation because the transfer can change substantially if the spacecraft arrives at Tempel 1's perihelion at 1.51 AU or apohelion at 4.74 AU. Indeed, in the first case the perihelion is raised first, followed by the apohelion just before arrival, and in the second case the order of the two maneuvers is inversed. Finally, the results show that the transfers are generally more costly in Δv when the time of flight shortens.

2.5.4 Rendezvous with Neptune

In order to test the shaping methods on a wide range of transfer types, a rendezvous with Neptune is also studied as test case. Neptune has a semi-major axis of 30.1 AU and an orbital period of 164.8 years. One can make initial estimations of the orders of magnitude involved in a rendezvous to Neptune by studying the Hohmann transfer between two circular orbits representing Earth's and Neptune's. Straightforward computations provide the characteristics of the Hohmann transfer. The transfer ellipse has a semimajor axis of 15.6 AU and eccentricity of 0.94 and the transfer time is 30.7 years. The first maneuver at Earth has a Δv of 11.66 km/s and the second one at Neptune is of 4.05 km/s, so the total Hohmann transfer requires a Δv of 15.71 km/s.

Table 2.5 Results of each shaping method for the Neptune rendezvous mission with no revolution

	Spherical	Pseudo-equinoctial
Percentage of feasible trajectories	92.4%	13.6%
Δv of the best trajectory [km/s]	14.99	50.37
Peak thrust of the shaped trajectory with the best Δv [N]	1.36	3.25
DITAN optimised Δv [km/s]	13.34	13.41
Average computational time for shaping a trajectory [s]	0.321	0.292

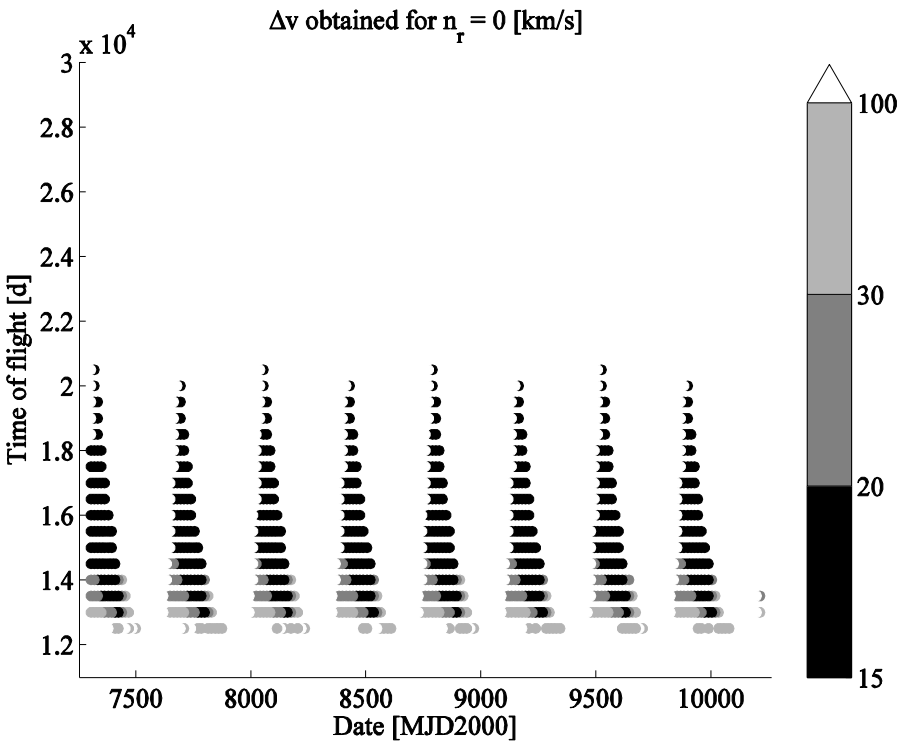

a)

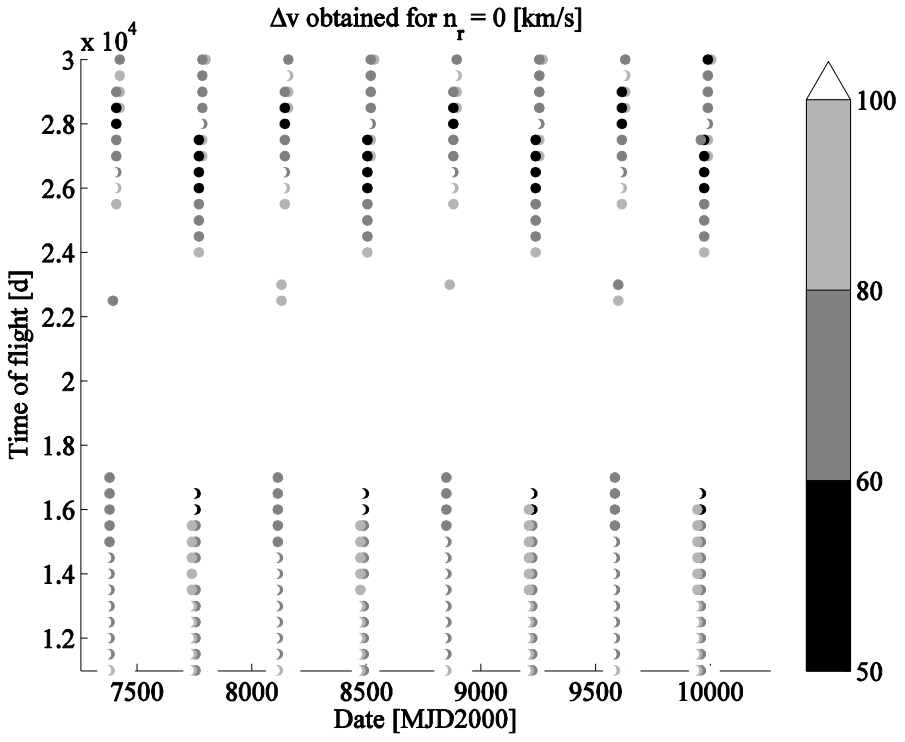

b)

Fig. 2.8 Illustration of the set of combinations of launch date and time of flight for which the spherical a) and the pseudo-equinoctial b) shaping method found feasible solutions to rendezvous Neptune, without any revolution.

A systematic search was performed over a launch window between January 1st 2020 and December 31st 2025, discretised at every 15 days. Two scenarios have been

addressed: one without heliocentric revolutions and one with 10 revolutions. The values of times of flight that were investigated differed between the two cases. For no revolutions that set ranged between 11000 and 30000 days (that is 30.1 and 82.1 years) at 500-day time steps. For the case of 10 revolutions, the times of flight ranged between 40000 and 80000 days, with intervals of 500 days. An initial tangential velocity of 3 km/s relative to Earth was set at the departure for the transfers without revolutions, while in the other case the initial relative velocity at the Earth is zero. The reason for that is to limit the peak thrust of the transfer. Moreover it would also be likely that such a mission would be injected directly into an Earth escape trajectory by the launcher.

It can be seen from Fig. 2.8 that the two shaping methods provide different results when no revolutions are allowed. The spherical shaping produces transfers with substantially lower Δvs, with the lowest values of Δv reaching 15 km/s. The results have a periodicity of a year, which is the synodical period of the Sun-Earth-Neptune system. With the spherical shaping, the lowest Δvs are obtained for transfers between 13000 days and 20000 days. Shaping the pseudo-equinoctial elements does not provide interesting results for two reasons. The first is that the Newton loop does not impose the boundary conditions well, the other is that the range of times of flight covered by varying the shaping parameter λ_1 is limited and the reshaping of the time evolution has to be used, which can potentially raise the Δvs by much.

Much fewer acceptable results are provided by the pseudo-equinoctial shaping since the Newton-Raphson iteration on the boundary conditions has more difficulties to converge due to the larger effect of the gauge term. This is because the relative variation of pseudo-equinoctial elements is high. Moreover the time of flight constraint is less often satisfied through Newton-Raphson iteration due to the interval of values that would be allowed by the shaping parameters' variation, and therefore the time of flight is satisfied by reshaping the time of flight evolution which increases the necessary Δv substantially.

2.5.5 Discussion

Both shaping methods generated a number of feasible solutions for every launch date, although the Newton loop failed to converge for a number of times of flight. In

particular, the loop did not converge when the flight time is short for the given number of revolutions. The cases in which the Newton loop fails correspond to trajectories with very high Δvs and as such, are often not interesting in practice. It should be noted, however, that due to the imposed shape there is no guarantee that the thrust magnitude is close to the optimal one. More importantly, the peak thrust recovered from the dynamic equations might be higher than the maximum thrust allowed for the transfer. This problem will be addressed in the next chapter of this thesis and represents a limitation of the shaping approach, as it does not allow for a clear discrimination of the feasibility of a transfer given a specific engine.

CHAPTER 3 IMPROVEMENT OF TRAJECTORIES WITH A LINEAR QUADRATIC CONTROLLER

This section describes a method to quickly improve the quality of the shaped solutions. The assumption behind this approach is that if the shaped solution is not locally optimal then one can reasonably expect an optimal solution in a neighbourhood of the shaped one. The validity of this assumption will be verified theoretically at the end of this section.

3.1 Derivation of the LQ controller

Let one assume that a spacecraft has position **r**, velocity **v** and is subject to the gravitational pull of a central body with a gravity parameter μ. Additionally the spacecraft has an on-board controllable propulsion system that contributes to the motion of the spacecraft with an acceleration **u**. If one defines the state vector **x** as $\mathbf{x}=\left[\mathbf{r}^T,\mathbf{v}^T\right]^T$ then the equations of motion can be written as $\dot{\mathbf{x}}=\mathbf{A}\left(\mathbf{x}\right)+\mathbf{B}\mathbf{u}$, with $\mathbf{A}\left(\mathbf{x}\right)=\left[\mathbf{O}_3,-\mu\mathbf{r}^T/r^3\right]^T$ and $\mathbf{B}=\left[\mathbf{O}_3,\mathbf{1}_3\right]^T$. The equations of motion are then linearised in the neighbourhood of the nominal $\mathbf{x_0}$ and $\mathbf{u_0}$ within the time interval I_t. Indicating by the subscript l the linearised variable and setting $\xi=\mathbf{x}_l-\mathbf{x}_0$ and $\nu=\mathbf{u}_l-\mathbf{u}_0$, the linearised system is:

$$\begin{cases}\xi\left(t_i\right)=\left[0,0,0,0,0,0\right]^T\\ \dot{\xi}=\nabla\mathbf{A}\big|_{\mathbf{x}_0(t)}\left(\mathbf{x}_l-\mathbf{x}_0\left(t\right)\right)+\mathbf{B}\left(\mathbf{u}_l-\mathbf{u}_0\left(t\right)\right)=\nabla\mathbf{A}\Big|_{\mathbf{x}_0(t)}\xi+\mathbf{B}\upsilon\end{cases} \tag{3.1}$$

The gradient of **A** at a point **x** is expressed as:

$$\nabla\mathbf{A}=\begin{bmatrix}\mathbf{O}_3 & \mathbf{I}_3\\ \mathbf{A}_g & \mathbf{O}_3\end{bmatrix} \tag{3.2}$$

such that $\mathbf{O}_3$ is the nil square matrix of order 3, $\mathbf{I}_3$ is the identity matrix of order 3 and $\mathbf{A}_g$ is written:

$$\mathbf{A}_g = \frac{\mu}{r^5}\begin{bmatrix} y^2+z^2 & -xy & -xz \\ -xy & x^2+z^2 & -yz \\ -xz & -yz & x^2+y^2 \end{bmatrix} \tag{3.3}$$

with $\mathbf{r} = [x, y, z]^T$. Defining $\xi_1 = \left[\xi^T, 1\right]^T$, $\mathbf{A}_1$ and $\mathbf{B}_1$ such that:

$$\mathbf{A}_1 = \left[\nabla\mathbf{A}, \mathbf{O}_{3\times 1}\right] \tag{3.4}$$

and

$$\mathbf{B}_1 = \left[\mathbf{B}, -\mathbf{B}\mathbf{u}_0\right] \tag{3.5}$$

Eq. (3.1) can be rewritten as:

$$\begin{cases} \xi_1(t_i) = \left[0,0,0,0,0,0,1\right]^T \\ \dot{\xi}_1 = \mathbf{A}_1(t)\xi_1 + \mathbf{B}_1\mathbf{u}_l \end{cases} \tag{3.6}$$

with the control vector denoted by $\mathbf{u}_l$ and the augmented state $\xi_1 = \left[\xi^T, 1\right]^T$ to remove $\mathbf{u}_0$ from the equations. The desired optimal control has to minimize the objective function:

$$J_1(\mathbf{u}_l) = \xi_1{}^T(t_f)\mathbf{Q}_1\xi_1(t_f) + \frac{1}{2}\int_l \|\mathbf{u}_l\|^2 \, dt \tag{3.7}$$

The minimisation of (3.7) provides the feedback control:

$$\mathbf{u}_l = \mathbf{B}_1^T\mathbf{E}\xi_1 \tag{3.8}$$

where the matrix $\mathbf{E}$ is computed by integrating backwards the Riccati differential equation:

$$\begin{cases} \mathbf{E}\left(t_f\right) = -\mathbf{Q}_1 \\ \dot{\mathbf{E}} = -\mathbf{A}_1^T\mathbf{E} - \mathbf{E}\mathbf{A}_1 - \mathbf{E}\mathbf{B}_1\mathbf{B}_1^T\mathbf{E}, \forall t \in I_t \end{cases} \tag{3.9}$$

The first term in the objective function will make ξ_1 tend towards 0, which is what is required: the perturbations on the trajectory should not affect the boundaries. The fact that the last component of ξ_1 is always 1 is not an issue because the choice of $\mathbf{Q}_1$ is made such that it does not influence the convergence of the other components of ξ_1 towards 0. The matrix $\mathbf{Q}_1$ is defined as:

$$\mathbf{Q}_1 = \begin{bmatrix} q_r\mathbf{I}_3 & 0 & 0 \\ 0 & q_v\mathbf{I}_3 & 0 \\ 0 & 0 & 0 \end{bmatrix} \quad \text{for} \quad q_r > 0, \quad q_v > 0 \tag{3.10}$$

where q_r is a weight on the final position vector to satisfy the final boundary constraint, and q_v has the same role but for the velocity. The values for the two weights were set to 1 in order to satisfy the boundary conditions at arrival up to a relative accuracy of 10^{-6}. Note that minimizing J_1 with Eq. (3.6) is the same as minimizing $J_l\left(\mathbf{u}_l\right) = \xi^T\left(t_f\right)\mathbf{Q}\xi\left(t_f\right) + \frac{1}{2}\int_I \|\mathbf{u}_l\|^2 dt$ with the condition in Eq. (3.1). $\mathbf{Q}$ is the matrix composed of the block containing the first six rows and six columns inside $\mathbf{Q}_1$.

The optimisation requires the integration of a 7 by 7 matrix differential equation backwards in time, followed by the forward integration of the linearised equations of motion using the matrix $\mathbf{E}$. The first integration can be made computationally faster by noting that $\mathbf{E}$ is a symmetric, hence it is sufficient to compute 28 variables instead of 49. The numerical propagations, in this paper, were performed with the Matlab function *ode45,* that implements a 4^{th}-5^{th} order Runge-Kutta variable step size integrator, with a relative and absolute tolerance of 10^{-9}.

Once the optimised linearised trajectory $\mathbf{x}_0 + \xi$ is computed, the corresponding control law needs to be updated since it verifies the linearised equations of motion and not the real ones. The real control law corresponding to the physical trajectory is calculated from:

$$\mathbf{u}_{real} = \ddot{\mathbf{r}}_{real} + \frac{\mu}{r_{real}^3}\mathbf{r}_{real} \tag{3.11}$$

Note that keeping the linearised control law and calculating the corresponding state vectors by propagation would not only be more computationally intensive but would not guarantee that the trajectory ends at the target state vector. Finally, the total Δv can be calculated by an integration of $\mathbf{u}_{real}$ over I_t.

3.2 Estimation of the Error on the Control Profile

The accuracy of the linearised solution can be assessed by computing the error between $\mathbf{u}_l$ and $\mathbf{u}_{real}$. If $\mathbf{x}_0$ and $\mathbf{u}_0$ define the reference trajectory, $\left(\mathbf{x}_0+\xi,\mathbf{u}_l\right)$ the optimal linearised trajectory and $\left(\mathbf{x}_0+\xi,\mathbf{u}_{real}\right)$ the trajectory obtained after recomputing $\mathbf{u}_l$ with the real dynamics, then one has the equations:

$$\dot{\mathbf{x}}_0=\mathbf{A}\left(\mathbf{x}_0\right)+\mathbf{B}\mathbf{u}_0 \tag{3.12}$$

$$\dot{\xi}=\nabla\mathbf{A}\big|_{\mathbf{x}_0}\cdot\xi+\mathbf{B}\left(\mathbf{u}_l-\mathbf{u}_0\right) \tag{3.13}$$

$$\dot{\mathbf{x}}_0+\dot{\xi}=\mathbf{A}\left(\mathbf{x}_0+\xi\right)+\mathbf{B}\mathbf{u}_{real} \tag{3.14}$$

By subtracting Eq. (3.12) and (3.13) from Eq., (3.14) one gets

$$\mathbf{B}\left(\mathbf{u}_l-\mathbf{u}_{real}\right)=\mathbf{A}\left(\mathbf{x}_0+\xi\right)-\mathbf{A}\left(\mathbf{x}_0\right)-\nabla\mathbf{A}\big|_{\mathbf{x}_0}\cdot\xi \tag{3.15}$$

which can be approximated by:

$$\mathbf{B}\left(\mathbf{u}_l-\mathbf{u}_{real}\right)=\xi^T\,\mathbf{H}_{\mathbf{A}}\big|_{\mathbf{x}_0}\,\xi+O\left(\|\xi\|^3\right) \tag{3.16}$$

where $\mathbf{H}_{\mathbf{A}}\big|_{\mathbf{x}_0}$ is the Hessian of $\mathbf{A}$ at $\mathbf{x}_0$. Because $\mathbf{A}$ depends only on the reference position $\mathbf{r}_0$, $\mathbf{H}_{\mathbf{A}}\big|_{\mathbf{x}_0}$ also depends on $\mathbf{r}_0$ only. If one defines $\Delta\mathbf{u}=\mathbf{u}_l-\mathbf{u}_{real}=\left[\Delta u_x,\Delta u_y,\Delta u_z\right]^T$ and $\xi_{\mathbf{r}}$ as the first three components of ξ, i.e., the change of position resulting from the LQ controller, then Eq. (3.16) can be developed into the system:

$$\begin{cases} \Delta u_x = \xi_{\mathbf{r}}^T \, \mathbf{H}_{\mathbf{A}}^1 \big|_{r_0} \, \xi_{\mathbf{r}} + O\left(\left\|\xi_{\mathbf{r}}\right\|^3\right) \\ \Delta u_y = \xi_{\mathbf{r}}^T \, \mathbf{H}_{\mathbf{A}}^2 \big|_{r_0} \, \xi_{\mathbf{r}} + O\left(\left\|\xi_{\mathbf{r}}\right\|^3\right) \\ \Delta u_z = \xi_{\mathbf{r}}^T \, \mathbf{H}_{\mathbf{A}}^3 \big|_{r_0} \, \xi_{\mathbf{r}} + O\left(\left\|\xi_{\mathbf{r}}\right\|^3\right) \end{cases} \tag{3.17}$$

In Eqs. (3.17) one has that all of $\mathbf{H}_{\mathbf{A}}^i$ depends only on $\mathbf{r}_0$ and that $\left\|\mathbf{H}_{\mathbf{A}}^i\right\| = O\left(\left\|\mathbf{r}_0\right\|^{-4}\right)$. The interpretation of these equations is that the error on the control law corresponding to the linearised equations of motion depends uniquely on the position of the reference trajectory and the perturbations in position. Moreover, when one assumes that the perturbations in the position are small, then the error behaves as $\left\|\mathbf{r}_0\right\|^{-4}$, or as $\left\|\mathbf{r}_0\right\|^{-2}$ if one considers the relative perturbations $\xi_{\mathbf{r}} / \left\|\mathbf{r}_0\right\|$. Therefore, when the reference trajectory approaches the central body, the difference between the control corresponding to the real equations of motion and the control computed with the linearised equations of motion increases.

The evolution of $\xi_{\mathbf{r}}$ depends on its integration along the nominal trajectory. Initially its norm is small since it starts at 0, and upon arrival it also goes to 0 since the final state is reached. Therefore what is important is that in the middle of the cruising phase the corrected trajectory does not go lower considerably closer to the central body than the initial and final position.

3.3 Optimality of the LQ and shaped solutions

In this section, it will be proven that: if the shaped solution is locally optimal, then the output from the LQ controller will be equal to the shaped solution. Vice versa, it is demonstrated that when the output of the LQ controller is equal to the shaped solution, the shaped solution is locally optimal. As will be shown, the latter inference is not trivial due to the non-linearity of the dynamical system.

Let us define the two mathematical problems:

$$\wp_l := \begin{cases} \min_{\mathbf{u}_l} J_l\left(\mathbf{u}_l\right) \\ \xi\left(t_i\right) = 0 \\ \dot{\xi} = f_l\left(\xi, \mathbf{u}_l\right) = \nabla \mathbf{A}\big|_{\mathbf{x}_0(t)} \cdot \xi + \mathbf{B}\left(\mathbf{u}_l - \mathbf{u}_0\right) \end{cases} \tag{3.18}$$

and:

$$\wp := \begin{cases} \min_{\mathbf{u}} J(\mathbf{u}) \\ \mathbf{x}(t_i) = \left[\begin{array}{cc} \mathbf{r}_0(t_i)^T, & \mathbf{v}_0(t_i)^T \end{array} \right]^T \\ \dot{\mathbf{x}} = f(\mathbf{x}, \mathbf{u}) = \mathbf{A}(\mathbf{x}) + \mathbf{B}\mathbf{u} \end{cases} \tag{3.19}$$

where J has the form:

$$J(\mathbf{u}) = \left(\mathbf{x}(t_f) - \mathbf{x}_0(t_f)\right)^T \mathbf{Q}\left(\mathbf{x}(t_f) - \mathbf{x}_0(t_f)\right) + \frac{1}{2}\int_l \|\mathbf{u}\|^2 \, dt \tag{3.20}$$

The Hamiltonians corresponding to $\wp$ and to $\wp_l$ are respectively $H = \mathbf{p}f - \|\mathbf{u}\|^2/2$ and $H_l = \mathbf{p}_l f_l - \|\mathbf{u}_l\|^2/2$. If one calls $\mathbf{p}^*$, $\mathbf{u}^*$, $\mathbf{p}_l^*$ and $\mathbf{u}_l^*$ the respective optimal adjoint variables and control profiles, then the optimality conditions $\partial H/\partial \mathbf{u} = 0$ and $\partial H_l/\partial \mathbf{u}_l = 0$ give the control laws:

$$\begin{aligned} \mathbf{u}^* &= \mathbf{B}^T \mathbf{p}^{*T} = \mathbf{p}_{\mathbf{v}}^{*T} \\ \mathbf{u}_l^* &= \mathbf{B}^T \mathbf{p}_l^{*T} = \mathbf{p}_{l\mathbf{v}}^{*T} \end{aligned} \tag{3.21}$$

The subscripts **r** and **v** denote respectively the first three and the last three components of the adjoint vectors. The differential equations governing the optimal adjoint variables $\mathbf{p}^*$ and $\mathbf{p}_l^*$ are:

$$\begin{aligned} \dot{\mathbf{p}}^* &= -\partial H/\partial \mathbf{x} = -\mathbf{p}^* \cdot \partial f/\partial \mathbf{x} = -\mathbf{p}^* \cdot \nabla \mathbf{A}\big|_{\mathbf{x}^*} \\ \dot{\mathbf{p}}_l^* &= -\partial H/\partial \boldsymbol{\xi} = -\mathbf{p}_l^* \cdot \partial f_l/\partial \boldsymbol{\xi} = -\mathbf{p}_l^* \cdot \nabla \mathbf{A}\big|_{\mathbf{x}_0(t)} \end{aligned} \tag{3.22}$$

with the transversality conditions:

$$\begin{aligned} \mathbf{p}^*(t_f) &= -\left(\mathbf{x}(t_f) - \mathbf{x}_0(t_f)\right)^T \mathbf{Q}_0 \\ \mathbf{p}_l^*(t_f) &= -\boldsymbol{\xi}(t_f)^T \mathbf{Q}_0 \end{aligned} \tag{3.23}$$

From the latter, one gets $\mathbf{p}^*(t_f)=\mathbf{p}_l^*(t_f)$. It is important to note that due to the smoothness of **A** and the expression of the differential equations governing $\mathbf{x}^*$, $\mathbf{x}_l{}^*$, $\mathbf{p}^*$ and $\mathbf{p}_l^*$, the last four quantities are C^∞ on their interval of definition. Therefore, the control profiles $\mathbf{u}^*$ and $\mathbf{u}_l^*$ are also C^∞.

Three lemmas establishing some properties of $\mathbf{A}_g$ and three propositions on the nature of the solutions to problems $\wp$ and $\wp_l$ are now proved.

Lemma 1: Given the set $U=\mathbb{R}^3\setminus\{(0,0,0)\}$, $\forall\mathbf{x}\in U,\forall\mathbf{q}\in\mathbb{R}^3$, $\mathbf{A}_g(\mathbf{x})\cdot\mathbf{q}=\dfrac{\mu}{\|\mathbf{x}\|^5}\mathbf{x}\wedge(\mathbf{q}\wedge\mathbf{x})$.

Proof: Let $\mathbf{x}=[x,y,z]^T\in U$ and $\mathbf{q}=[q_1,q_2,q_3]^T\in\mathbb{R}^3$. From the definition of $\mathbf{A}_g$, one has:

$$\mathbf{A}_g(\mathbf{x})=\frac{\mu}{\|\mathbf{x}\|^5}\begin{bmatrix}y^2+z^2 & -xy & -xz\\ -xy & x^2+z^2 & -yz\\ -xz & -yz & x^2+y^2\end{bmatrix} \tag{3.24}$$

then:

$$\mathbf{A}_g(\mathbf{x})\cdot\mathbf{q}=\frac{\mu}{\|\mathbf{x}\|^5}\begin{pmatrix}(y^2+z^2)q_1-xyq_2-xzq_3\\ -xyq_1+(x^2+z^2)q_2-yzq_3\\ -xzq_1-yzq_2(x^2+y^2)q_3\end{pmatrix} \tag{3.25}$$

and since

$$\mathbf{x}\wedge(\mathbf{q}\wedge\mathbf{x})=\begin{pmatrix}x\\y\\z\end{pmatrix}\wedge\begin{pmatrix}q_2z-q_3y\\q_3x-q_1z\\q_1y-q_2x\end{pmatrix}=\begin{pmatrix}(y^2+z^2)q_1-xyq_2-xzq_3\\ -xyq_1+(x^2+z^2)q_2-yzq_3\\ -xzq_1-yzq_2(x^2+y^2)q_3\end{pmatrix} \tag{3.26}$$

then $\mathbf{A}_g(\mathbf{x})\cdot\mathbf{q}=\dfrac{\mu}{\|\mathbf{x}\|^5}\mathbf{x}\wedge(\mathbf{q}\wedge\mathbf{x})$. ■

Lemma 2: $\forall\mathbf{x}\in U$ and $\mathbf{q}\in\mathbb{R}^3\setminus\{(0,0,0)\}$, $\mathbf{A}_g(\mathbf{x})\cdot\mathbf{q}=0\Leftrightarrow\mathbf{q}$ and $\mathbf{x}$ are collinear. Note that **x** cannot be the null vector.

Proof: From Lemma 1, if one has $\mathbf{A}_g(\mathbf{x})\cdot\mathbf{q}=\mu\|\mathbf{x}\|^{-5}\mathbf{x}\wedge(\mathbf{q}\wedge\mathbf{x})=0$, then there exists $\lambda\in\mathbb{R}$ such that $\mathbf{q}\wedge\mathbf{x}=\lambda\mathbf{x}$. Taking the dot product of both sides with **x** in the latter equation and remembering that $\mathbf{x}\neq 0$, one gets $\lambda=0$. Thus **q** and **x** are collinear. Reciprocally, if **q** is collinear with **x**, then $\mathbf{A}_g(\mathbf{x})\cdot\mathbf{q}=0$. ■

Lemma 3: Let $\mathbf{x},\mathbf{y}\in U$. The matrix $\mathbf{A}_g(\mathbf{x})-\mathbf{A}_g(\mathbf{y})$ has maximum rank if and only if $\mathbf{x}\neq\pm\mathbf{y}$.

Proof: Let $\mathbf{x},\mathbf{y}\in U$ such that $\mathbf{x}\neq\pm\mathbf{y}$, and $\mathbf{q}\in\mathbb{R}^3$ such that $\mathbf{A}_g(\mathbf{x})\cdot\mathbf{q}=\mathbf{A}_g(\mathbf{y})\cdot\mathbf{q}$, then if $\|\mathbf{x}\|$ and $\|\mathbf{y}\|$ are the Euclidian norms of **x** and **y** respectively, one has:

$$\mathbf{x}\wedge(\mathbf{q}\wedge\mathbf{x})/\|\mathbf{x}\|^5=\mathbf{y}\wedge(\mathbf{q}\wedge\mathbf{y})/\|\mathbf{y}\|^5 \tag{3.27}$$

Expanding and rearranging this expression to isolate **q**, one obtains:

$$\left(\frac{1}{\|\mathbf{x}\|^3}-\frac{1}{\|\mathbf{y}\|^3}\right)\mathbf{q}=\frac{\mathbf{x}\cdot\mathbf{q}}{\|\mathbf{x}\|^5}\mathbf{x}-\frac{\mathbf{y}\cdot\mathbf{q}}{\|\mathbf{y}\|^5}\mathbf{y} \tag{3.28}$$

If $\|\mathbf{x}\|=\|\mathbf{y}\|$, then Eq.(3.28) yields $(\mathbf{x}\cdot\mathbf{q})\mathbf{x}=(\mathbf{y}\cdot\mathbf{q})\mathbf{y}$ therefore $\mathbf{x}=\pm\mathbf{y}$, which goes against our initial assumption. Therefore $\|\mathbf{x}\|\neq\|\mathbf{y}\|$ and then Eq. (3.28) results in $\mathbf{q}=\alpha_{\mathbf{q}}\mathbf{x}+\beta_{\mathbf{q}}\mathbf{y}$ with,

$$\alpha_{\mathbf{q}}=\left(\frac{1}{\|\mathbf{x}\|^3}-\frac{1}{\|\mathbf{y}\|^3}\right)^{-1}\frac{\mathbf{x}\cdot\mathbf{q}}{\|\mathbf{x}\|^5}\qquad\beta_{\mathbf{q}}=\left(\frac{1}{\|\mathbf{x}\|^3}-\frac{1}{\|\mathbf{y}\|^3}\right)^{-1}\frac{\mathbf{y}\cdot\mathbf{q}}{\|\mathbf{y}\|^5} \tag{3.29}$$

Inserting the expression for **q** into Eq. (3.27) one has, after rearranging the terms:

$$\left(\frac{\beta_{\mathbf{q}}}{\|\mathbf{x}\|^5}\mathbf{x}-\frac{\alpha_{\mathbf{q}}}{\|\mathbf{y}\|^5}\mathbf{y}\right)\wedge(\mathbf{x}\wedge\mathbf{y})=0 \tag{3.30}$$

From Eq. (3.27) it can be obtained that if **x** and **y** are collinear then $\|\mathbf{x}\|=\|\mathbf{y}\|$. Hence **x** and **y** are not collinear, i.e., $\mathbf{x}\wedge\mathbf{y}\neq 0$. This means that **q** lies in the plane

generated by $\mathbf{x}$ and $\mathbf{y}$. Eq.(3.30) results in $\beta_{\mathbf{q}}\|\mathbf{x}\|^{-5}\mathbf{x} - \alpha_{\mathbf{q}}\|\mathbf{y}\|^{-5}\mathbf{y} = 0$, thus $\alpha_{\mathbf{q}} = \beta_{\mathbf{q}} = 0$ and $\mathbf{x}\cdot\mathbf{q} = \mathbf{y}\cdot\mathbf{q} = 0$ which implies $\mathbf{q} = 0$. Therefore the endomorphism $\mathbf{A}_g(\mathbf{x}) - \mathbf{A}_g(\mathbf{y})$ is injective and hence invertible, and its rank is 3.

Conversely, it can be checked that if $\mathbf{x} = \pm\mathbf{y}$, then $\mathbf{A}_g(\mathbf{x}) = \mathbf{A}_g(\mathbf{y})$ and $\mathbf{A}_g(\mathbf{x}) - \mathbf{A}_g(\mathbf{y})$ does not have maximum rank. ■

Proposition 1: Let $\mathbf{u}^*$ (respectively $\mathbf{u}_l^*$) be a solution of the optimisation problem $\wp$ (resp. $\wp_l$). Then $\mathbf{p}^{*T} = \begin{bmatrix} -\dot{\mathbf{u}}^{*T} & \mathbf{u}^{*T} & \kappa \end{bmatrix}^T$ (resp. $\mathbf{p}_l^{*T} = \begin{bmatrix} -\dot{\mathbf{u}}_l^{*T} & \mathbf{u}_l^{*T} & \kappa_l \end{bmatrix}^T$), where κ (resp. κ_l) is a scalar function, and $\mathbf{u}^*$ (resp. $\mathbf{u}_l^*$) satisfies the differential equations:

$$\begin{aligned} \ddot{\mathbf{u}}^* + \mathbf{A}_g\left(\left(\mathbf{x}_0 + \boldsymbol{\xi}\right)(t)\right)\mathbf{u}^* = 0 \\ \ddot{\mathbf{u}}_l^* + \mathbf{A}_g\left(\mathbf{x}_0(t)\right)\mathbf{u}_l^* = 0 \end{aligned} \tag{3.31}$$

Proof: From the optimality conditions, one has the expressions $\mathbf{u}^* = \mathbf{B}_1^T\mathbf{p}^{*T}$ and $\mathbf{u}_l^* = \mathbf{B}_1^T\mathbf{p}_l^{*T}$. Developing these expressions, the control vectors correspond to the fourth to sixth components of the adjoint variables. Moreover, since $\dot{\mathbf{p}}^{*T} = -\mathbf{A}_1^T\left(\left(\mathbf{x}_0 + \boldsymbol{\xi}\right)(t)\right)\mathbf{p}^{*T}$ and $\dot{\mathbf{p}}_l^{*T} = -\mathbf{A}_1^T\left(\mathbf{x}_0(t)\right)\mathbf{p}_l^{*T}$, one gets $\dot{\mathbf{u}}^* = \mathbf{B}_1^T\dot{\mathbf{p}}^{*T} = -\mathbf{B}_1^T\mathbf{A}_1^T\left(\left(\mathbf{x}_0 + \boldsymbol{\xi}\right)(t)\right)\mathbf{p}^{*T}$ and $\dot{\mathbf{u}}_l^* = \mathbf{B}_1^T\dot{\mathbf{p}}_l^{*T} = -\mathbf{B}_1^T\mathbf{A}_1^T\left(\mathbf{x}_0(t)\right)\mathbf{p}_l^{*T}$. By developing the expressions of $\mathbf{A}_1^T$ and $\mathbf{B}_1^T$, one finds that the first three components of the adjoint variables correspond to the opposite of the derivative of the controls. So one can write $\mathbf{p}^{*T} = \begin{bmatrix} -\dot{\mathbf{u}}^{*T} & \mathbf{u}^{*T} & \kappa \end{bmatrix}^T$ and $\mathbf{p}_l^{*T} = \begin{bmatrix} -\dot{\mathbf{u}}_l^{*T} & \mathbf{u}_l^{*T} & \kappa_l \end{bmatrix}^T$. From the expressions of the derivatives of the adjoint variables, one obtains:

$$\dot{\mathbf{p}}^{*T} = \begin{pmatrix} -\ddot{\mathbf{u}}^* \\ \dot{\mathbf{u}}^* \\ \dot{\kappa} \end{pmatrix} = -\mathbf{A}_1^T\left(\left(\mathbf{x}_0 + \boldsymbol{\xi}\right)(t)\right)\begin{pmatrix} -\dot{\mathbf{u}}^* \\ \mathbf{u}^* \\ \kappa \end{pmatrix} = \begin{pmatrix} -\mathbf{A}_g\left(\left(\mathbf{x}_0 + \boldsymbol{\xi}\right)(t)\right)\mathbf{u}^* \\ \dot{\mathbf{u}}^* \\ \mathbf{u}_0^T\mathbf{u}^* \end{pmatrix} \tag{3.32}$$

$$\dot{\mathbf{p}}_l^{*T} = \begin{pmatrix} -\ddot{\mathbf{u}}_l^* \\ \dot{\mathbf{u}}_l^* \\ \dot{\kappa}_l \end{pmatrix} = -\mathbf{A}_1^T\left(\mathbf{x}_0(t)\right)\begin{pmatrix} -\dot{\mathbf{u}}_l^* \\ \mathbf{u}_l^* \\ \kappa_l \end{pmatrix} = \begin{pmatrix} -\mathbf{A}_g\left(\mathbf{x}_0(t)\right)\mathbf{u}_l^* \\ \dot{\mathbf{u}}_l^* \\ \mathbf{u}_0^T\mathbf{u}_l^* \end{pmatrix} \tag{3.33}$$

The differential equations satisfied by the components of $\mathbf{u}^*$ and $\mathbf{u}_l^*$ are the first three components in Eqs. (3.32) and (3.33). ■

Proposition 2: Let $\mathbf{u}^*$ (respectively $\mathbf{u}_l^*$) be a solution of the optimisation problem $\wp$ (resp. $\wp_l$). Let $I_t = \left(\begin{array}{cc} t_1 & t_2 \end{array} \right) \subset \mathbb{R}$ be an open interval of time. Let us assume that the angular momentum along the trajectory corresponding to $\mathbf{u}^*$ (resp. $\mathbf{u}_0$) is never zero. If $\mathbf{p}_\mathbf{r}^* = 0$ (resp. $\mathbf{p}_{l\mathbf{r}}^* = 0$) on I_t, then $\mathbf{u}^* = 0$ (resp. $\mathbf{u}_l^* = 0$) on I_t.

Proof: From proposition 1, $\mathbf{p}_\mathbf{r}^* = 0$ (resp. $\mathbf{p}_{l\mathbf{r}}^* = 0$) on I_t implies that $\dot{\mathbf{u}}^* = 0$ (resp. $\dot{\mathbf{u}}_l^* = 0$) on I_t, and thus $\ddot{\mathbf{u}}^* = 0$ (resp. $\ddot{\mathbf{u}}_l^* = 0$) on I_t. From the differential equations provided by Proposition 1, one obtains $\mathbf{A}_g\left((\mathbf{x}_0 + \boldsymbol{\xi})(t)\right)\mathbf{u}^* = 0$ (resp. $\mathbf{A}_g\left(\mathbf{x}_0(t)\right)\mathbf{u}_l^* = 0$). Thus, according to Lemma 2, there exists a scalar function λ on I_t, such that $\mathbf{u}^* = \lambda(\mathbf{x}_{\mathbf{r}0} + \boldsymbol{\xi}_\mathbf{r})$ (resp. $\mathbf{u}_l^* = \lambda \mathbf{x}_{\mathbf{r}0}$). λ is continuously differentiable because $\mathbf{x}_{\mathbf{r}0} + \boldsymbol{\xi}_\mathbf{r}$ (resp. $\mathbf{x}_{\mathbf{r}0}$) is continuously differentiable. From this, one obtains the differential equation $\dot{\lambda}\left(\mathbf{x}_{\mathbf{r}0} + \boldsymbol{\xi}_\mathbf{r}\right) + \lambda\left(\dot{\mathbf{x}}_{\mathbf{r}0} + \dot{\boldsymbol{\xi}}_\mathbf{r}\right) = 0$ (resp. $\dot{\lambda}\mathbf{x}_{\mathbf{r}0} + \lambda\dot{\mathbf{x}}_{\mathbf{r}0} = 0$). Because the trajectories are always assumed to have angular momentum bounded away from zero, one gets $\lambda = 0$ and $\dot{\lambda} = 0$ and thus $\mathbf{u}^* = 0$ (resp. $\mathbf{u}_l^* = 0$) on I_t. Due to the continuous nature of the optimal thrust profiles, the latter result is valid on $\bar{I}_t = \left[t_1 \quad t_2 \right]$. ■

Proposition 3: Let $\mathbf{u}^*$ be a solution of $\wp$ and $\mathbf{u}_l^*$ a solution of $\wp_l$. Let us assume that the angular momentum of the initial trajectory $\mathbf{x}_0$ never cancels. If $\mathbf{u}^* = \mathbf{u}_l^*$ then there are three regimes in which the trajectory can evolve:

1. $\mathbf{x}^* = \mathbf{x}_0$
2. $\mathbf{x}^* = -\mathbf{x}_0$
3. $\mathbf{u}^* = \mathbf{u}_l^* = 0$, i.e. the optimal trajectories are coast arcs.

Moreover, the optimal trajectories cannot switch between regimes 1 and 2 without passing through regime 3 on an open interval of time $(t_1 \quad t_2)$, and switching between regime 1 and regime 3 can only happen if $\mathbf{u}_0 = 0$ at the boundary.

Proof: From Eqs. (3.21), if $\mathbf{u}^* = \mathbf{u}_l^*$ then $\mathbf{p}_\mathrm{v}^* = \mathbf{p}_{l\mathrm{v}}^*$ and $\dot{\mathbf{p}}_\mathrm{v}^* = \dot{\mathbf{p}}_{l\mathrm{v}}^*$. Furthermore, $\dot{\mathbf{p}}_\mathrm{v}^* = -\mathbf{p}_\mathrm{r}^*$ and $\dot{\mathbf{p}}_{l\mathrm{v}}^* = -\mathbf{p}_{l\mathrm{r}}^*$ implies $\mathbf{p}_\mathrm{r}^* = \mathbf{p}_{l\mathrm{r}}^*$, thus $\mathbf{p}^* = \mathbf{p}_l^*$. From Eqs.(3.22) one gets $\mathbf{p}_l^* \cdot \left(\nabla \mathbf{A}\big|_{\mathbf{x}^*} - \nabla \mathbf{A}\big|_{\mathbf{x}_0} \right) = 0$ therefore $\mathbf{p}_{l\mathrm{r}}^* \cdot \left(\mathbf{A}_g(\mathbf{x}^*) - \mathbf{A}_g(\mathbf{x}_0) \right) = 0$. According to Lemma 3, $\left(\mathbf{A}_g(\mathbf{x}^*) - \mathbf{A}_g(\mathbf{x}_0) \right)$ has full rank as long as $\mathbf{x}^* \neq \pm \mathbf{x}_0$, therefore, there exists three regimes in which the trajectory can evolve: $\mathbf{x}^* = \mathbf{x}_0$, $\mathbf{x}^* = -\mathbf{x}_0$ or $\mathbf{p}_{l\mathrm{r}}^* = 0$. Proposition 2 can be applied for regime 3 because the angular momentum of the initial trajectory $\mathbf{x}_0$ is assumed to never cancel. If $\mathbf{p}_{l\mathrm{r}}^* = 0$ on an interval of time $(t_1 \quad t_2)$, then $\mathbf{u}^* = \mathbf{u}_l^* = 0$ on $(t_1 \quad t_2)$, i.e. the optimal trajectories are coast arcs.

The trajectory cannot switch between regime 1 and regime 2 directly because the trajectory is continuous. Therefore, regimes 1 and 2 can switch only if regime 3 takes place between the two. However, in that case, the system has to be in regime 3 on an interval of time $(t_1 \quad t_2)$ and not for an isolated instant of time t_0, because otherwise, due to the continuity of the trajectory, the system would bounce back to the regime leading up to regime 3. There is a condition when the system can swap between regime 1 and regime 3 on an interval of time $(t_1 \quad t_2)$ since at the boundary between regime 1 and regime 3 $\xi = 0$ and $\dot{\xi} = 0$, from Eq. (3.1) one obtains that $\mathbf{u}_l^* = \mathbf{u}_0$ at the switching point, otherwise the velocity profile would not be continuous. Finally, because when the system is in regime 3 on $I_t = (t_1 \quad t_2)$, $\mathbf{u}^* = \mathbf{u}_l^* = 0$ on I, by continuity on the controls are zero on the closure of I, i.e. on $\bar{I}_t = [t_1 \quad t_2]$, and finally one obtains that at the boundary between regimes 1 and 3, $\mathbf{u}_0 = 0$. ■

Theorem: Let $\mathbf{u}^*$ be a solution of $\wp$ and $\mathbf{u}_l^*$ a solution of $\wp_l$, then $\mathbf{u}^* = \mathbf{u}_0 \Rightarrow \mathbf{u}^* = \mathbf{u}_l^*$. Furthermore, if $\mathbf{u}_0 \neq 0$ along the whole trajectory and the angular momentum of the reference trajectory $\mathbf{x}_0$ is never zero, then $\mathbf{u}^* = \mathbf{u}_l^* \Rightarrow \mathbf{u}^* = \mathbf{u}_0$.

Proof: The first inference is proven first. If $\mathbf{u}^* = \mathbf{u}_0$, then $\mathbf{x}^* = \mathbf{x}_0$ and the equations governing $\mathbf{p}^*$ and $\mathbf{p}_l^*$ are identical, thus $\mathbf{p}^* = \mathbf{p}_l^*$ and $\mathbf{u}^* = \mathbf{u}_l^*$. Note that to establish this inference, no particular property of $\nabla \mathbf{A}$ is required.

The proof of the reciprocal inference requires special properties of the dynamical systems, and therefore of the gravity field. This inference is a corollary of Proposition 3. Because the starting points of the trajectories are fixed at $\mathbf{x}^*(t_i) = \mathbf{x}_l^*(t_i) = \mathbf{x}_0(t_i)$, the optimised trajectories start in regime 1 and since $\mathbf{u}_0 \neq 0$ along the whole trajectory, the

system remains in the same regime all the time. Therefore, $\mathbf{x}^* = \mathbf{x}_0$ and $\mathbf{u}^* = \mathbf{u}_0$ along the whole trajectory. ■

From this result one could argue that if the LQ controller does not modify the reference trajectory, then the reference trajectory is locally optimal, on the other hand, little can be said if the control $\mathbf{u}_l^*$ is worse than $\mathbf{u}_0$.

3.4 Application of the LQ Controller

The LQ controller is applied to the improvement of the solutions to the four mission test cases presented in Section 2.5. Only those transfers that do not pass inside Venus's orbit were retained in order to keep the error due to linearisation small. The reason for this comes from the considerations in subsection 3.3 which sets a limit of validity of the linearisation involved in the LQ controller. Fig. 3.1 to Fig. 3.3 show the improvement of the L_2 norm of the control profiles $\frac{1}{2}\int_I \|\mathbf{u}\|^2 dt$ between the shaped trajectories and the corresponding LQ controlled trajectories.

Fig. 3.5 to Fig. 3.10 are examples of thrust profiles corresponding to the shaped trajectories, the LQ controlled trajectories and the DITAN re-optimised trajectories, for all three rendezvous missions. The figures illustrate well how the control profiles improve at each step.

There are cases where there is no improvement of the L_2 norm of the control. This happens when the trajectory is too close to the central body, i.e. inside Venus's orbit, in which case the control corresponding to the real equations of motion diverges from the optimal control of the linearised equations of motion, as described in technical terms in Section 3.2. Otherwise, the LQ controller has the tendency to reduce the control magnitude because a better L_2 norm of the control translates, in general, to lower peak controls. Indeed, when a function is squared, the peaks become more prominent and it becomes more effective to reduce these peaks. Applying the LQ controller to shaped trajectories can therefore reduce the risk of discarding some mission scenarios due to the high magnitude of the peak thrust.

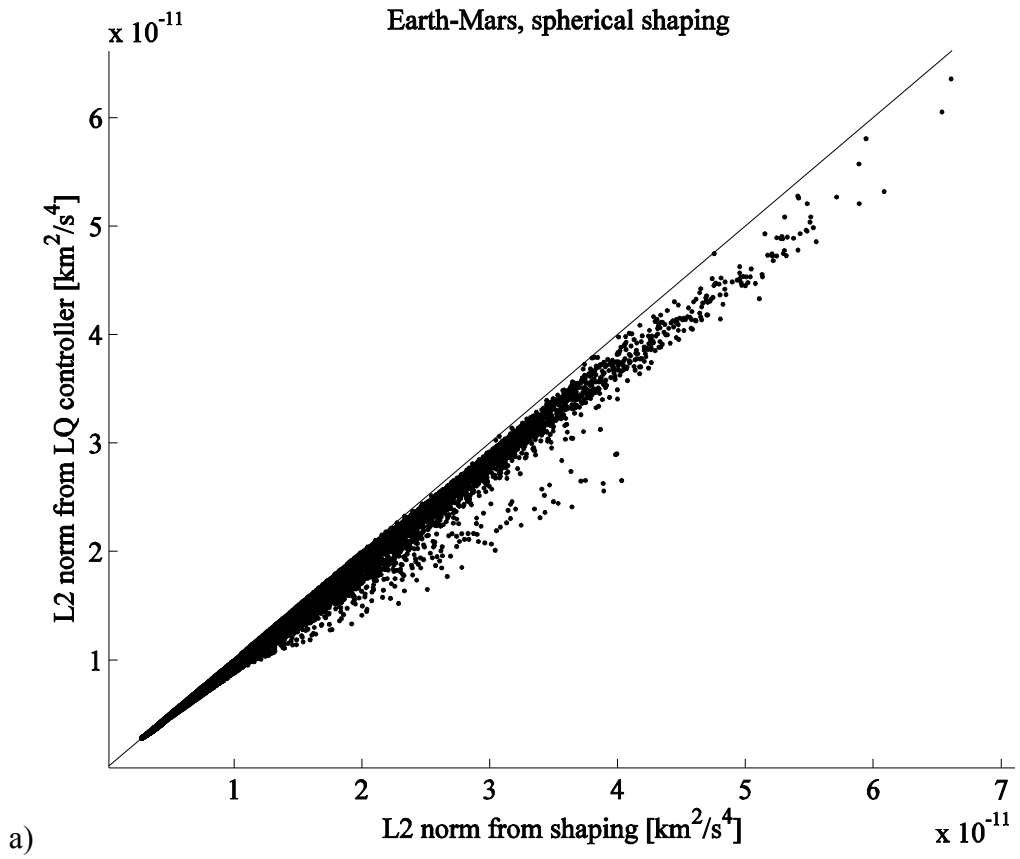

a)

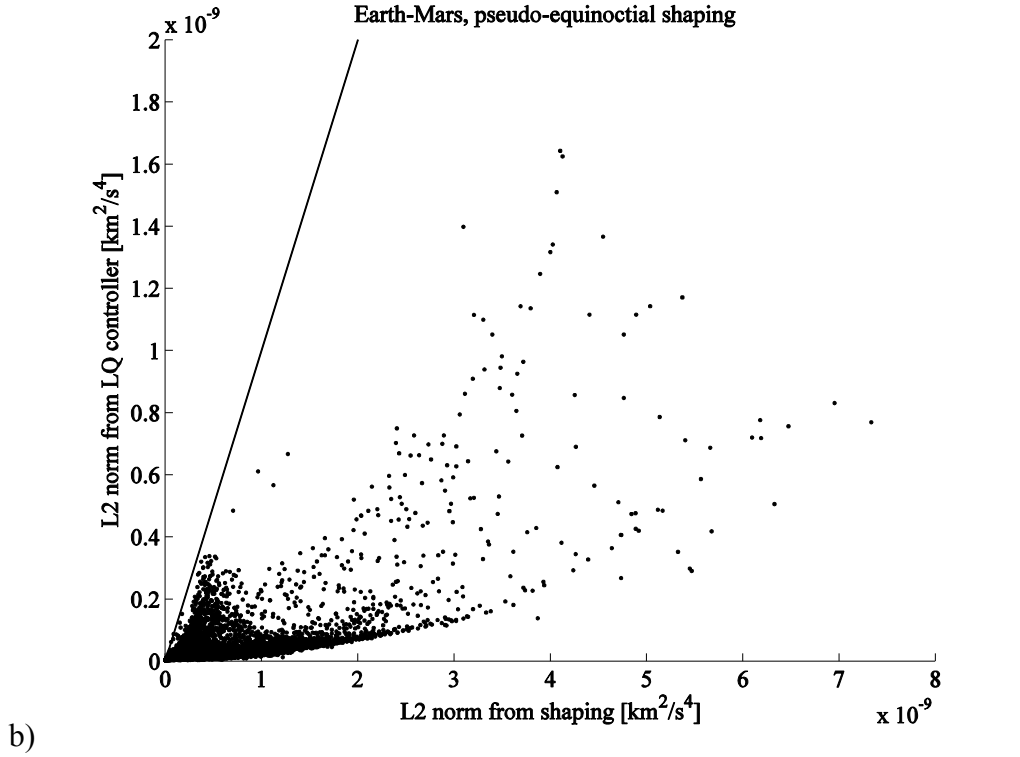

b)

Fig. 3.1: Comparison between the L_2 norms of the controls of the spherical and pseudo-equinoctial shaped transfers and the corresponding LQ-controlled improvement for the Mars rendezvous mission. a) Spherical shaping b) Pseudo-equinoctial shaping

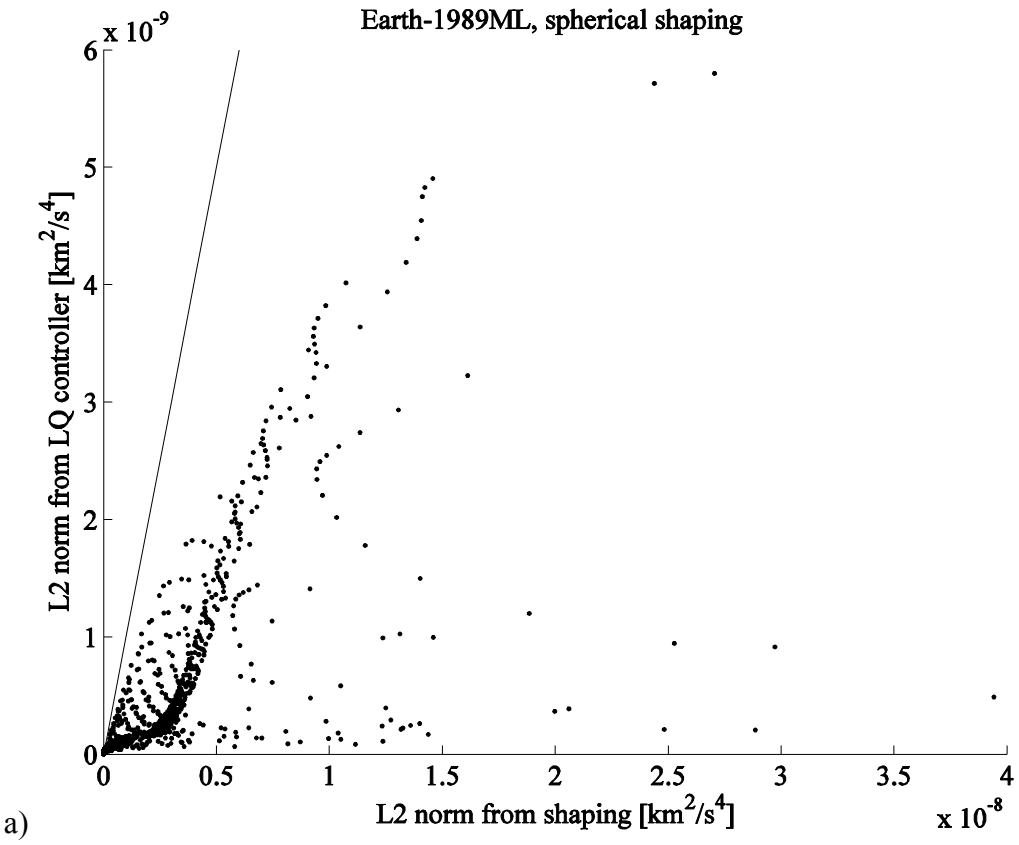

a)

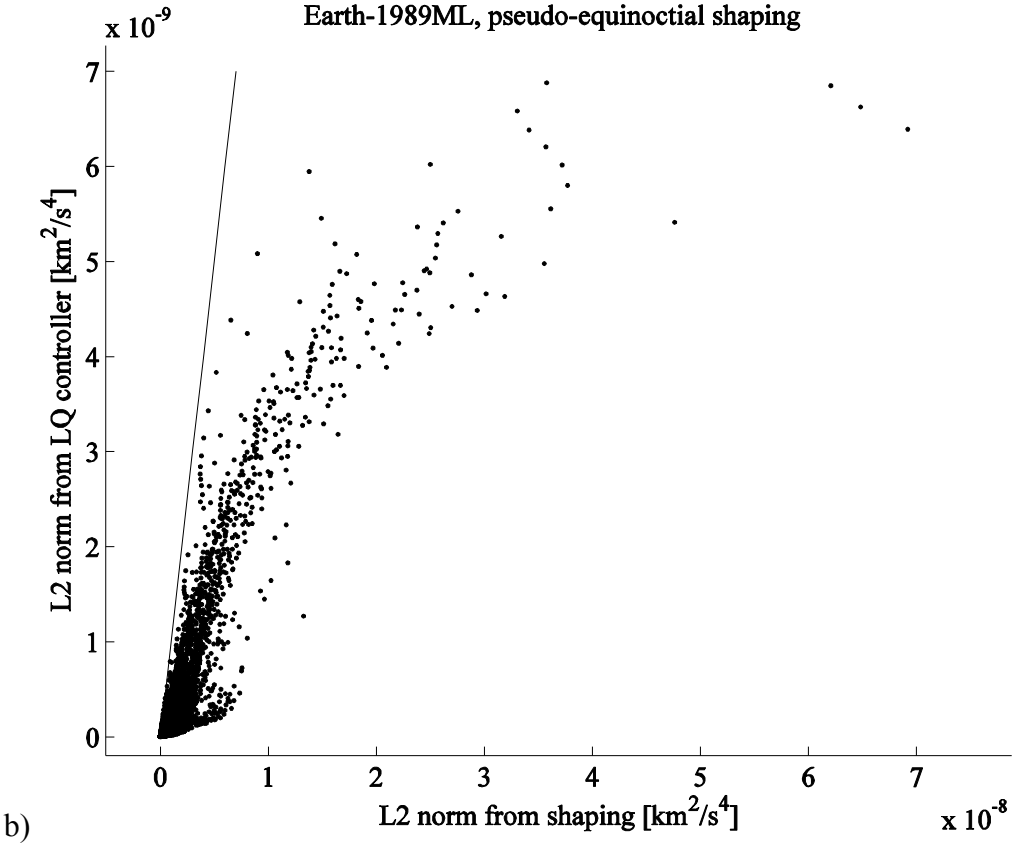

b)

Fig. 3.2: Comparison between the L_2 norms of the controls of the spherical and pseudo-equinoctial shaped transfers and the corresponding LQ-controlled improvement for the 1989ML rendezvous mission. a) Spherical shaping b) Pseudo-equinoctial shaping

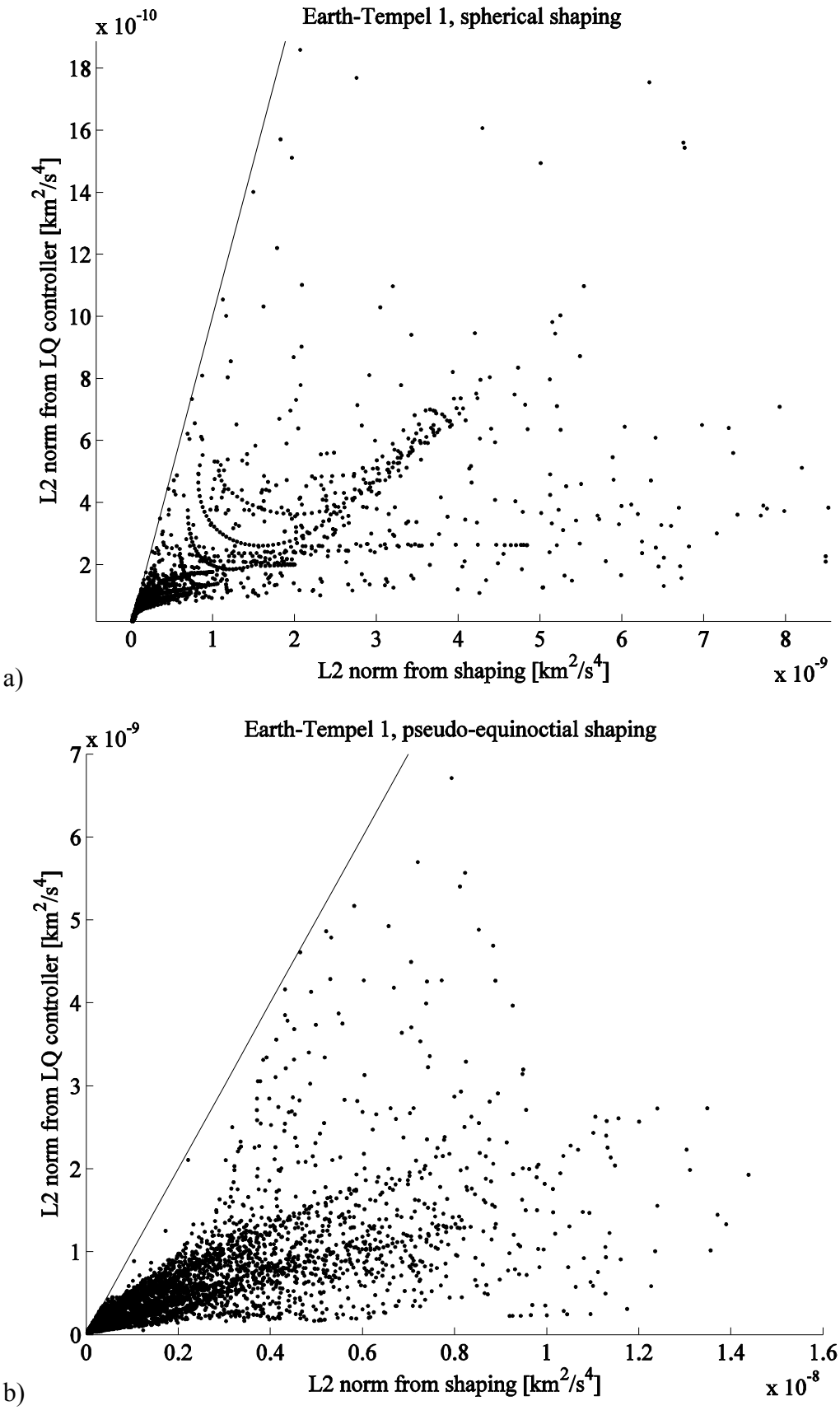

Fig. 3.3: Comparison between the L_2 norms of the controls of the spherical and pseudo-equinoctial shaped transfers and the corresponding LQ-controlled improvement for the Tempel 1 rendezvous mission. a) Spherical shaping b) Pseudo-equinoctial shaping

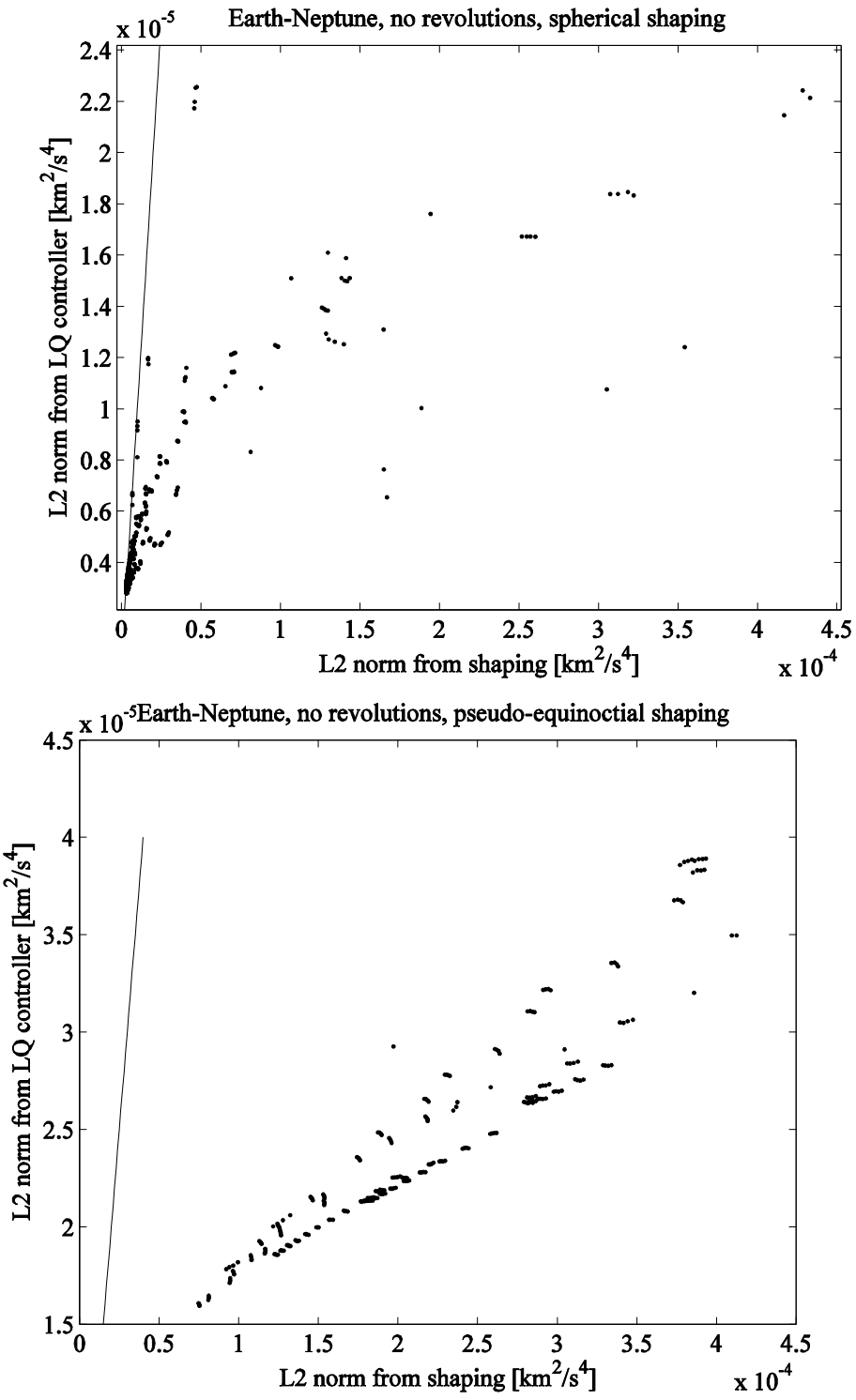

Fig. 3.4: Comparison between the L_2 norms of the controls of the spherical and pseudo-equinoctial shaped transfers and the corresponding LQ-controlled improvement for the Neptune rendezvous mission, without revolutions.

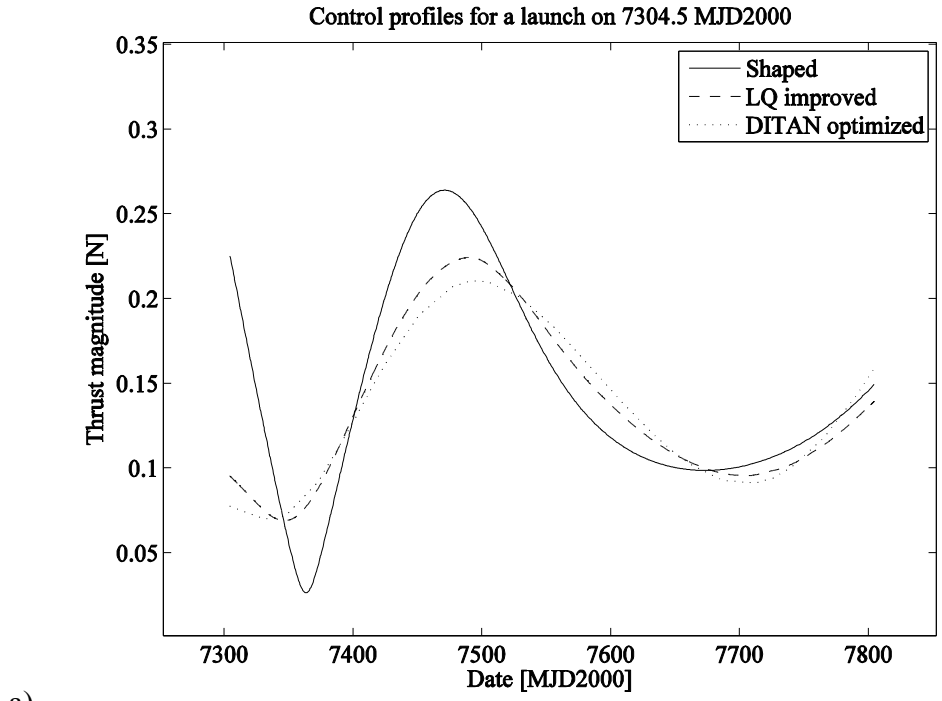

a)

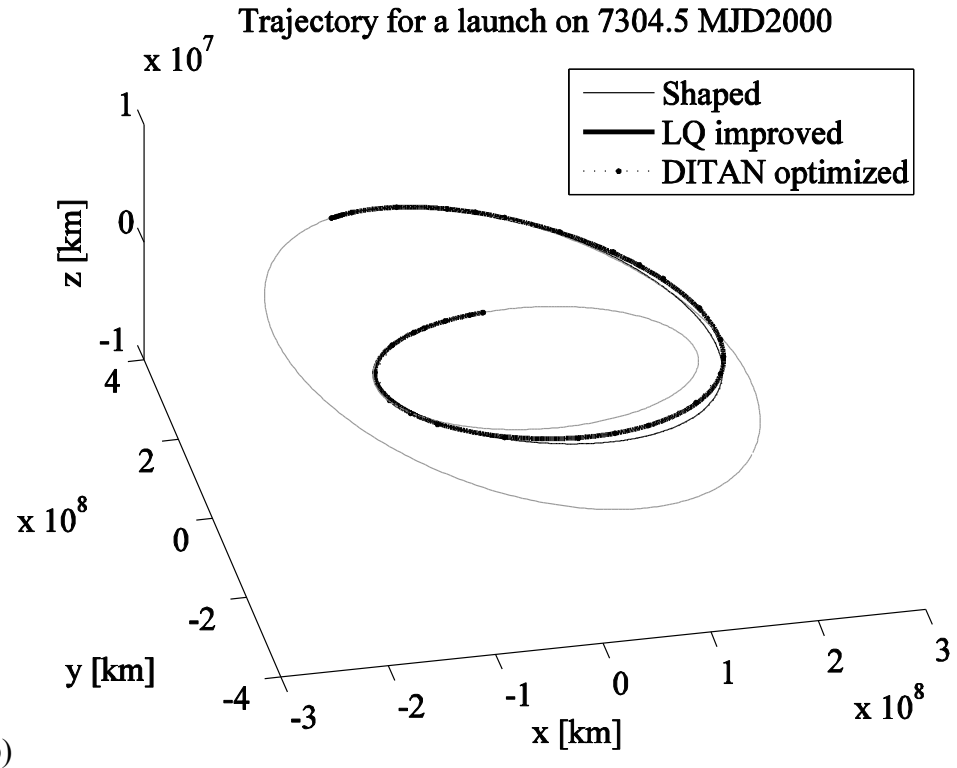

b)

Fig. 3.5: Rendezvous mission to Mars. Comparison between spherical shaped solution, LQ optimised solution and DITAN optimised solution: a) control profile, b) trajectory.

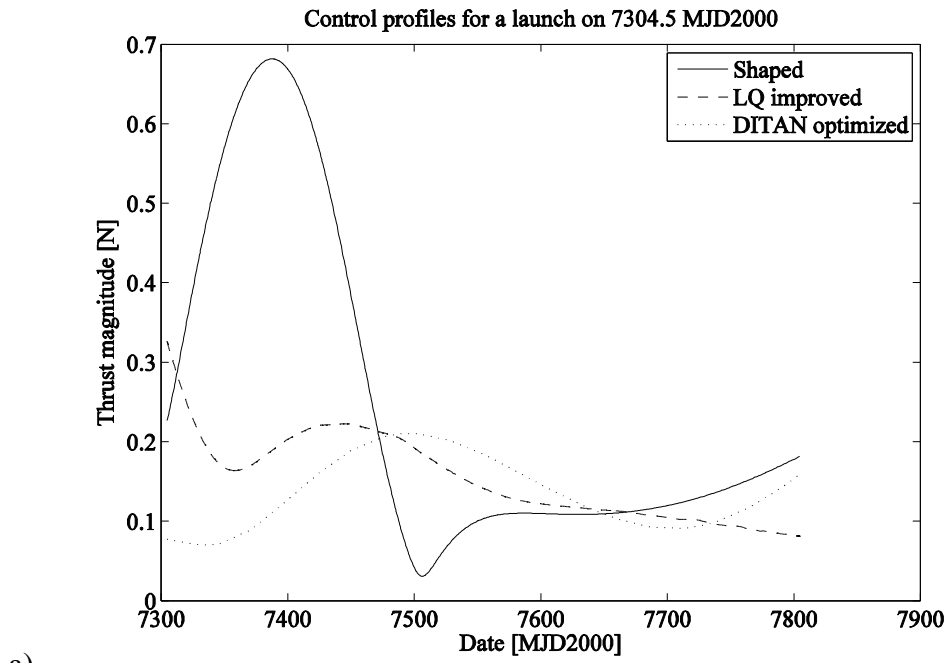

a)

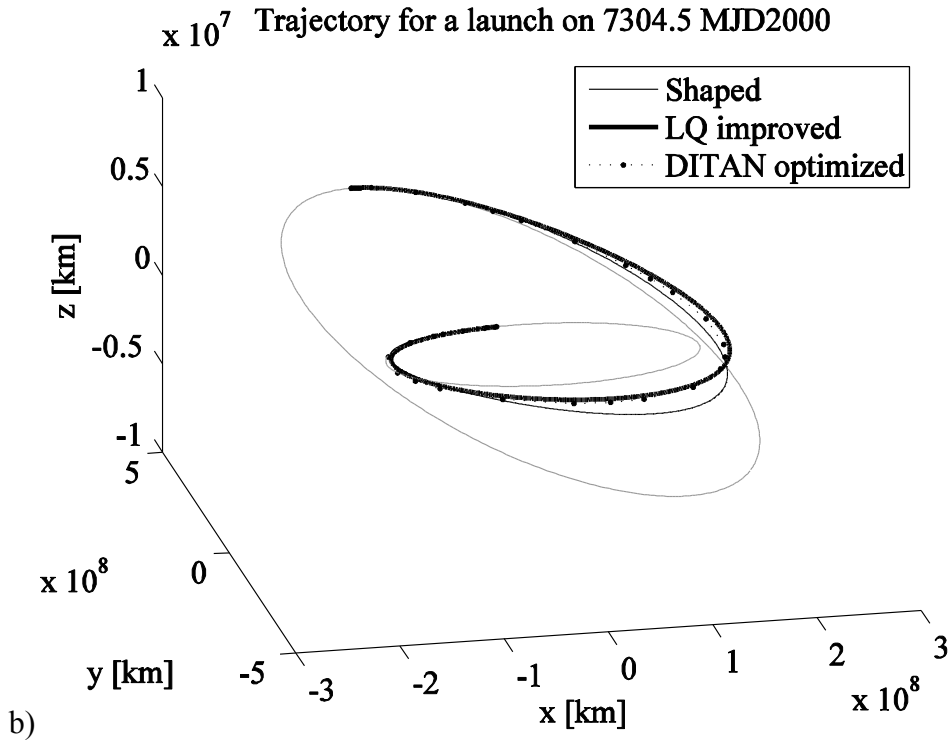

b)

Fig. 3.6: Rendezvous mission to Mars. Comparison between pseudo-equinoctial shaped solution, LQ optimised solution and DITAN optimised solution: a) control profile, b) trajectory.

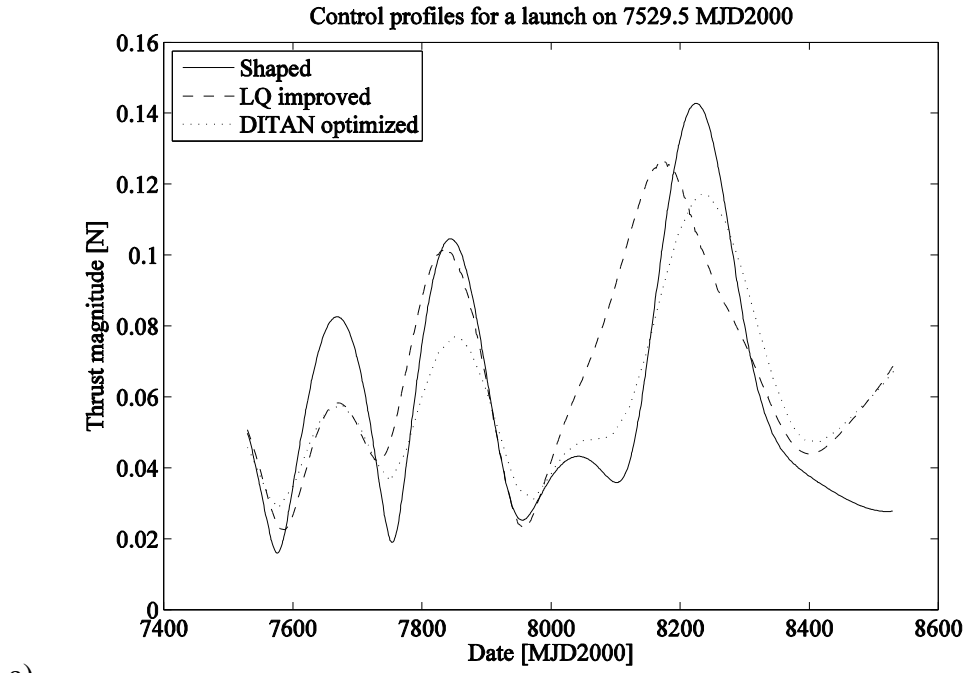

a)

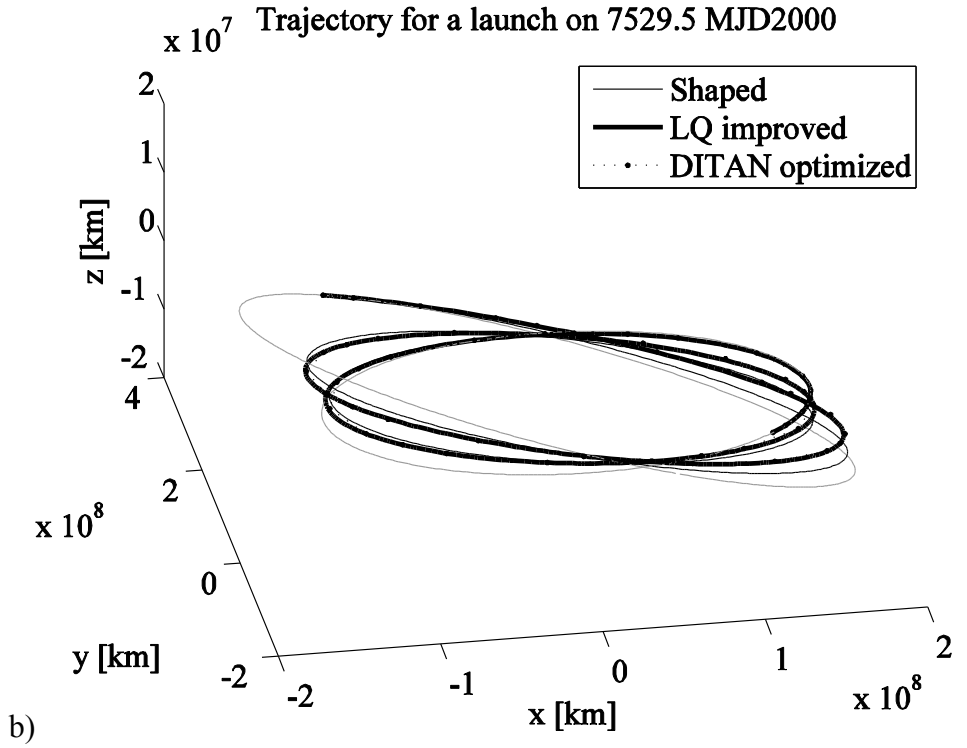

b)

Fig. 3.7: Rendezvous mission to asteroid 1989ML. Comparison between spherical shaped solution, LQ optimised solution and DITAN optimised solution: a) control profile, b) trajectory.

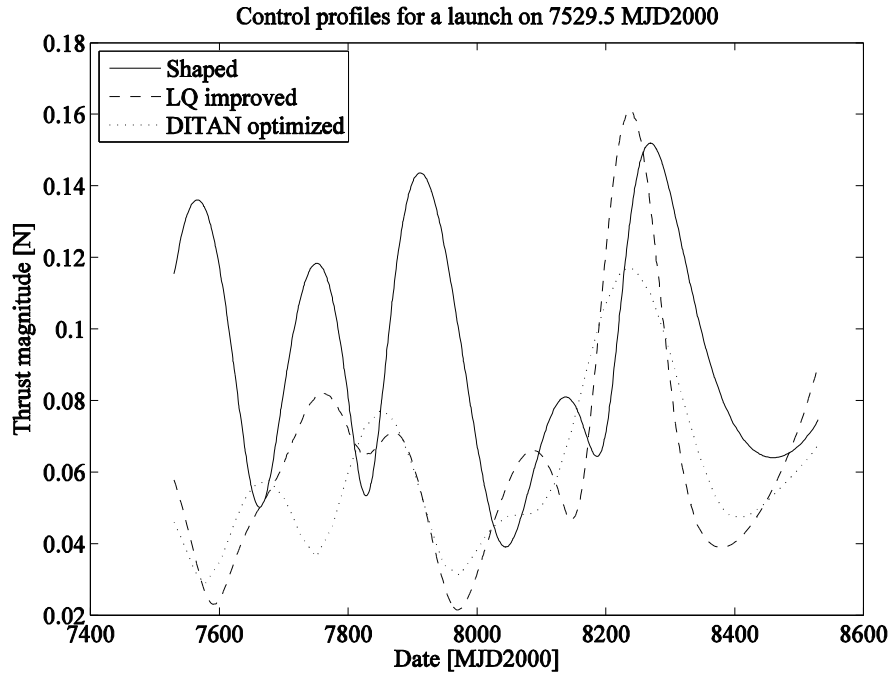

a)

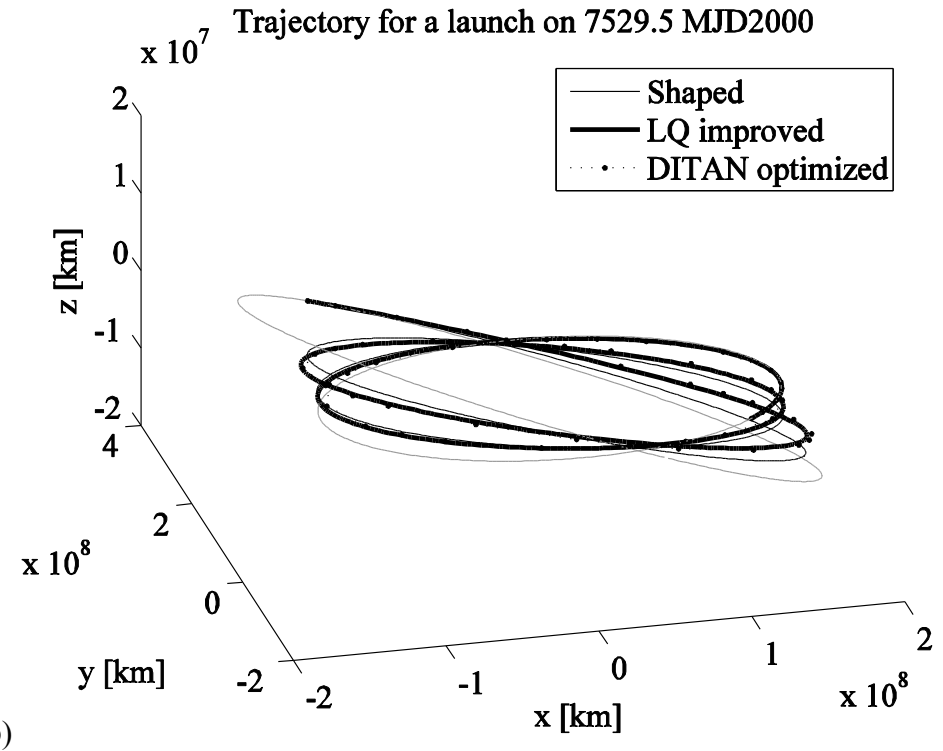

b)

Fig. 3.8: Rendezvous mission to asteroid 1989ML. Comparison between pseudo-equinoctial shaped solution, LQ optimised solution and DITAN optimised solution: a) control profile, b) trajectory.

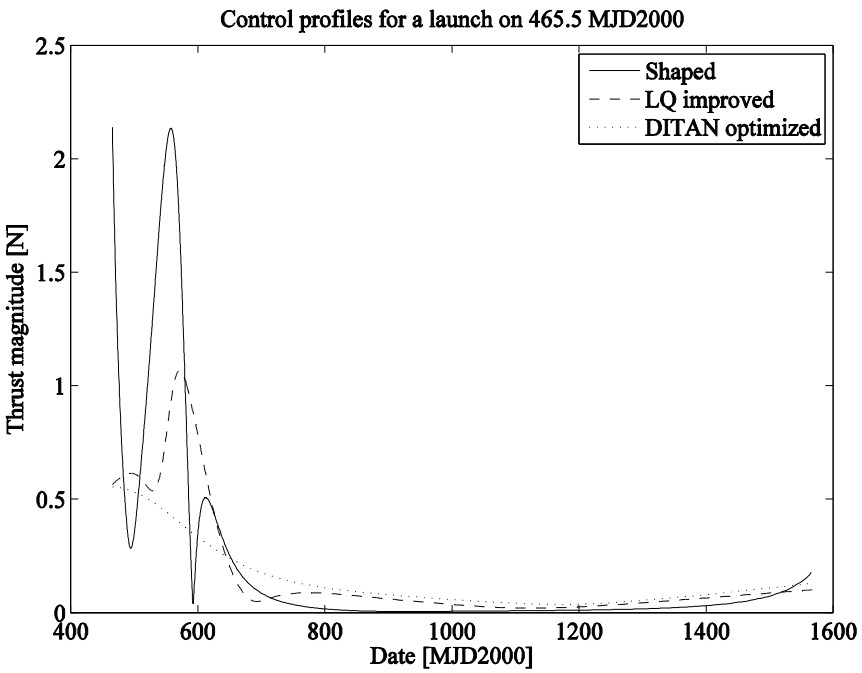

a)

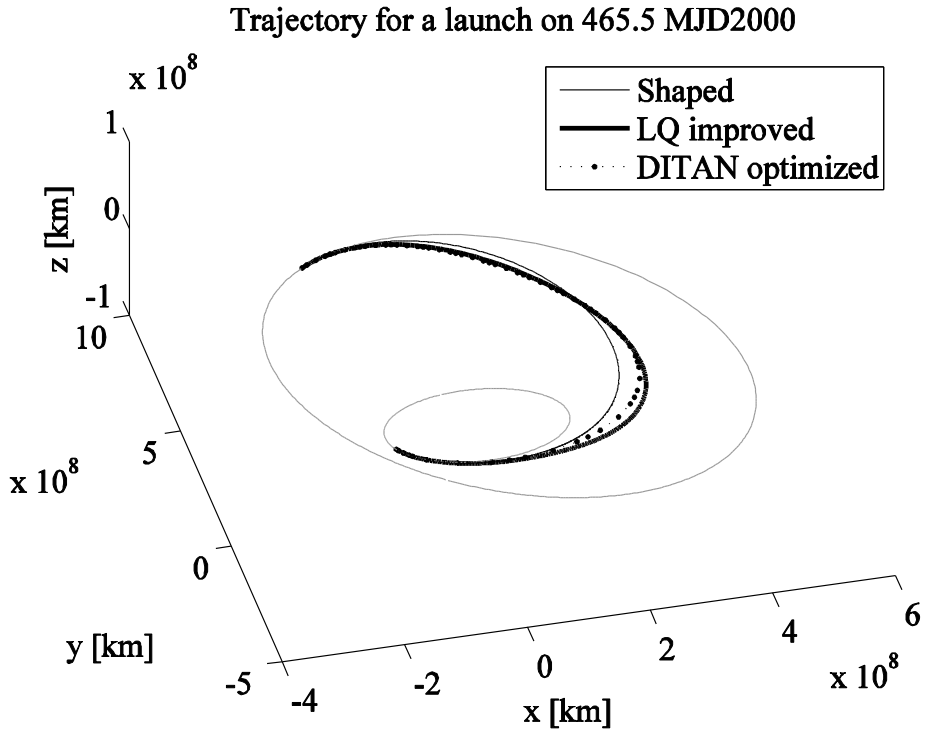

b)

Fig. 3.9: Rendezvous mission to Tempel 1. Comparison between spherical shaped solution, LQ optimised solution and DITAN optimised solution: a) control profile, b) trajectory.

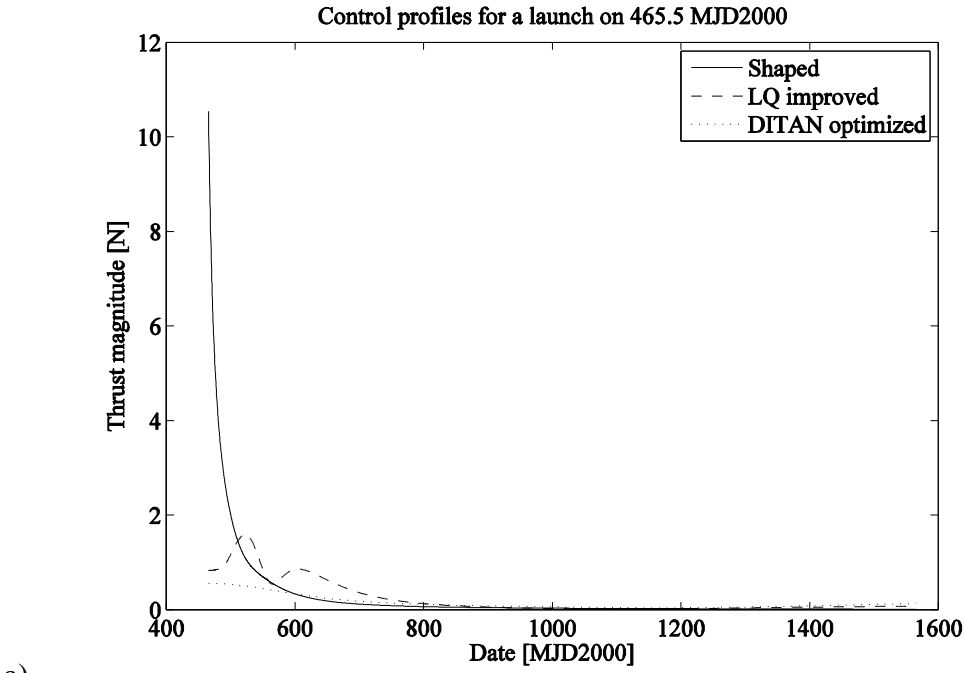

a)

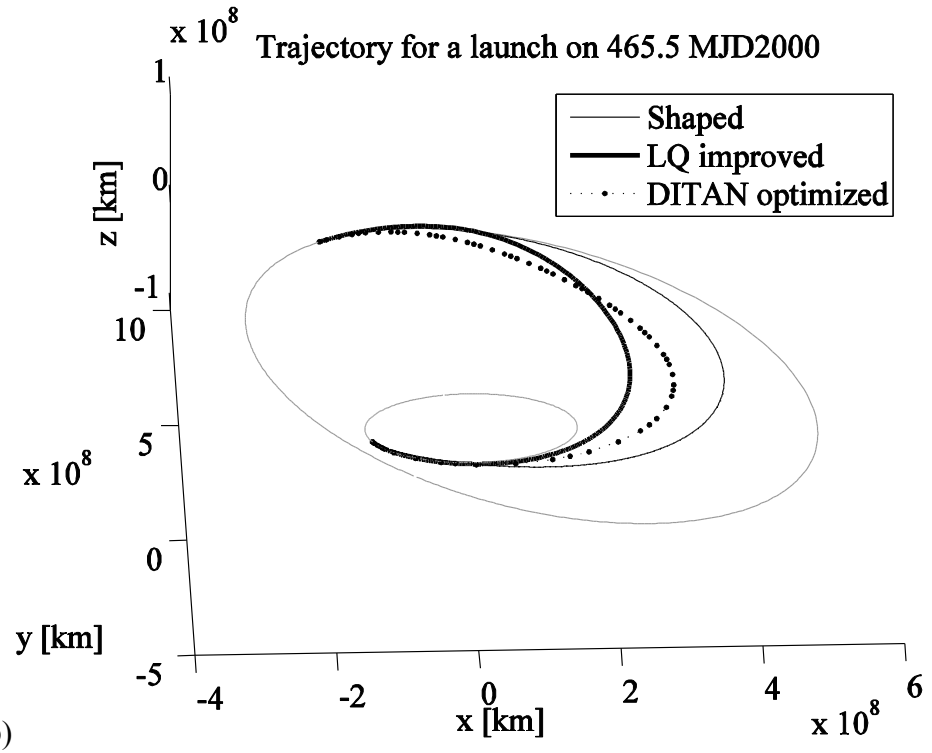

b)

Fig. 3.10: Rendezvous mission to Tempel 1. Comparison between pseudo-equinoctial shaped solution, LQ optimised solution and DITAN optimised solution: a) control profile, b) trajectory.

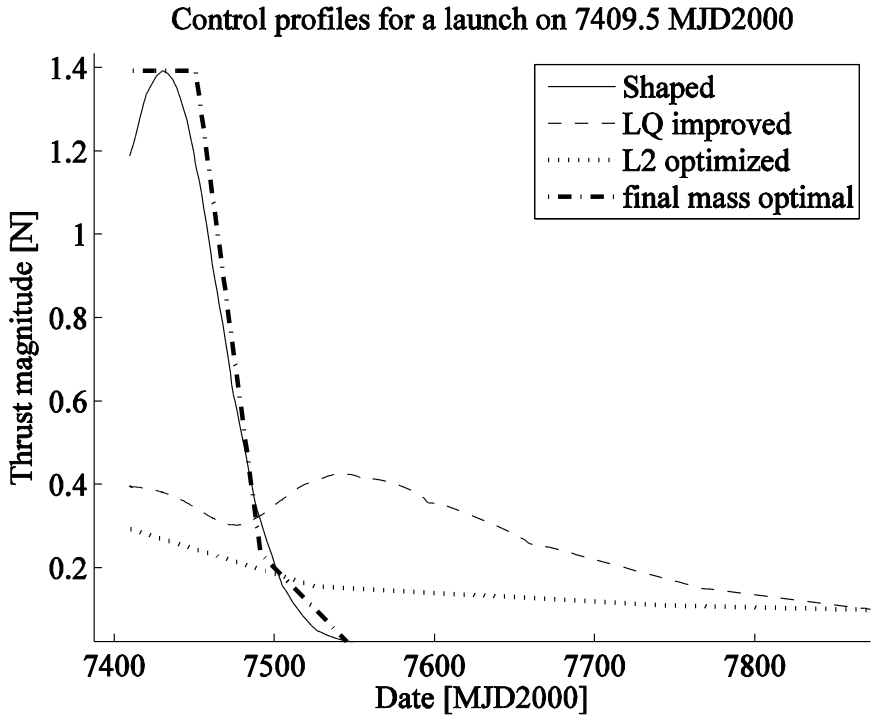
Control profiles for a launch on 7409.5 MJD2000
Shaped
LQ improved
L2 optimized
final mass optimal
Thrust magnitude [N]
1.4
1.2
1
0.8
0.6
0.4
0.2
7400
7500
7600
7700
7800
Date [MJD2000]

a)

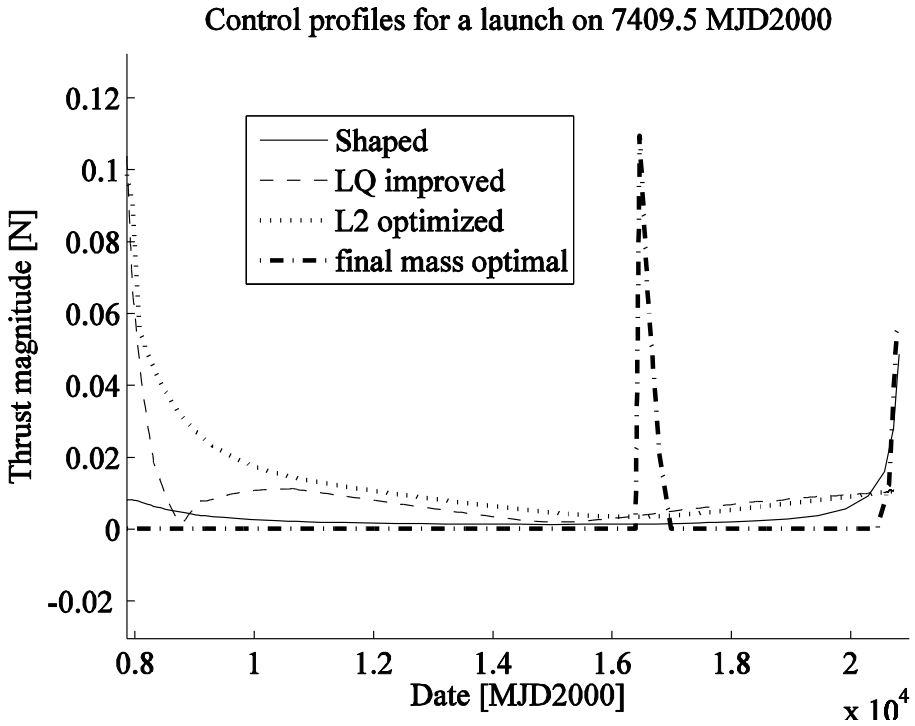
Control profiles for a launch on 7409.5 MJD2000
Shaped
LQ improved
L2 optimized
final mass optimal
Thrust magnitude [N]
0.12
0.1
0.08
0.06
0.04
0.02
0
-0.02
0.8
1
1.2
1.4
1.6
1.8
2
Date [MJD2000]
x 10^4

b)

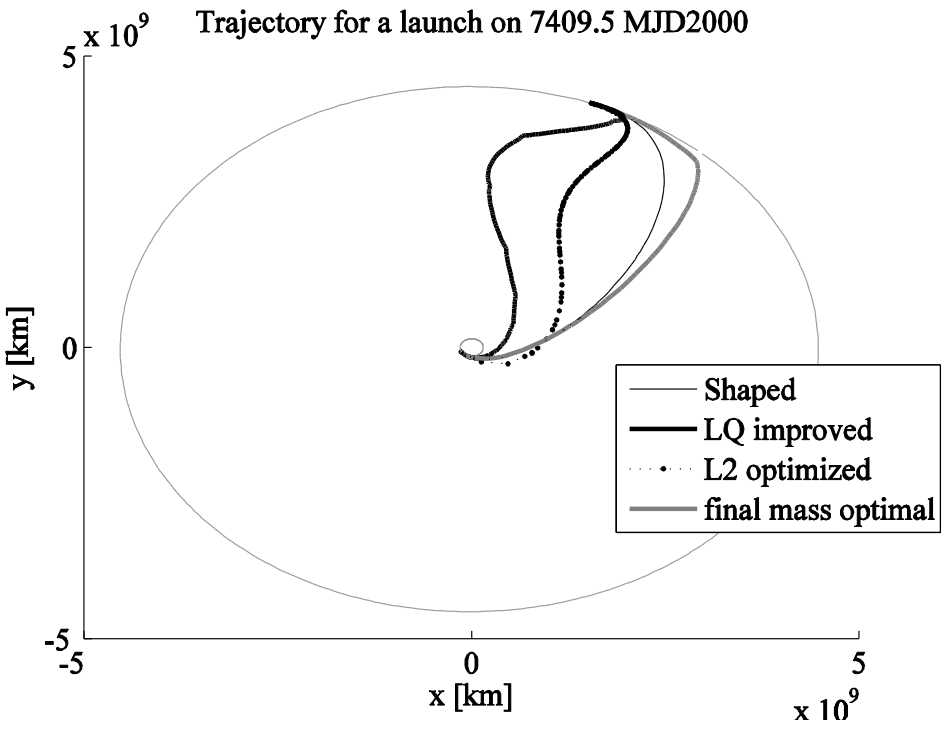

c)

Fig. 3.11: Rendezvous mission to Neptune, with an initial tangential relative velocity of 3 km/s. Comparison between spherical shaped solution, LQ optimized solution and DITAN optimized solution: a) first part of control profile, b) second part of control profile, c) trajectory.

Fig. 3.11 illustrates the thrust profiles and the trajectories corresponding to a typical rendezvous transfer to Neptune. The plots include the results from the spherical shaping, the LQ controller and DITAN for minimal L_2 norm of the thrust and minimal propellant mass. The figures show that the results from the shaping are closer to the ones of the optimal propellant mass trajectory than to the others. The thrust profile of the shaped trajectory is close to being bang-off-bang and the optimal propellant mass trajectory is very similar. However a maneuver is added towards the end of the transfer for a plane change since it is more efficient to perform that maneuver far from the Sun. Note that the bang-off-bang thrust profiles from DITAN would be more pronounced with a higher grid density.

3.5 Computational times

Table 3.1 summarizes the computational times required by each tool used in the present study. The shaping methods require a fraction of a second, depending on the number of times the trajectory is recomputed within the Newton loop in order to satisfy the time of flight constraints. The computational effort required by the LQ

controller is generally one order of magnitude higher, i.e. seconds, than the trajectories generated by shaping. The calculation time depends on the length of the trajectory, and the tolerances used to integrate the Riccati differential equation and the equations of motion. This time also depends on how many points are used to define the reference; the more points provided along the trajectory, the more time the interpolations require for the integrators to calculate each step. The speed of convergence of the low thrust optimizer DITAN generally depends on the initial thrust profile, and varies between 20 and 100 seconds. A better initial guess, i.e. smaller initial constraint violations and proximity to the optimal solution, will generally reduce the number of iterations and therefore the computational time. All times are compute

The shaping approach is mainly affected by the time step used for computing the position and the control as well as to integrate the control to obtain the Δv. The time depends linearly on this step size. The LQ controller also depends linearly on the time step used for the nominal reference trajectory. The DITAN optimiser requires roughly an order of magnitude more time to converge when the tolerances on optimality and feasibility are reduced by an order of magnitude. The processors used were AMD Athlon(tm) 64 Processor 3500+ at 3 GHz running OpenSUSE 11.

Table 3.1: Computational effort required by the different trajectory generating and improving tools used in this study.

	Computational time [s]
Shaping methods	~ 0.1 – 0.3
LQ controller	~ 2 – 6
DITAN optimizer	~ 20 – 100

CHAPTER 4 INCREMENTAL PRUNING FOR LTMGA MISSIONS

Incremental pruning is a technique first proposed by Becerra et al. [33] for finding globally optimum multiple gravity-assist trajectories. The idea is that if one can construct the legs of the MGA transfers independently, then it is possible to prune out whole sets of transfers if one of the legs does not satisfy some required criteria. Constructing and assessing legs one after the other prunes the space of acceptable transfers incrementally. Once the final pruned search space for the full problem is obtained, a global optimisation can be performed on it. It has been shown that applying such a pruning can increase the chance of finding the most promising trajectories.

The issue arising when trying to eliminate the manoeuvre at a swing-by is that successive legs cannot be computed independently, because the outgoing relative velocity at a gravity assist must always be reachable with any incoming relative velocity computed for the previous leg, while assuming that the pericenter is at an altitude above a prescribed value. For example, a necessary condition for linking two relative velocities at a planet by assuming a non-powered swing-by is that the magnitudes of both must be equal.

The Gravity Assist Space Pruning (GASP) algorithm [33] has therefore been modified such that pairs of successive legs are independent instead of individual legs. The low-thrust trajectory model is such that given a departure and arrival date between two successive planets, all the legs arrive with the same velocity, but can depart with different velocities depending on the arrival velocity of the previous leg. The latter property ensures that the pairs of successive legs are independent of the pairs of legs of the previous step.

For the first leg, only Lambert arcs are considered. For each additional leg i, linking planet i to planet $i+1$, the Lambert arcs are first computed, and the initial relative velocity is compared with the previous leg's (leg $i-1$) arrival relative velocity. If the two can be matched, then the Lambert arc is kept, otherwise the initial relative velocity is modified such that no impulse is required at the gravity assist. The leg i is then recomputed with a low-thrust trajectory model which can accommodate the new boundary constraints on velocity. Hence with this approach the departure date t_{i-1} of

leg *i-1* defines the incoming relative velocity at the swing-by at date t_i, which can influence the outgoing relative velocity, while the arrival date t_{i+1} defines the arrival velocity alone.

The model used to compute the outgoing relative velocity from a gravity assist is explained first, followed by the description of the complete LTMGA trajectory design.

4.1 GASP

As introduced by Becerra et al. in their code called GASP, the pruning relies on a systematic search on the discretized search space. The problem is formulated in such a way that the different legs can be constructed independently, but can also be linked together to form complete MGA trajectories. In the initial form of pruning, the legs are Lambert arcs linked together by powered swing-bys. The search space consists of a grid of departure dates, encounter dates for the gravity assist and arrival dates. All the possible Lambert arcs are constructed for the first leg and a pruning of the departure and first gravity-assist dates is performed, based on the magnitude of the initial relative velocity. If there are launch dates for which no Lambert arc is acceptable, then that launch date is pruned out for the problem. In a similar manner, if no Lambert arc is acceptable for a given date for the first gravity-assist, then that date is not considered as starting date for the second leg. In the next step, all possible second legs are constructed except for the dates of first gravity-assist that were pruned out in the previous step. Criteria to prune out the initial and final dates of the second leg are based on the maximum thrust constraints and angular constraints on the incoming and outgoing relative velocities at the first gravity assist.

The following legs are constructed and pruned out similarly to the second leg. A constraint on the relative arrival velocity is imposed during the pruning of the final leg's departure and arrival dates.

After the computation of all the legs and the pruning of departure, gravity assist and arrival dates, an additional forward and backward pruning is performed on the complete space, based on the consideration that if no Lambert arc arrives on a given date for a gravity assist, then that date is not considered as departure date for the next

leg, and if no Lambert arc can depart on a given date, then all Lambert arcs of the previous leg and arriving on that date are pruned out.

Once the grid space of the complete problem is pruned, one recovers the acceptable combinations of intervals for the initial and arrival dates of each leg. One obtains hence so-called boxes, and a global optimization is performed on each one of them. Becerra et al., for instance, applied differential evolution.

The algorithms that make up GASP have been used with trajectory models that are more complex than simple Lambert arcs. GASP has been tested successfully when a deep space maneuver (DSM) is inserted in each leg [43]. DSMs increase the flexibility to design each leg and represent more realistic missions, to the expense of an increased dimension for the search space. The objective in that case is to minimize the sum of the DSMs' Δv and the gravity assists' Δv. Schütze et al. applied GASP with exponential sinusoids [34][44] as trajectory models for the problem of optimizing low thrust MGA transfers. The inconvenience with the latter approach, however, is that one needs to employ powered swing-bys represented by impulsive Δvs, which would suggest both a chemical and a low-thrust propulsion system on board the spacecraft. This constraint is addressed in this paper, by eliminating the need of an impulsive maneuver at the swing-by.

4.2 Gravity assist model

Most often the outgoing relative velocity $\mathbf{v}_{i,rel}^{(i+1)}$ at the beginning of a given leg $i+1$ cannot be matched with the incoming one $\mathbf{v}_{f,rel}^{(i)}$, obtained from the previous leg i, while imposing a minimum pericenter altitude. If that happens, a transformation is applied to the outgoing relative velocity. The new relative outgoing velocity $\mathbf{v}_{i,rel}^{\prime(i+1)}$ is computed such that $\left\|\mathbf{v}_{i,rel}^{\prime(i+1)} - \mathbf{v}_{i,rel}^{(i+1)}\right\|$ is minimal, while constraining it to be attainable with an unpowered swing-by.

It can be first observed that the vector $\mathbf{v}_{i,rel}^{\prime(i+1)}$ with such a property is always in the plane P defined by $\mathbf{v}_{f,rel}^{(i)}$ and $\mathbf{v}_{i,rel}^{(i+1)}$. The case of $\mathbf{v}_{f,rel}^{(i)} = \mathbf{v}_{i,rel}^{(i+1)}$ is rare and corresponds to legs i and $i+1$ that can be matched by a non-powered swing-by with a very high altitude in practice, i.e. no flyby. The case of $\mathbf{v}_{f,rel}^{(i)} = -\mathbf{v}_{i,rel}^{(i+1)}$ is also very rare and the

satellite goes through the planet in that case. If it happens $\mathbf{v}_{i,rel}^{\prime(i+1)}$ is in the plane P defined by $\mathbf{v}_{f,rel}^{(i)}$ and $\mathbf{r}(t_i)$.

The angle δ between $\mathbf{v}_{f,rel}^{(i)}$ and $\mathbf{v}_{i,rel}^{(i+1)}$ is computed, and if it is greater than the maximum deflection angle $\delta_{\max}$ allowed by the gravity assist, defined by [40]:

$$\delta_{\max} = 2\arcsin\frac{1}{1+\frac{r_{p,\min}\left\|\mathbf{v}_{f,rel}^{(i)}\right\|^2}{\mu}}$$

then $\mathbf{v}_{i,rel}^{\prime(i+1)}$ is defined such that its angle with $\mathbf{v}_{f,rel}^{(i)}$ is $\delta_{\max}$. If the line carrying $\mathbf{v}_{f,rel}^{(i)}$ separates the plane P in two, $\mathbf{v}_{i,rel}^{\prime(i+1)}$ points towards the same half-plane as $\mathbf{v}_{i,rel}^{(i+1)}$. $\mathbf{v}_{i,rel}^{\prime(i+1)}$ is then fully defined by assigning it the same magnitude as $\mathbf{v}_{f,rel}^{(i)}$. Fig. 4.1 illustrates this transformation. If $\delta \le \delta_{\max}$ then only the magnitude of $\mathbf{v}_{i,rel}^{(i+1)}$ is adjusted to $\left\|\mathbf{v}_{f,rel}^{(i)}\right\|$, if at all necessary.

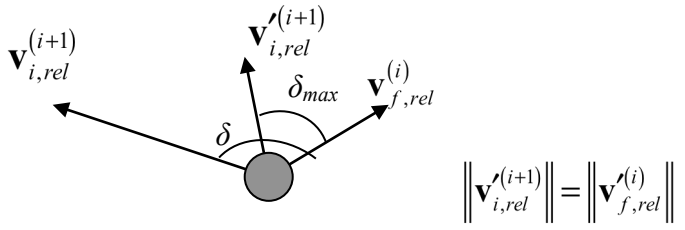

Fig. 4.1: Illustration of the transformation applied to the initial relative velocity of leg *i+1* if it cannot be obtained by a non-powered gravity-assist with incoming relative velocity $\mathbf{v}_{f,rel}^{(i)}$.

4.3 Description of the adapted incremental pruning

The inputs to the problem are the sequence of N planets to be encountered, including the departure one, the launch window W and the range of times of flight $(T_i)_{1\le i\le N-1}$ allowed for each leg of the transfer. The total search space is therefore $I = W \times T_1 \times \cdots \times T_{N-1}$. One constructs recursively N sets $(I_i)_{1\le i\le N}$ starting from $I_1 = W$. I_{i+1} is

the set of possible encounter dates of planet $i+1$ such that the spacecraft can leave planet i at any date whose value is in I_i and flies leg i in a time whose value is in T_i. The induction defining I_i can be written with sets as:

$$\begin{aligned} I_1 &= W \\ I_{i+1} &= I_i + T_i \end{aligned} \tag{4.1}$$

therefore

$$\begin{aligned} \min I_{i+1} &= \min I_i + \min T_i \\ \max I_{i+1} &= \max I_i + \max T_i \end{aligned} \tag{4.2}$$

Subtracting the first equation in (4.2) from the second one yields:

$$\begin{aligned} \max I_{i+1} - \min I_{i+1} &= \max I_i - \min I_i + \max T_i - \min T_i \\ \Delta I_{i+1} &= \Delta I_i + \Delta T_i \end{aligned} \tag{4.3}$$

and then, from the induction formula (4.3) on the amplitude of I_i, one gets:

$$\Delta I_i = \Delta I_1 + \sum_{k=1}^{i-1} \Delta T_k \tag{4.4}$$

This means that the amplitude of I_i grows with i. One also provides a set of N integers $\{k_1,\ldots,k_N\}$ strictly greater than 1, representing the number of points of the grid that discretizes each I_i. The discretised I_i are denoted I_i^d. The spacing between consecutive dates in I_i^d is:

$$\tau_i = \frac{\Delta I_i}{k_i - 1} = \frac{\Delta I_1 + \sum_{k=1}^{i-1} \Delta T_k}{k_i - 1} \tag{4.5}$$

The pruning then acts on the sets of dates $\left(I_i^d\right)_{1 \le i \le N}$. Since the amplitude of I_i grows with i, one would be tempted to augment the number of discretisation points k_i for maintaining τ_i stable, however it is not always necessary. The value of τ_i should generally be compared to the orbital period of planet i because if their ratio is not low enough the possible positions of the planet upon arrival are not well sampled.

Minimum pericenter radii have to be specified for each gravity-assist as well as the number of complete revolutions for each leg. One can then specify varied pruning criteria. These can be upper limits on the magnitude of launch and arrival relative velocities, maximum values of Δv for each leg or maximum thrust magnitude. Further constraints can be on avoidance of conjunction with the Earth during the gravity assist.

The pruning algorithm starts by generating all possible first legs. Three Lambert arcs are computed for each element of $I_1^d \times I_2^d$, one with no revolution, and two with one revolution (the long arc and the short arc). Out of the three Lambert arcs, only the one whose initial relative velocity is lowest is retained. If one of the Lambert arcs has a zero initial relative velocity, which can happen if the first gravity assist planet is identical to the launch planet, then that Lambert arc is discarded. The retained Lambert arc is then assessed for its launch velocity and the element in $I_1^d \times I_2^d$ to which it corresponds is either validated or invalidated. At the end of this step, a set of valid points in $I_1^d \times I_2^d$ is obtained. This set can be denoted V_1^d. Thus $V_1^d \subset I_1^d \times I_2^d$ .If there are dates in I_1^d or in I_2^d for which all Lambert arcs were pruned out, i.e. there are lines or columns in $I_1^d \times I_2^d$ full with invalid transfers, then those dates will not be present in V_1^d and the number of rows or columns of V_1^d will be reduced accordingly. The set of departure and arrival dates for which a valid Lambert arc exists is noted respectively $V_1^d\left(I_1^d\right)$ and $V_1^d\left(I_2^d\right)$ respectively, they are the projections of V_1^d onto I_1^d and I_2^d respectively.

For the second leg, five Lambert arcs are generated for each element of $V_1^d\left(I_2^d\right)\times I_3^d$: one for zero revolutions and the short and long arc for both the one revolution case and the two revolutions case. The retained Lambert arc is the one for which the difference between departure velocity and arrival velocity of the previous leg is smallest but non-zero. The retained Lambert arc therefore depends on the arrival velocity of the first leg's Lambert arc, so one ends up with a new Lambert arc for every element of $V_1^d\left(I_1^d\right)\times V_1^d\left(I_2^d\right)\times I_3^d$. For each of them, the initial relative velocity $\mathbf{v}_{i,rel}^{(2)}$ is compared to the incoming arrival relative velocity vector $\mathbf{v}_{f,rel}^{(1)}$ of the first leg and, if necessary, $\mathbf{v}_{i,rel}^{\prime(2)}$ is constructed with the procedure described in subsection 4.2. Then a shaped trajectory is generated to replace the Lambert arc, such that the initial relative velocity is $\mathbf{v}_{i,rel}^{\prime(2)}$ instead of the Lambert arc's $\mathbf{v}_{i,rel}^{(2)}$. All other boundary conditions are

kept the same. Because of the nature of the trajectory model, the shaping method covers the Keplerian arc and is continuous with respect to the boundary constraints, so the closer $\mathbf{v}'^{(2)}_{i,rel}$ is to $\mathbf{v}^{(2)}_{i,rel}$, the closer the shaped trajectory will be to the Lambert arc. It is important to notice that generating the second leg this way retains the arrival velocity of the Lambert arc at the end of the leg, so the arrival velocity of the second leg does not depend on the first leg. However the initial velocity does, so second legs are fully defined by providing a triplet of dates that are in $V_1^d\left(I_1^d\right)\times V_1^d\left(I_2^d\right)\times I_3^d$. Hence the application that assigns the transfer arc of the second leg to a triplet of dates in $V_1^d\left(I_1^d\right)\times V_1^d\left(I_2^d\right)\times I_3^d$ is surjective.

If $\mathbf{v}^{(2)}_{i,rel}$ can never be matched with $\mathbf{v}^{(1)}_{f,rel}$, one would end up computing a new shaped trajectory for every element of $V_1^d\left(I_1^d\right)\times V_1^d\left(I_2^d\right)\times I_3^d$. Each shaped trajectory is assessed against predefined criteria such as the highest allowed Δv for the leg, resulting in elements of $V_1^d\left(I_1^d\right)\times V_1^d\left(I_2^d\right)\times I_3^d$ being either retained or marked invalid. A first pruning, called backward pruning, is then performed, on the basis that if $t_0 \in V_1^d\left(I_2^d\right)$ all possible second legs departing on $t_0 \in V_1^d\left(I_2^d\right)$, i.e. legs corresponding to dates in $V_1^d\left(I_1^d\right)\times\left\{t_0\right\}\times I_3^d$, are invalid, then that date is pruned out for the rest of the computations and all corresponding elements in V_1^d are marked invalid. In an analogous way, a forward pruning is performed: if all possible first legs arriving on a given date in $V_1^d\left(I_2^d\right)$ are invalid, then that date is pruned out. The same check is performed on arrival dates for the second leg in I_3^d. The sequence of backward and forward prunings results in a new set of valid triplets of dates $V_2^d \subset V_1^d\left(I_1^d\right)\times V_1^d\left(I_2^d\right)\times I_3^d$. The individual encounter dates for which valid second legs exist are therefore the projection of V_2^d onto I_1^d, I_2^d and I_3^d. These can be written $V_2^d\left(I_1^d\right)$, $V_2^d\left(I_2^d\right)$ and $V_2^d\left(I_3^d\right)$ respectively. Note that $V_2^d\left(I_1^d\right)\subset V_1^d\left(I_1^d\right)$, $V_2^d\left(I_2^d\right)\subset V_1^d\left(I_2^d\right)$ and $V_2^d\left(I_3^d\right)\subset V_1^d\left(I_3^d\right)$. If the inclusions are strict, then encounter dates can be pruned out for the remainder of the algorithm.

The trajectories of the following legs are generated and assessed in the same way as those of the second one. A number of departure and arrival dates can then be potentially marked invalid. The effect of this on the rest of the trajectory is propagated by backward and forward pruning. From the way the method is built, legs are decoupled in pairs, instead of individually like in GASP. Indeed, by construction, for

any leg *j+1*, the arrival velocity does not depend on leg *j*. Moreover, the initial velocity of leg *j+1* depends on the arrival velocity of leg *j*, which, from the previous property, does not depend on leg *j-1*. Therefore, in order to construct leg *j+1*, one only needs information from leg *j* that does not depend on previous legs. Hence pairs of consecutive legs are decoupled in the proposed method.

The last leg is treated differently if the objective is to rendezvous with the final celestial body. Indeed, in that case, the Lambert arc is generally not a good initial guess for that leg, because the arrival velocity can be far from the target body's velocity. In that case, a shaped trajectory is generated instead of the Lambert arc, where the initial velocity is unconstrained, and the final velocity is that of the planet. The coefficients a_4, a_6 and b_3 are set to zero in the expressions of R and Φ in (2.51). If the mission objective is not to rendezvous with the target body, then Lambert arcs are generated for the last leg and a further pruning is performed based on the highest acceptable relative velocity upon arrival.

At this point, one has to analyse the distribution of the dates defining the acceptable pairs of consecutive legs. An acceptable pair of legs $(j, j+1)$ will be defined by a triplet of dates (t_j, t_{j+1}, t_{j+2}). The set of all valid triplets, after backward and forward pruning, form V_{j+1}^d. One can then proceed to construct the new continuous search spaces from the pruned discrete ones. For this, the connected components inside every V_{j+1}^d are identified and boxes $BV_{j+1}^{(p)}$ are created around each one of them. Finally, hyperboxes $BV^{(m)} \subset I$ are identified such that an element $(t_1 \dots t_N) \in BV^{(m)}$ has each of its components t_j belonging to one of the $BV_j^{(p)}$ and $BV_{j+1}^{(q)}$:

$$(t_1 \dots t_N) \in BV^{(m)} \Leftrightarrow \begin{cases} \exists p, \quad t_1 \in BV_1^{(p)} \\ \forall j \in [\![2; N-1]\!], \exists (p,q), \quad t_j \in BV_{j-1}^{(p)} \cap BV_j^{(q)} \\ \exists p, \quad t_N \in BV_{N-1}^{(p)} \end{cases}$$

The hyperboxes $BV^{(m)}$ are disconnected subsets of I, and one of them is expected to contain the global optimum. However, due to the discretised approach to the pruning, this is not necessarily the case, even though the probability for that can be raised.

One can apply a global optimisation algorithm on each hyperbox. In this study, the differential evolution algorithm *devec3* of Matlab was employed. When applying it,

the LQ controller was called after the shaping for the last leg in order to improve the rendezvous with the destination planet.

Finally, the best trajectories were locally optimised with the low thrust trajectory optimizer called DITAN. DITAN transcribes the optimal control problem into finite elements in time and uses collocation. The objective was to maximize the final mass at arrival and a constraint was set for the maximum thrust to be the value of the maximum thrust of the shaped trajectory used as initial guess.

4.4 Computational effort

During the pruning, the part that takes by far the most time is the generation of the shaped trajectory. The computational effort for a Lambert arc is negligible compared to it. The trajectory shaping is called from the second leg onward. If one discretizes the initial and arrival dates of the leg into k points, as well as the previous leg's initial dates, then the shapes are called potentially k^3 times. This is the case for all the legs except the first and the last, which adds up to $(N-1)k^3$ calls to the shaping. In the final leg there are up to two calls to the trajectory shaping for each node, adding up to $8k^3$ calls. So in total, the shaping is called at most $(N+7)k^3$ times. The latter formula provides the number of times the shaping is called if no pruning is applied and is therefore a considerable over-estimation of the real number of calls to the shaping. Moreover, the possibility of overlapping between intervals of encounter dates is not accounted for, whereby the arrival date can be earlier than the departure date, in which case the transfer arc is not generated. The effect of the latter on the pruning of the dates can be approximated using the inputs.

To find the approximation, it is assumed that one wants to compute the transfer arcs for leg i for all possible departure and arrival dates. If $\min I_{i+1}^d < \max I_i^d$, then the number of calls to compute the transfer arc is simply $k_i k_{i+1}$. If there is an overlap between I_i and I_{i+1} then the number of calls is smaller because some departure dates in I_i^d are after some arrival dates in I_{i+1}^d. In that case, according, as illustrated in Fig. 4.2, I_i^d is split into two sets A and B, and I_{i+1}^d into C and D. Note that $\Delta B = \Delta C$. Transfers are computed for every case where the departure date is in A and the arrival in I_{i+1}^d. These amount to $N_{i1} = |A| k_{i+1} = \left(k_i - |B|\right) k_{i+1}$ calls. In the case when the departure

date is *B*, the number of calls is approximated by (4.6). The accuracy of the approximation rises with the number of elements in *B* and *C*.

$$\begin{aligned} N_{i2} &\simeq \left(k_{i+1} - \frac{\tau_i}{\tau_{i+1}}\right) + \left(k_{i+1} - 2\frac{\tau_i}{\tau_{i+1}}\right) + \cdots + \left(k_{i+1} - |B|\frac{\tau_i}{\tau_{i+1}}\right) \\ &\simeq |B| k_{i+1} - \frac{1}{2}\frac{\tau_i}{\tau_{i+1}}|B|^2 \end{aligned} \tag{4.6}$$

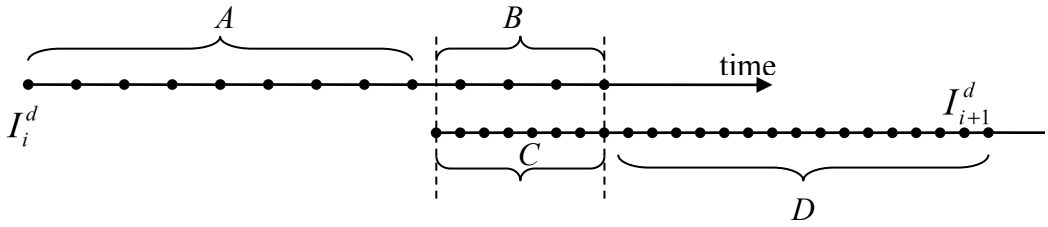

Fig. 4.2: Illustration of departure dates I_i^d and arrival dates I_{i+1}^d for leg *i*, when the ranges covered by the two overlap each other.

The total number of calls is then close to:

$$\begin{aligned} N_i &= N_{i1} + N_{i2} \\ &\simeq k_i k_{i+1} - \frac{1}{2}\frac{\tau_i}{\tau_{i+1}}|B|^2 \end{aligned} \tag{4.7}$$

since

$$|B| \simeq \frac{\max I_i - \min I_{i+1}}{\tau_i} = \frac{\Delta I_i - \min T_i}{\tau_i} \tag{4.8}$$

and from (4.5) $\tau_i \simeq \frac{\Delta I_i}{k_i}$, the following expression is obtained for N_i:

$$N_i = k_i k_{i+1}\left(1 - \frac{\beta_i^+ \beta_{i+1}^-}{2}\right) \tag{4.9}$$

where

$$\begin{aligned}\beta_i^+ &= \frac{\Delta I_i^d - \min T_i}{\Delta I_i^d} \simeq \frac{\Delta B}{\Delta I_i^d} \\ \beta_{i+1}^- &= \frac{\Delta I_i^d - \min T_i}{\Delta I_{i+1}^d} \simeq \frac{\Delta C}{\Delta I_{i+1}^d}\end{aligned} \tag{4.10}$$

So for a leg *i*, an overlap between the range of departure and arrival dates results in a reduction of the number of possible transfers represented by the factor α_i:

$$\alpha_i = 1 - \frac{\beta_i^+ \beta_{i+1}^-}{2} \tag{4.11}$$

Expression (4.11) is remarkable in the sense that it does not include information about the density of either I_i^d and I_{i+1}^d. As a matter of fact, it could also have been obtained by reasoning on continuous intervals of dates instead of discrete sets, after assuming that $k_i \gg 1$ and $k_{i+1} \gg 1$:

$$\begin{aligned}\alpha_i &= \frac{\iint_{\mathbb{R}^2} \mathbf{1}_{I_i}(t)\mathbf{1}_{I_{i+1}}(u)\mathbf{1}_{[t;+\infty)}(u)\,du\,dt}{\iint_{\mathbb{R}^2} \mathbf{1}_{I_i}(t)\mathbf{1}_{I_{i+1}}(u)\,du\,dt} \\ &= \frac{1}{\Delta I_i \Delta I_{i+1}}\left(\int_0^{\Delta I_i}\int_{\max(t,\min I_{i+1})}^{\max I_{i+1}} du\,dt\right) \\ &= \frac{1}{\Delta I_i \Delta I_{i+1}}\left(\int_0^{\min I_{i+1}}\int_{\min I_{i+1}}^{\max I_{i+1}} du\,dt + \int_{\min I_{i+1}}^{\Delta I_i}\int_t^{\max I_{i+1}} du\,dt\right) \\ &= \frac{1}{\Delta I_i \Delta I_{i+1}}\left(\left(\Delta I_i - \Delta B\right)\Delta I_{i+1} + \int_{\min I_{i+1}}^{\Delta I_i}\int_t^{\max I_{i+1}} du\,dt\right) \\ &= \frac{1}{\Delta I_i \Delta I_{i+1}}\left(\left(\Delta I_i - \Delta B\right)\Delta I_{i+1} + \int_0^{\Delta B}\int_t^{\Delta I_{i+1}} du\,dt\right) \\ &= \frac{1}{\Delta I_i \Delta I_{i+1}}\left(\Delta I_i \Delta I_{i+1} - \Delta B \Delta I_{i+1} + \int_0^{\Delta B}\left(\Delta I_{i+1} - t\right)dt\right) \\ &= \frac{1}{\Delta I_i \Delta I_{i+1}}\left(\Delta I_i \Delta I_{i+1} - \Delta B \Delta I_{i+1} - \left[\frac{\left(\Delta I_{i+1} - t\right)^2}{2}\right]_0^{\Delta B}\right) \\ &= \frac{1}{\Delta I_i \Delta I_{i+1}}\left(\Delta I_i \Delta I_{i+1} - \Delta B \Delta I_{i+1} - \frac{\left(\Delta I_{i+1} - \Delta B\right)^2}{2} + \frac{\Delta I_{i+1}^2}{2}\right) \\ &= \frac{1}{\Delta I_i \Delta I_{i+1}}\left(\Delta I_i \Delta I_{i+1} - \frac{\Delta B^2}{2}\right) \\ &= 1 - \frac{\beta_i^+ \beta_{i+1}^-}{2}\end{aligned} \tag{4.12}$$

Hence, before considering any pruning, the real number of calls to the shaping is generally a fraction of $(N+7)k^3$. If transfer arcs are pruned according to given criteria, that fraction becomes even lower, according to how stringent the conditions are. It is

difficult to quantify a priori the effect of the pruning criteria on the final number of calls to the trajectory shaping, unless one has a statistical model of the parameters on which the pruning is based with respect to initial conditions, final conditions and times of flight.

If one assumes that at least a fraction α of the k encounter dates is always pruned out, after considering consistency of encounter dates, pruning on user-defined criteria and backward and forward pruning, then the number of calls to the trajectory shaping function will be at most $(N+7)k^3/\alpha^3$.

4.5 Test cases

This section presents the test cases to which the shaping and the new incremental pruning was applied to. Rendezvous missions are presented from Earth to Apollo and Jupiter. The search space was pruned out incrementally and a differential evolution algorithm was run on each connected component of the pruned space. The differential algorithm operated on a population 10 times the size of the search space's dimension. The population evolved over 20 generations. Different values were tested for the two parameters and these values were retained because they turned out to result in the algorithm converging in the test cases presented below while keeping the computational effort reasonably low.

The low thrust trajectory optimizer DITAN was employed to find the transfer with the lowest propellant consumption. DITAN is a local optimizer and transcribes the problem into finite elements of time and uses collocation to model the evolution of the state and control vectors. A limit on the thrust magnitude was set each time, its value being the peak thrust value of the initial guess trajectory. The initial mass of the spacecraft was set to 1000 kg and the specific impulse of its propulsion system to 3000 s. The initial relative velocity at launch was limited to 5 km/s.

The computations were performed on Intel Xeon processors clocked at 2.67 GHz and running Linux Centos 5.4 operating system.

4.5.1 Earth-Earth-Apollo rendezvous

As a first test for the pruning algorithm, a rendezvous to asteroid Apollo was chosen with a single flyby at the Earth. The selection of the asteroid was based mainly on the high eccentricity of its orbit, making the search for gravity assist transfers relevant. Apollo's orbital elements are reported in Table 4.1.

Table 4.1 Orbital elements of Asteroid Apollo

Semi-major axis	1.471 AU
Eccentricity	0.56
Inclination	6.4°
Ascending node	25.9°
Argument of pericenter	285.7°

The mission scenario has two legs, which makes the search space of dimension 3. The launch window W was set to be the interval between 1st January 2010 and 1st January 2015. W was discretised into 240 equidistant dates, i.e. in average three launch dates per month. The first leg's range of times of flight was set between 200 days and 800 days and the range of dates for the gravity assist was discretised into 250 dates, the second leg's time of flight took values in [200 d ; 1000 d] and the range of rendezvous dates was discretised into 300 equidistant values. The initial relative velocity was allowed to be 5 km/s maximum and a limit was set on the second leg's total Δv to 10 km/s. Therefore only two criteria were used to prune out the search space. The minimal altitude allowed for the gravity-assist at Earth was 200 km. The pruned pairs of legs are plotted in Fig. 4.3.

In total, 29 separate hyperboxes were obtained by the pruning after 8.5 hours of computation, and a differential evolution algorithm was run on all of them, in order to locate the global minimum, taking 8.9 minutes each.

The trajectory with the lowest Δv obtained from the DE turned out to be of 5.32 km/s with an initial launch velocity of 4.93 km/s. One should note that part of the Δv of the low thrust transfer includes gravity-loss. The total time of flight is 3.17 years. The local optimisation with DITAN resulted in a transfer also lasting 3.17 years and requiring 4.49 km/s of Δv and an initial launch velocity of 5.00 km/s. Table 4.2 provides the dates of encounter of each planet for the best trajectory.

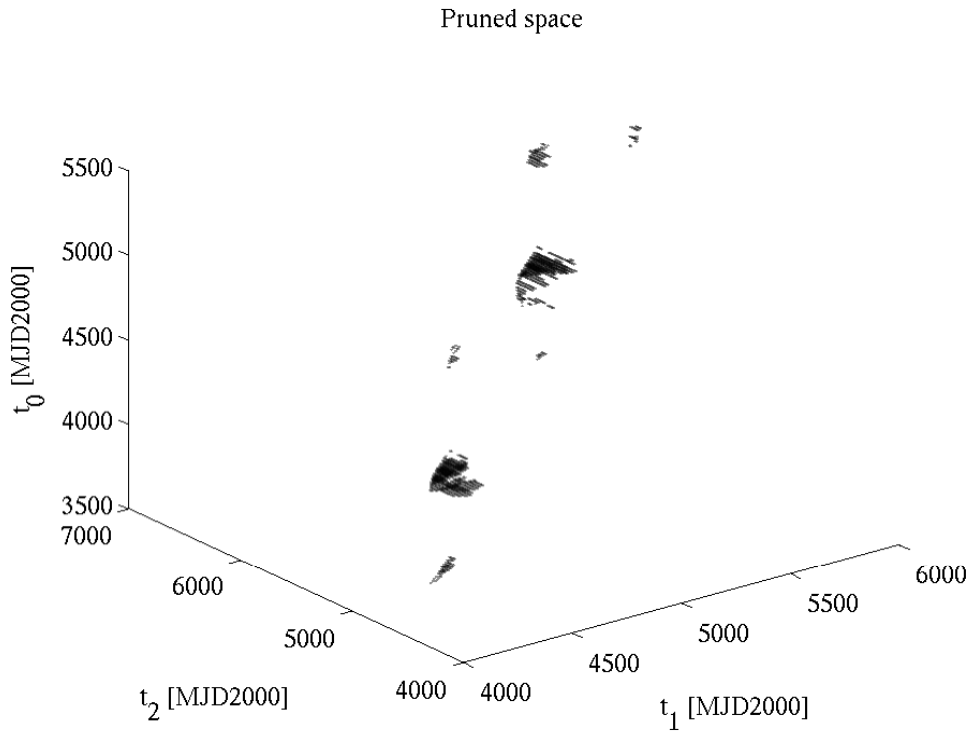

Fig. 4.3: Plotted are the triplets of dates, corresponding to the pair of Earth-Earth-Apollo legs, that were not pruned

Table 4.2 Dates at each planet for the LTMGA trajectory with the lowest Δv.

	Date from DE	Date from DITAN
Launch from Earth	9/2/2011	19/3/2011
Earth GA	27/7/2012	4/9/2012
Rendezvous at Apollo	12/4/2014	20/5/2014

Fig. 4.4 shows that the optimised transfer is close to the initial guess one. After launch, the spacecraft coasts for more than one revolution and performs a flyby of Earth. The flyby occurs close to the line of apsides of Apollo, on the side of the pericenter. The flyby raises the apocenter of the trajectory, such that the thrust in the Earth-Venus leg is predominantly about reducing the pericenter. The gravity assist has thus a beneficial effect, reducing the necessary total Δv for the rendezvous.

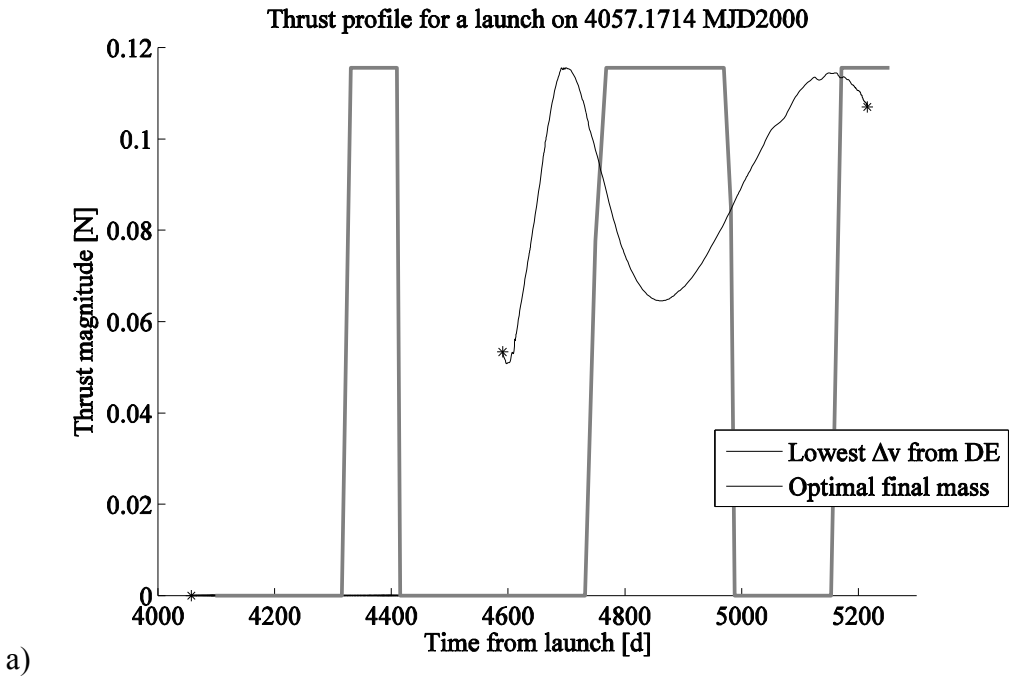

a)

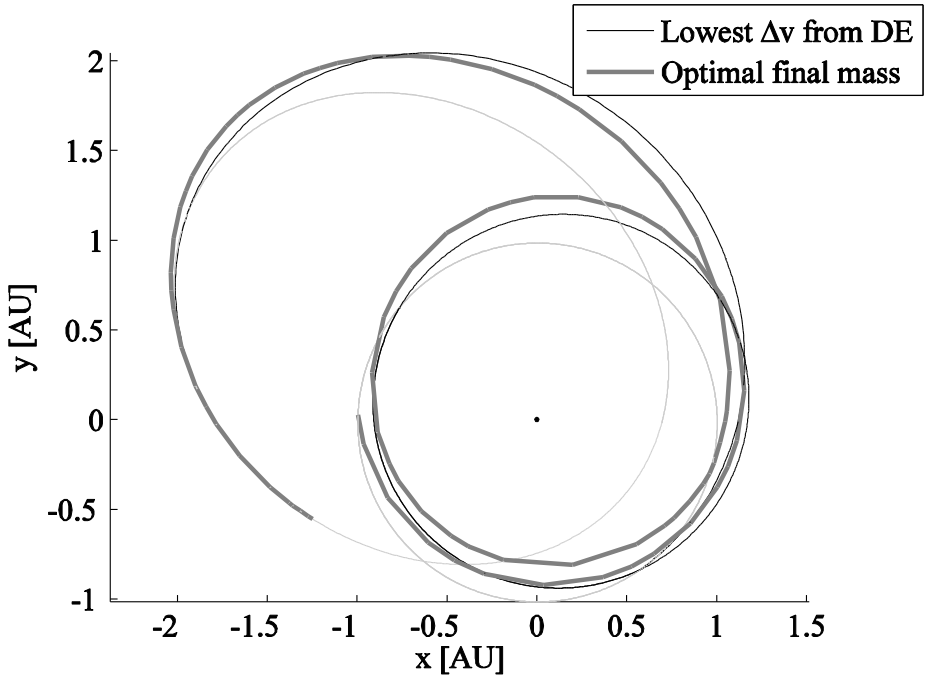

b)

Fig. 4.4: Result from DE with the lowest Δv and its optimised solution from DITAN, a) thrust profile, b) trajectory plot

4.5.2 Earth-Venus-Earth-Apollo rendezvous

Analysing the results obtained in subsection 4.5.1 for the rendezvous with asteroid Apollo suggests that inserting an additional gravity assist that reduces the pericenter of the spacecraft's orbit to that of asteroid's can be beneficial. The pericenter of the

asteroid is at 0.65 AU from the Sun, therefore an initial flyby at Venus was envisaged since its pericenter is at 0.72 AU.

The mission scenario has three legs, so the dimension of the search space is four. The launch window W was set again to be the interval between 1st January 2010 and 1st January 2015 and was discretised into 240 equidistant dates, i.e. in average three launch dates per month. The Earth-Venus leg's range of times of flight was set to [100 d ; 500 d] and the range of encounter dates of Venus was discretised into 250 points, the second leg's time of flight spanned [50 d ; 700 d] and the interval of dates for the Earth gravity assist was discretised into 250 equidistant dates. The final leg's time of flight was in the range [200 d ; 1000 d] and the range of possible arrival dates was discretised into 300 equidistant dates. The initial relative velocity was allowed to be 5 km/s maximum and a limit was set on the second leg's Δv to 10 km/s and on the third leg's Δv to 10 km/s. Three criteria were used to prune out the search space. The minimal altitude allowed for both gravity assists 200 km. The pruned pairs of legs are plotted in Fig. 4.5.

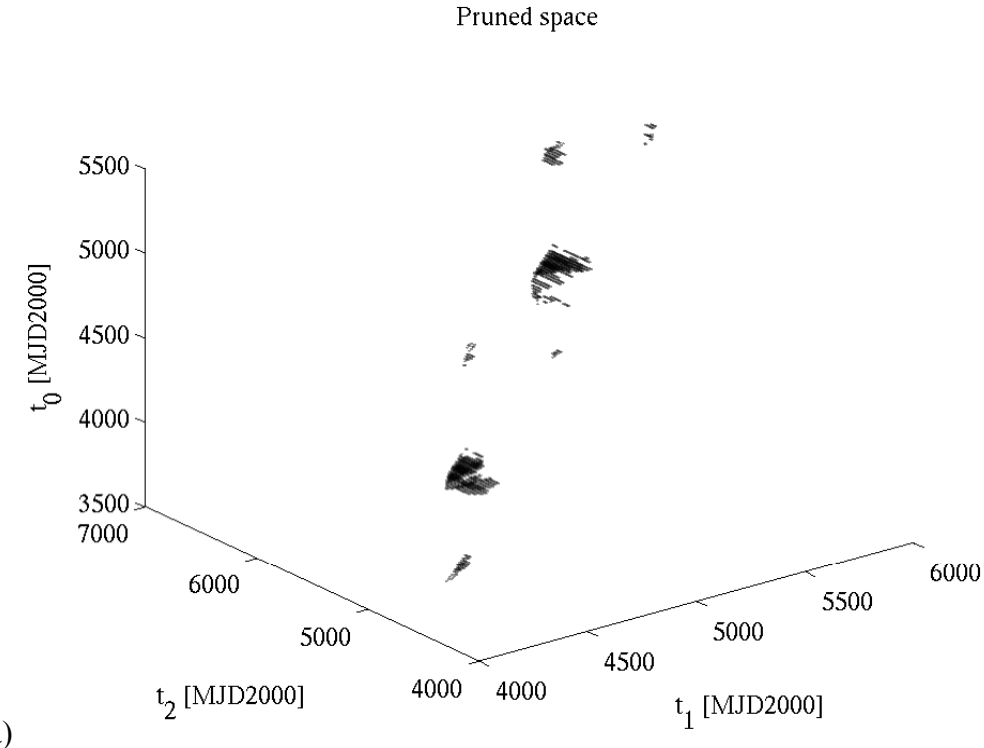

a)

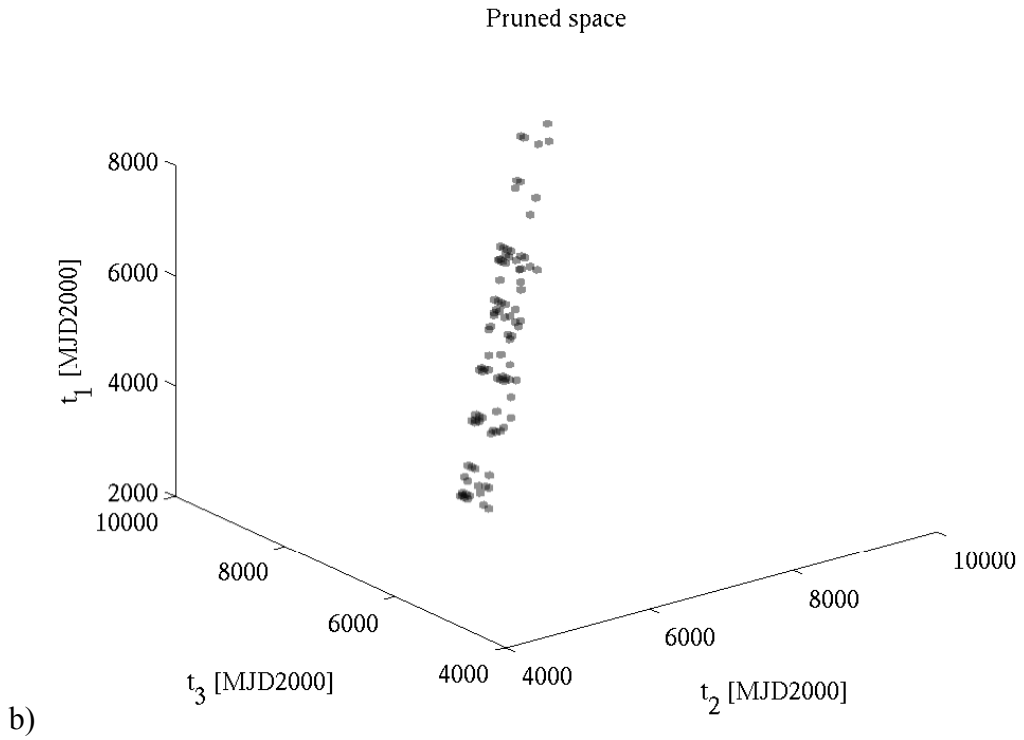

b)

Fig. 4.5: Plotted are the triplets of dates, corresponding to the pair of a) Earth-Venus-Earth legs and b) Venus-Earth-Apollo legs, that were not pruned

In total, 13 separate hyperboxes were obtained by the pruning after 1.21 days of computation, and a differential evolution algorithm was run on all of them, in order to locate the global minimum, taking 34 minutes in average each.

The trajectory with the lowest Δv obtained from the DE turned out to be of 2.21 km/s with an initial launch velocity of 4.24 km/s. One should note that part of the Δv of the low thrust transfer includes gravity-loss. The total time of flight is 4.59 years. The local optimisation with DITAN resulted in a transfer lasting 4.65 years and requiring 1.61 km/s of Δv and an initial launch velocity of 5.00 km/s. Table 4.3 provides the dates of encounter of each planet for the best trajectory.

Table 4.3 Dates at each planet for the LTMGA trajectory with the lowest Δv.

	Date from DE	Date from DITAN
Launch from Earth	15/2/2010	13/1/2010
Venus GA	4/4/2011	30/3/2011
Earth GA	19/10/2012	14/10/2012
Rendezvous at Apollo	20/9/2014	9/9/2014

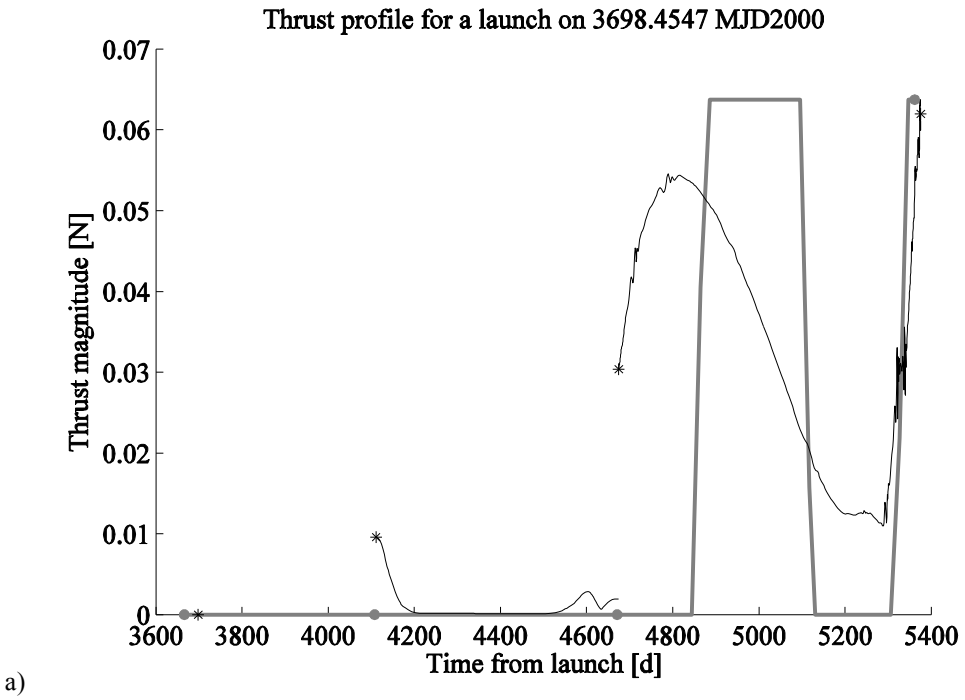

a)

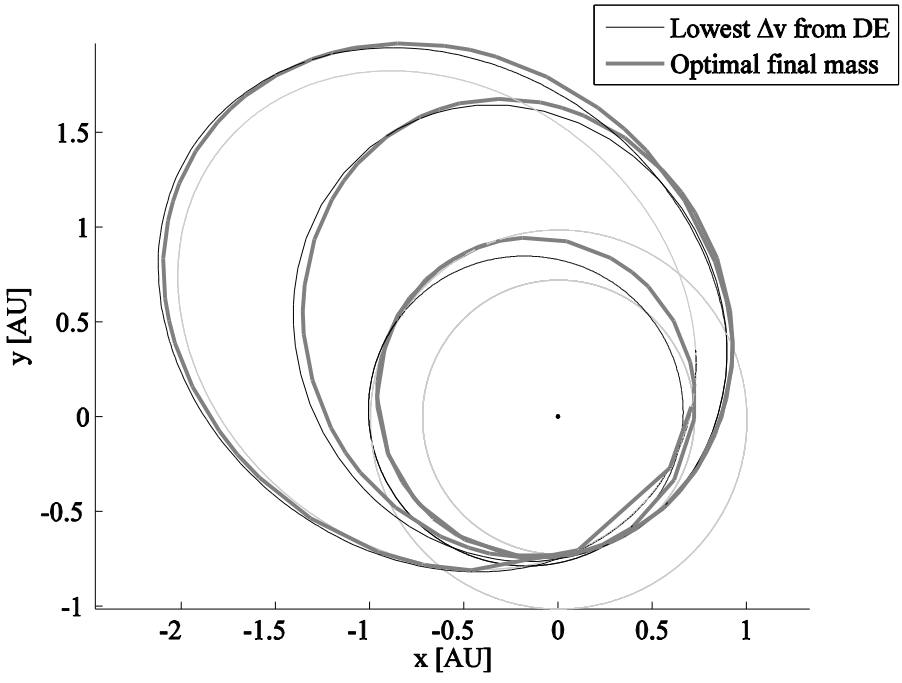

b)

Fig. 4.6: Result from DE with the lowest Δv and its optimised solution from DITAN, a) thrust profile, b) trajectory plot

Fig. 4.6 shows that the optimised transfer is close to the initial guess. The initial relative launch velocity reduces the pericenter to Venus's level and the Venus gravity assist occurs after coasting for more than one revolution. The Venus flyby raises the apocenter of the trajectory. The following flyby at Earth further raises the apocenter and aligns the line of apsides with that of Apollo. Both gravity assists are beneficially exploited, reducing the necessary total Δv for the rendezvous. The role of the

manoeuvres at the final leg is to adjust the keplerian elements to arrive with no relative velocity. It is noteworthy that the optimal result found by DITAN employs manoeuvres only in the last leg, while the first two legs are coast arcs. The physical explanation is that manoeuvres are more efficient at greater distance from the Sun, where the thrust to local gravity field magnitude is higher.

4.5.3 Earth-Venus-Earth-Earth-Jupiter rendezvous

Another target body to rendezvous with that was used as test for the pruning algorithm was Jupiter. Its orbital elements are reported in Table 4.4. Because of the larger semi-major axis of Jupiter compared to the Earth's, employing successive gravity-assists can be beneficial to lower the total Δv. The same sequence of flyby planets as for the Galileo mission was used.

Table 4.4 Orbital elements of Jupiter

Semi-major axis	5.203 AU
Eccentricity	0.05
Inclination	1.3°
Ascending node	100.4°
Argument of pericenter	273.9°

This LTMGA transfer has four legs. The launch window W was set to be the interval between 1st January 2010 and 1st January 2020. W was discretised into 240 equidistant dates, i.e. in average two launch dates per month. The first leg's range of times of flight was set to [50 d ; 500 d], the second one's to [50 d ; 700 d], the third one to [100 d ; 1000 d] and the fourth to [500 d ; 2000 d]. The ranges of encounter dates were discretised into respectively 45, 65, 90 and 75 points. The initial relative velocity was allowed to be 5 km/s at most and limits were set on the last three leg's total Δv to 10 km/s, 10 km/s and 15 km/s respectively. It can be therefore noted that the discretisation grid is course while the pruning criteria are not stringent. The minimal altitude allowed for all gravity assists was 200 km. The pruned pairs of legs are plotted in Fig. 4.7.

In total, 5 separate hyperboxes were obtained by the pruning, and a differential evolution algorithm was run on all of them, in order to locate the global minimum.

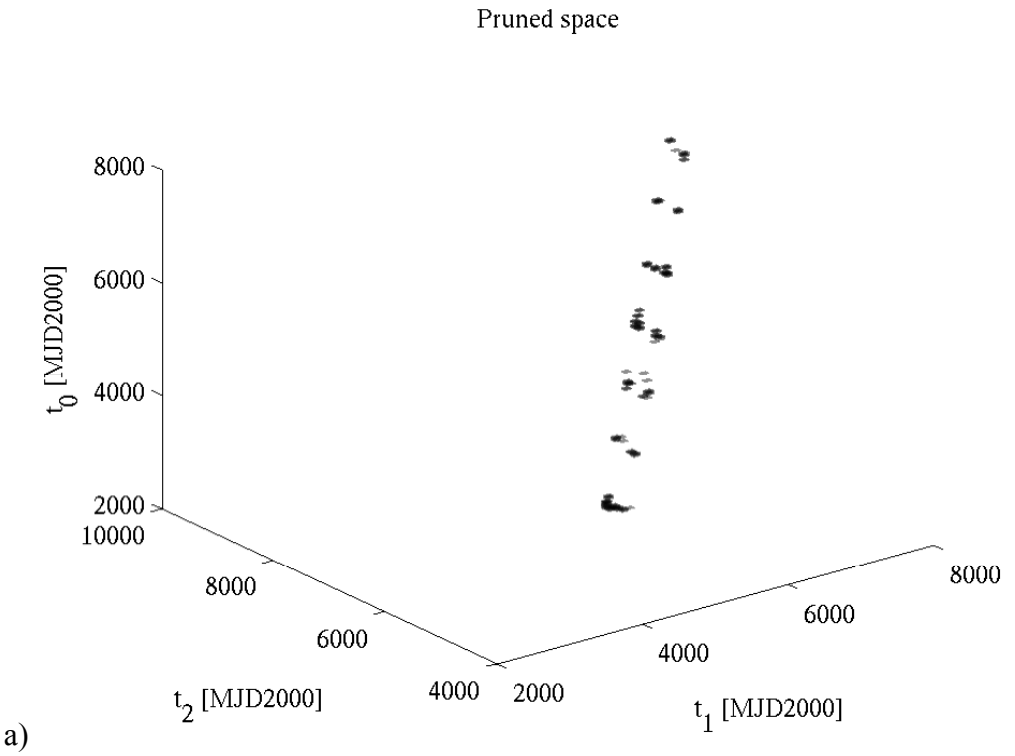
Pruned space
8000
6000
4000
2000
t_0 [MJD2000]
10000
8000
6000
4000
t_2 [MJD2000]
2000
4000
6000
8000
t_1 [MJD2000]

a)

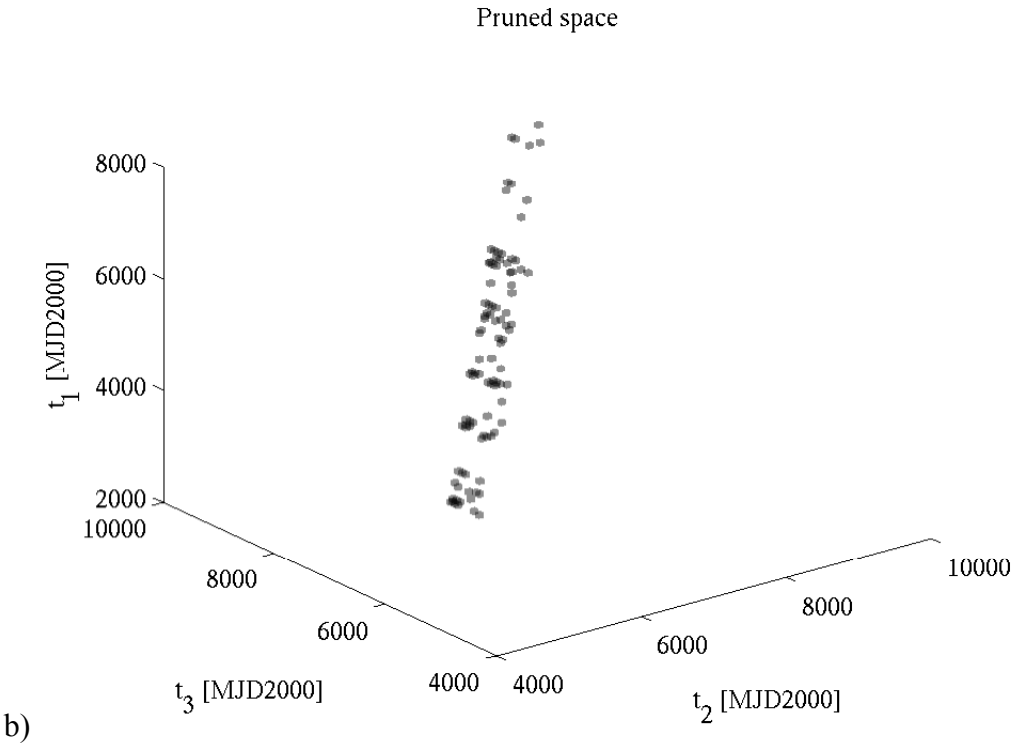
Pruned space
8000
6000
4000
2000
t_1 [MJD2000]
10000
8000
6000
4000
t_3 [MJD2000]
4000
6000
8000
10000
t_2 [MJD2000]

b)

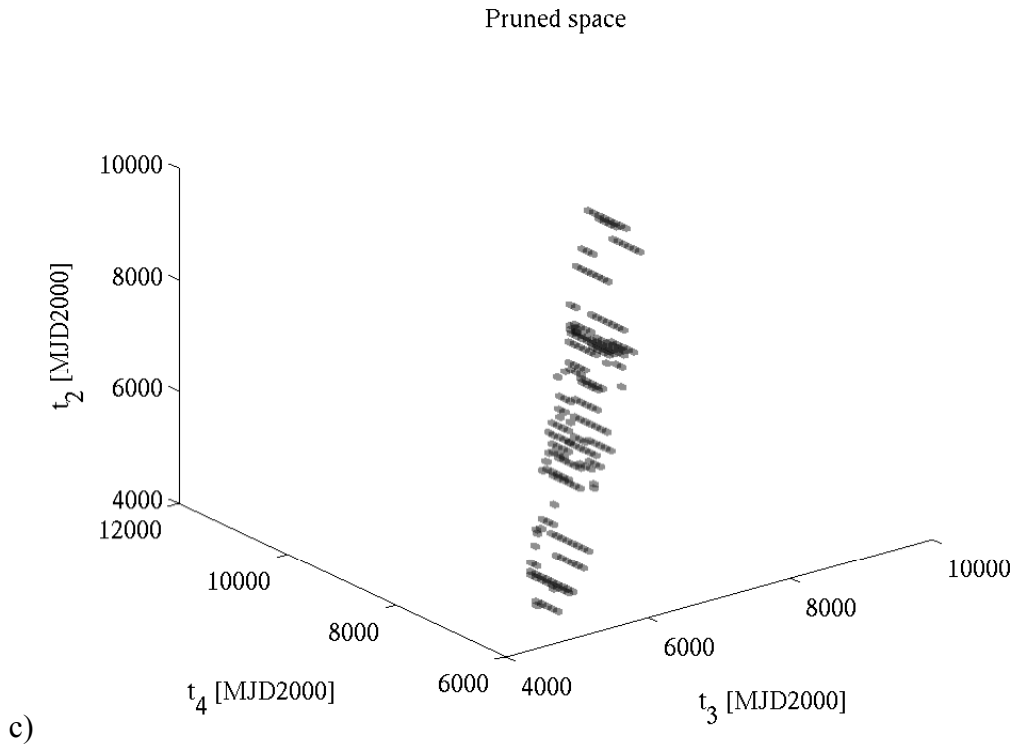

c)

Fig. 4.7: Plotted are the triplets of dates, corresponding to the pair of a) Earth-Venus-Earth legs, b) Venus-Earth-Earth legs, c) Earth-Earth-Jupiter legs, that were not pruned

Table 4.5: Dates at each planet for the LTMGA trajectory with the lowest Δv, obtained from the differential evolution and from DITAN

	Date from DE	Date from DITAN
Launch from Earth	15/1/2017	3/2/2017
Venus GA	20/4/2017	20/4/2017
First Earth GA	28/8/2018	1/9/2018
Second Earth GA	25/3/2021	25/3/2021
Rendezvous at Jupiter	8/9/2024	27/12/2024

The lowest Δv obtained from DE was 7.66 km/s plus a relative launch velocity of 3.58 km/s, to be compared with the Hohmann transfer's 14.44 km/s. The total time of flight is 7.65 years. One should note that the Δv also includes the gravity loss due to the low and long nature of the thrust arcs. The optimised transfer from DITAN has a Δv 6.64 km/s and the relative launch velocity is 5 km/s which is the maximum value allowed. Table 4.5 provides the dates of encounter of each planet for that trajectory. Fig. 4.8 illustrates how close the best transfer from the DE is from the optimal transfer computed by DITAN. It is worth mentioning that the optimised transfer only employs thrust arcs at the last leg on the way to Jupiter, when the spacecraft is far from the Sun, because the thruster has more effect on the trajectory at greater distances. The

role of the thrust arc at the last leg is mainly to raise the pericenter to the level of Jupiter.

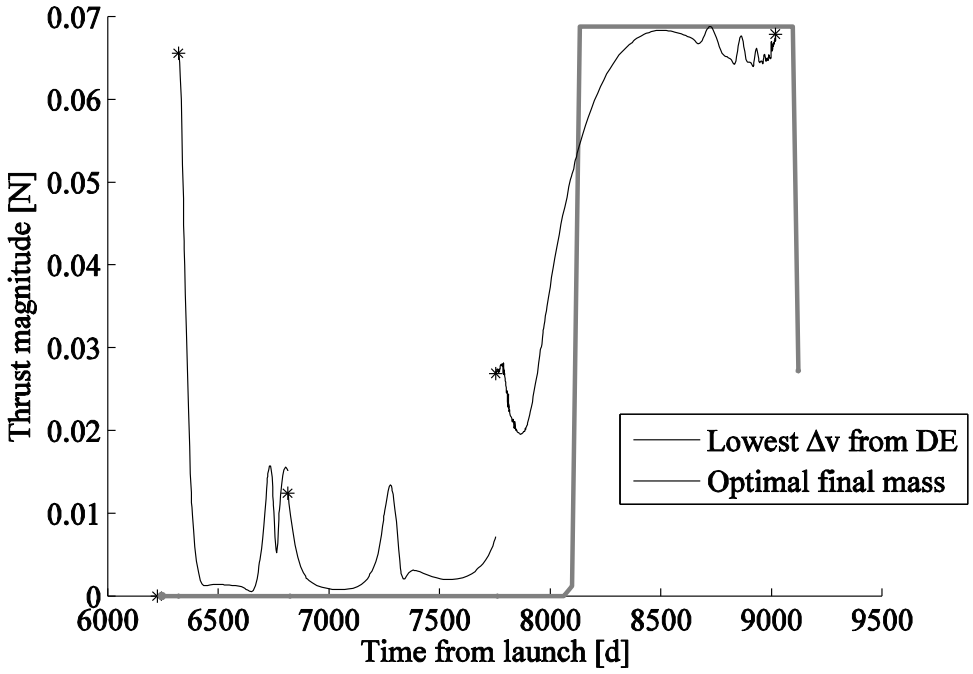

a)

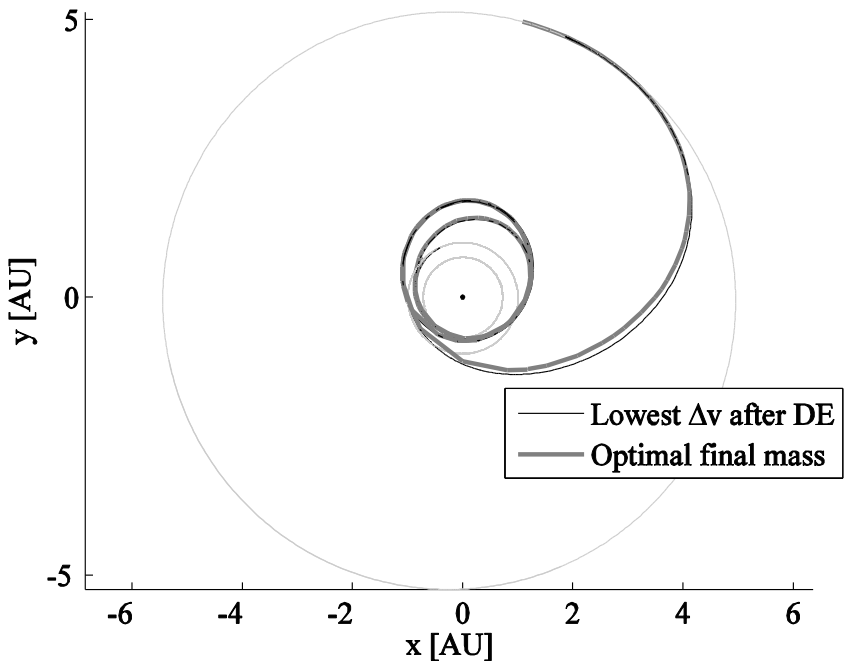

b)

Fig. 4.8 Comparison between the best transfer obtained from the DE and the corresponding optimal result from DITAN: a) thrust profiles, b) trajectory plot

4.6 Limitations

While the pruning and the generation of the hyperboxes reduce the total search space considerably and keep promising regions, the number of hyperboxes is difficult to difficult to predict. The number depends on the density of the discretisation of the encounter dates and the stringency of the filtering of each leg. Therefore, running a global optimisation can become long if many hyperboxes result from a pruning. The parameters need to be well set for a good compromise between computational intensity and quality of the results.

Moreover, it can happen that a hyperbox contains only unacceptable transfers for a given leg, because of the way hey are constructed. In fact, when constructing a box around a cluster of date triplets, there will be areas in the box that contain unacceptable legs. Therefore when intersecting boxes for consecutive pairs of legs, the intersections may only contain these regions of unacceptable legs.

CHAPTER 5 CONCLUSIONS

5.1 Summary and findings of the thesis

The purpose of this thesis was to ease a mission analyst's task to generate a variety of interesting low thrust transfers satisfying a certain number of constraints while keeping computational efforts reasonably low. The approach has been to address first direct transfers between a departure and arrival planet. An essential tool of generating low thrust trajectories from scratch has been developed. It was sought that resulting trajectories would estimate well the level of optimality for propellant mass consumption, such that large sets of transfers could be generated, and then pruned out to keep most promising ones. Transfer generating tools can be used by global optimisers to identify promising regions in a search space, as well as by local optimisers to provide an initial guess.

Since generally the generating tools do not provide optimal transfers, and optimising locally can be computationally intensive, an efficient method to improve the trajectories locally was developed. With such a tool, the mission analyst can identify the regions of interest in the search space with more confidence. The compromise is between computational efficiency and level of improvement of the trajectory.

Finally the issue of MGA transfers was addressed. Gravity assist is more and more being used to reduce necessary propellant to carry on board interplanetary missions, however the difficulty of finding the best trajectories is increased by the dimensions of the search space that each candidate swingby planet adds. A method to address the problem of dimensionality has been developed based on an incremental method first proposed by Becerra et al. With this method, the trajectory generators and improvers can be used for each leg, while the overall search strategy is governed by an incremental pruning that keeps the search space polynomial with the number of swingby planets. The outputs of the pruning are candidate trajectories that can be used to initialise local optimisers on the full transfer.

5.1.1 Shaping methods

A trajectory shaping approach has been adopted to generate trajectories from scratch due to their flexibility and their computational efficiency. Due to the description of the trajectory using analytical functions, the control profile from the equations of motion without propagation, and boundary constraints can be applied easily if the shaping functions are well chosen.

Several authors have already studied this approach; this thesis provided a unified mathematical framework in which any shaping can be applied, independently of the coordinates, or the equations of motion. The standardised framework enabled then to develop a new shaping method, dubbed spherical shaping, that describes the evolution of spherical coordinates by assigning shaping functions to them. This method is a generalisation to three dimensions of the exponential sinusoids and the polar shaping proposed by Petropoulos et al. and Wall et al.

The new framework also let Vasile and De Pascale's pseudo-equinoctial shaping to be revisited. The major contribution of the thesis is the understanding of the non-osculating nature of the elements that the shaping functions parameterise.

Only six equations of motion were used to describe the system, the mass evolution being obtained by specifying a posteriori a propulsion model. To obtain a propellant mass corresponding to a trajectory, one needs at least an initial spacecraft mass and a specific impulse as input, but a more complicated model can also be applied with dependencies on the available power, distance from the Sun, etc. There would still be no need to use a propagator for the trajectories.

Numerical integration of the trajectory is however generally necessary if one wants to compute the Δv and the time of flight. But since the trajectories are normally sampled at multiple points for analysis reasons, one can choose in that case sufficiently dense Gauss points on which integration becomes straightforward.

Attention was paid in both methods for the shaping functions to cover the case of pure Keplerian transfer arcs, such that in the vicinity of Keplerian arcs, by the continuous nature of the problem, the generated trajectory keeps a low Δv.

Time of flight constraints are shown to be satisfied by a applying a Newton loop first followed by a reshaping of the time evolution along the trajectory if there is no convergence. The reason for not applying only an independent shaping to the time coordinate like for the other coordinates is that it is difficult to find a generic

analytical expression for the time evolution that ends up with an acceptable thrust profile. Therefore, in the spherical shaping, the time evolution was shaped using an expression depending on the distance from the central body, such that the control profile is assumed to have tangential and out-of-plane components. This assumption is proven to be reasonable in most cases and ends up in trajectories that are close to optimal in many cases. In the pseudo-equinoctial case, the time evolution is also assumed to have the expression of the one of a trajectory without normal component.

Test cases prove that both shaping methods can identify promising regions in a search space and can initialise a local optimiser. It was shown that satisfying time of flight constraints with a Newton loop on an extra coefficient in the shaping functions is feasible in all the interesting cases and that the Newton loop only breaks down when the number of revolutions is inappropriate with the desired time of flight.

The test cases all cover heliocentric transfers, however the trajectory generation can also be applied for orbit changes around a planet like the Earth, in which case time constraints are not always necessary because one does not need to arrive to the final orbit at a given time.

The theoretical basis for a hybrid shaping has also been laid down. The motivation for its development was to combine the advantages of both the spherical shaping and the pseudo-equinoctial shaping. The number of shaped parameters was reduced to three from five in the case of the pseudo-equinoctial shaping and the equinoctial elements derived from them satisfy the variational equations so are osculating. Moreover the out-of-plane behaviour of the shaping covers the case of the Keplerian motion, unlike in the spherical shaping. Unfortunately, no generic expression for the shaping functions has been found that results in transfers with Δvs low enough to be considered interesting in practice. This opens up a direction for the future research.

5.1.2 LQ controller

The LQ controller was developed with the purpose of improving transfers, both in terms of Δv and peak thrust. In fact, when pruning large numbers of candidate trajectories, the latter two are common bases for filtering. An improvement is sought for in the vicinity of a reference trajectory after linearising the 6 equations of motion for position and velocity. The rationale is that by optimising for the L_2 norm of the

control vector, thrust profiles tend to be smoothed out and peak thrusts reduced, which in turn can reduce Δv.

The term improvement is used instead of optimisation because a fully-fledged efficient optimisation is not available and the optimal trajectory corresponding to the linearised system does not necessarily correspond to an optimal trajectory in the non-linearised model.

An estimate was provided for the error between the linearise and the non-linearised trajectory and it was shown that the error decreases with the square of the distance with respect to the central body.

It was then proved in a theorem that the two are the same if and only if the reference trajectory is already optimal. It was shown in test cases, that when the linearised trajectory does not diverge too much from the corresponding real trajectory, then the LQ controller does improve the real trajectory. This is the case when reference thrust is not high for extended portions of the trajectory.

Adding a specific model for the propulsion system can be done a posteriori after computing the improved trajectory, while another option is to include this model in the equation governing the evolution of mass and linearise that model as well around the reference trajectory. In that case the system becomes 7 dimensional and the Riccati equation to solve becomes 49 dimensional up from 36, a 36% increase. It was deemed that the increase in computing intensity does not necessarily compensate for the potential improvement of the reference trajectory. In fact, by linearising the propulsion model, the optimal linearised trajectory would not automatically result in improved trajectories satisfying the real equations of motion.

The LQ controller has been applied to numerous test cases covering different mission types. A systematic search has been applied in order to assess the regions where the controller best works.

5.1.3 Incremental pruning

When Becerra et al. introduced the idea of the incremental pruning of MGA transfers, the search for globally optimal transfers became computationally much easier, due to the reduction of the search space. Becerra's approach used Keplerian arcs with eventually deep space manoeuvres, as well as powered swingbys. While it would have been possible to simply use the shaping methods to generate the legs

between the encountered planets, the powered nature of the swingby would still have suggested chemical propulsion on board the spacecraft. Since this is not generally the case, Becerra's method would not have been useful for purely low thrust missions. The pruning method has therefore been adapted, such that swingbys are not powered anymore. The trick is to construct legs by pairs with a swingby in between, instead of individually. The incremental pruning therefore happens on the pairs of legs. The remaining pairs of legs are then matched with each other in order to get a full transfer.

The swingby model that has been developed is based on a simple patched conic model. The incoming and outgoing legs are computed first separately, and the velocities at the swingby are tried to be matched. If that is not possible without a manoeuvre, the second leg is modified such that its initial velocity, i.e. outgoing velocity, matches the unpowered swingby's conditions.

The spherical shaping was used to generate the trajectories since it allows constraining analytically any combination of position and velocity, which is needed for matching the legs at the gravity assist.

Boxes were defined around clusters of triplets of dates representing pairs of legs and hyperboxes are obtained by intersecting boxes for consecutive pairs of legs, such that the promising regions of the total search space are found. The search space is successfully reduced and a global optimisation can be run on each of the hyperboxes. Test cases have shown that this method results in transfers with low Δv. Due to the much bigger size of the total search space relative to the union of the hyperboxes, it can be asserted safely that the with the same number of function calls, running a global optimisation after pruning method will find better results than without pruning with very high probability

It is unfortunately not possible to predict exactly the number of hyperboxes generated by the method; the number depends on the number and configuration of the boxes, which themselves depend on initial parameters such as the density of the search grid and the pruning thresholds.

5.2 Proposed directions for future study

All tools and methods presented in this thesis have their limitations and are prone to improvement.

The expressions of the shaping functions presented in this thesis might not be the best ones, and expressions may exist that result in more interesting trajectories. The number of possible expressions is unlimited, although some physical considerations provide guidelines into choosing them. The thesis provides however the framework and one just has to plug in the new expressions. It also follows from this that interesting shaping functions might exist for the hybrid shaping that would increase the utility of this shaping method.

It might also be interesting to shape Poincaré elements. The interest in Poincaré elements lies in their canonical nature: they satisfy particularly simple equations in the Hamiltonian formulation that are reminiscent of the necessary conditions of optimality. If one shapes these elements, it may be possible to find a certain relationship between the violation of osculation and optimality.

It is to be noted that due to the general nature of the framework proposed for shaping trajectories, one is not limited to work in the two-body model. In fact, nothing restricts the user to apply a more complex physical model for the dynamics, such as three- or four-body models. Any coordinate frame can be used, including non-inertial. According to the chosen approach, certain choices of coordinates to be shaped are more relevant than others. For instance, pseudo-equinoctial elements loose their utility when a second celestial body acts substantially on the spacecraft.

In a general context, an essential tool that a mission analyst needs is a metric measuring violations of optimality. Methods have already been proposed, based on the violation of the necessary condition of optimality, but they are not necessarily robust, because adjoint variables must be computed iteratively such that the violation is minimal. Also, the ideal measure should have topologically desirable properties such as continuity, a monotonous relationship between the violation and the change in the value of the objective function.

When it comes to improving existing trajectories, it is a promising idea to keep the geometry fixed and optimise the velocity at which the satellite travels on the fixed path. The optimal time evolution is therefore a solution of a second order differential equation obtained from Lagrangian variational formulation. The two coefficients, representing the initial conditions, are set to satisfying the initial and final velocity constraints. This entails a shooting problem and an initial value must be well guessed. When the time of flight is constrained, i.e. there is an isoperimetric constraint, a constant parameter in the differential equation must be tuned such that the time of

flight is right. The author has found analytical results for the case when the trajectory is circular, but not necessarily centred on the central body, and intends to publish the results in a scientific journal in the future. This method should be studied in detail to understand whether the difficulty to solve the differential equation is compensated by the improvement of the transfer.

Adaptations to the pruning technique applied to the LTMGA transfer design could be applied. A direction of interest is not to create boxes around triplets of dates representing pairs of legs but to compute all combinations of transfers by gluing the pairs of legs together. This is a fast process that is simple to implement and the result is the list of all MGA transfers on the defined grid of encounter dates that satisfy the filter criteria for each leg. One can then sort the list, study the distribution of the transfers and optimise the best transfers, both with the shaping functions and with local optimiser using a full physical model. If the grids are dense enough, one should localise the global optimal. A special study however is necessary to prove that for a given grid density the optimal transfer does not migrate out of the clusters of promising trajectories, in which case there is a risk of missing promising regions in the total search space.

APPENDIX A Derivation of the velocity and acceleration's expressions in different reference frames

This appendix presents the derivations for the expressions of $\tilde{\mathbf{v}}$ and $\tilde{\mathbf{a}}$ in different reference frames. The resulting expressions are used in particular in the computation of D in (2.12). Three coordinate systems are introduced, together with their basis vectors:

- The Cartesian coordinates *(C)*, with basis vectors $(\mathbf{i},\mathbf{j},\mathbf{k})$
- The spherical coordinates *(S),* with basis vectors $(\mathbf{e}_r,\mathbf{e}_\theta,\mathbf{e}_\varphi)$
- The radial-orthoradial-out-of-plane coordinates *(R),* with basis vectors $(\mathbf{e}_r,\mathbf{e}_\theta,\mathbf{e}_\varphi)$

Written in *(C)*, the basis vectors of *(S)* are:

$$\mathbf{e}_r = \begin{pmatrix} \cos\theta\cos\varphi \\ \sin\theta\cos\varphi \\ \sin\varphi \end{pmatrix}_{(C)}$$

$$\mathbf{e}_\theta = \begin{pmatrix} -\sin\theta \\ \cos\theta \\ 0 \end{pmatrix}_{(C)}$$

$$\mathbf{e}_\varphi = \mathbf{e}_r \times \mathbf{e}_\theta = \begin{pmatrix} -\cos\theta\sin\varphi \\ -\sin\theta\sin\varphi \\ \cos\varphi \end{pmatrix}_{(C)}$$

therefore the matrix that transforms the coordinates of a vector in *(S)* to the coordinates in *(C)* is:

$$P_{(S)\to(C)} = \begin{pmatrix} \cos\theta\cos\varphi & -\sin\theta & -\cos\theta\sin\varphi \\ \sin\theta\cos\varphi & \cos\theta & -\sin\theta\sin\varphi \\ \sin\varphi & 0 & \cos\varphi \end{pmatrix}$$

By differentiating the components of basis vectors of *(S)*, and using $P_{(C)\to(S)} = P^{-1}_{(S)\to(C)} = P^{T}_{(S)\to(C)}$, one obtains the expression of the derivatives of $\mathbf{e}_r$, $\mathbf{e}_\theta$ and $\mathbf{e}_\varphi$ with respect to θ, expressed in *(S)*:

$$\frac{d\mathbf{e}_r}{d\theta} = \begin{pmatrix} 0 \\ \cos\varphi \\ \varphi' \end{pmatrix}_{(S)}$$

$$\frac{d\mathbf{e}_\theta}{d\theta} = \begin{pmatrix} -\cos\varphi \\ 0 \\ \sin\varphi \end{pmatrix}_{(S)}$$

$$\frac{d\mathbf{e}_\varphi}{d\theta} = \begin{pmatrix} -\varphi' \\ -\sin\varphi \\ 0 \end{pmatrix}_{(S)}$$

The velocity vector $\tilde{\mathbf{v}} = d\mathbf{r}/d\theta$ can now be expressed in the spherical coordinates, knowing that $\mathbf{r} = r\mathbf{e}_r$:

$$\begin{aligned} \tilde{\mathbf{v}} &= r'\mathbf{e}_r + r\frac{d\mathbf{e}_r}{d\theta} \\ &= \begin{pmatrix} r' \\ r\cos\varphi \\ r\varphi' \end{pmatrix}_{(S)} \end{aligned}$$

The out-of-plane basis vector is therefore:

$$\begin{aligned} \mathbf{e}_h &= \frac{\mathbf{e}_r \times \tilde{\mathbf{v}}}{\left\| \mathbf{e}_r \times \tilde{\mathbf{v}} \right\|} \\ &= \frac{1}{\sqrt{U}} \begin{pmatrix} 0 \\ -\varphi' \\ \cos\varphi \end{pmatrix}_{(S)} \end{aligned}$$

where $U = \varphi'^2 + \cos^2\varphi$. $\mathbf{e}_o$ is finally expressed in the spherical coordinates:

$$\begin{aligned} \mathbf{e}_o &= \mathbf{e}_h \times \mathbf{e}_r \\ &= \frac{1}{\sqrt{U}} \begin{pmatrix} 0 \\ \cos\varphi \\ \varphi' \end{pmatrix}_{(S)} \end{aligned}$$

The matrix that transforms the coordinates of a vector in *(R)* to the coordinates in *(S)* is then:

$$P_{(R)\to(S)} = \begin{pmatrix} 1 & 0 & 0 \\ 0 & \dfrac{\cos\varphi}{\sqrt{U}} & \dfrac{-\varphi'}{\sqrt{U}} \\ 0 & \dfrac{\varphi'}{\sqrt{U}} & \dfrac{\cos\varphi}{\sqrt{U}} \end{pmatrix}$$

Using $P_{(S)\to(R)} = P^{-1}_{(R)\to(S)} = P^{T}_{(R)\to(S)}$, the velocity vector can be expressed in *(R)*:

$$\tilde{\mathbf{v}} = \begin{pmatrix} r' \\ r\sqrt{U} \\ 0 \end{pmatrix}_{(R)}$$

From the latter, one can see that to get the components of $\tilde{\mathbf{a}} = d\tilde{\mathbf{v}}/d\theta$ in *(R)*, the expressions of $d\mathbf{e}_r/d\theta$ and $d\mathbf{e}_o/d\theta$ are required. $P_{(S)\to(R)}$ provides the components of $d\mathbf{e}_r/d\theta$ in *(R)*:

$$\frac{d\mathbf{e}_r}{d\theta} = \begin{pmatrix} 0 \\ \sqrt{U} \\ 0 \end{pmatrix}_{(R)}$$

By differentiating $\mathbf{e}_o$ and using the expression of $d\mathbf{e}_\theta/d\theta$ and $d\mathbf{e}_\varphi/d\theta$ in spherical coordinates, one gets $d\mathbf{e}_o/d\theta$ in *(S)* first:

$$\frac{d\mathbf{e}_o}{d\theta} = \begin{pmatrix} -\sqrt{U} \\ -U^{-3/2}\varphi'\left(\cos\varphi\left(\varphi'' - \sin\varphi\cos\varphi\right) + 2U\sin\varphi\right) \\ U^{-3/2}\cos\varphi\left(\cos\varphi\left(\varphi'' - \sin\varphi\cos\varphi\right) + 2U\sin\varphi\right) \end{pmatrix}_{(S)}$$

and then, with $P_{(S)\to(R)}$, the latter is expressed in *(R)*:

$$\frac{d\mathbf{e}_o}{d\theta} = \begin{pmatrix} -\sqrt{U} \\ 0 \\ U^{-1}\left(\cos\varphi\left(\varphi'' - \sin\varphi\cos\varphi\right) + 2U\sin\varphi\right) \end{pmatrix}_{(R)}$$

So finally $\tilde{\mathbf{a}}$ is obtained in *(R)*:

$$\tilde{\mathbf{a}} = \begin{pmatrix} r'' - rU \\ 2r'\sqrt{U} + r\varphi' \dfrac{\varphi'' - \sin\varphi\cos\varphi}{\sqrt{U}} \\ \dfrac{r}{\sqrt{U}}\left(\cos\varphi\left(\varphi'' - \sin\varphi\cos\varphi\right) + 2U\sin\varphi\right) \end{pmatrix}_{(R)}$$

One can also check that in the spherical coordinate system, $\tilde{\mathbf{a}}$ is written:

$$\tilde{\mathbf{a}} = \begin{pmatrix} r'' - rU \\ 2r'\cos\varphi - 2r\varphi'\sin\varphi \\ 2r'\varphi' + r\left(\varphi'' + \sin\varphi\cos\varphi\right) \end{pmatrix}_{(S)}$$

The expression of $\tilde{\mathbf{a}}$ in Cartesian coordinates is obtained by applying $P_{(S)\to(C)}$ to the latter.

APPENDIX B Derivation of the elevation angle profile for Keplerian arcs

This appendix establishes a relationship between the elevation angle, the azimuthal angle and the inclination of a given orbit. This relationship is then approximated for low inclinations and a simple expression is derived to shape the elevation angle such that the orbital plane evolves linearly. That expression is then used for all the spherical shaping methods.

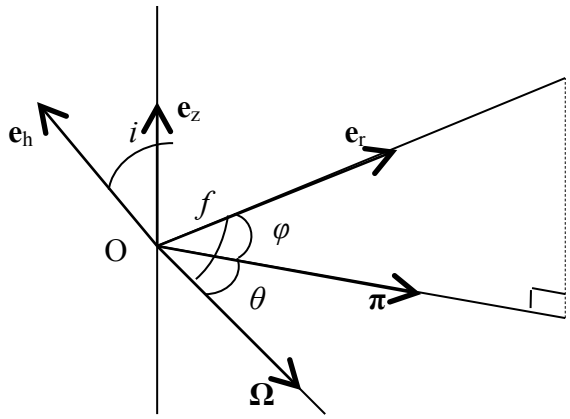

Fig. B.1 Illustration of the angles and vectors present in the spherical and the radial-orthoradial-out-of-plane reference frames. $\boldsymbol{\Omega}$ is the direction of the ascending node, $\mathbf{e}_h$ the unitary vector carrying the angular momentum, $\mathbf{e}_r$ the unitary vector carrying the radius vector, $\boldsymbol{\pi}$ the unitary vector carrying the orthogonal projection of $\mathbf{e}_r$ on the equatorial plane, i the orbital inclination, θ the azimuthal angle, φ the elevation angle and f the sum of the true anomaly and the argument of pericenter.

A first relationship between the angles illustrated in Fig. B.1 is obtained. All the vectors are considered unitary and the angles present in the figure are defined as follows:

$$
\begin{aligned}
i &= \left(\mathbf{e}_z, \mathbf{e}_r\right) \\
\theta &= \left(\boldsymbol{\Omega}, \boldsymbol{\pi}\right) \\
\varphi &= \left(\boldsymbol{\pi}, \mathbf{e}_r\right) \\
f &= \left(\boldsymbol{\Omega}, \mathbf{e}_r\right)
\end{aligned}
$$

It is also assumed that $(\mathbf{e}_r \wedge \boldsymbol{\pi}) \cdot \mathbf{e}_z = 0$ and $(\boldsymbol{\Omega} \wedge \boldsymbol{\pi}) \wedge \mathbf{e}_z = 0$. One can write first $(\boldsymbol{\Omega} \wedge \boldsymbol{\pi}) \cdot (\boldsymbol{\Omega} \wedge \mathbf{e}_r) = \sin\theta \mathbf{e}_z \cdot (\boldsymbol{\Omega} \wedge \mathbf{e}_r) = \sin\theta \cos i \sin f$. The same quantity can be also written as:

$$\begin{aligned}(\boldsymbol{\Omega} \wedge \boldsymbol{\pi}) \cdot (\boldsymbol{\Omega} \wedge \mathbf{e}_r) &= \left((\boldsymbol{\Omega} \wedge \boldsymbol{\pi}) \wedge \boldsymbol{\Omega}\right) \cdot \mathbf{e}_r \\ &= \left(\boldsymbol{\pi} - (\boldsymbol{\Omega} \cdot \boldsymbol{\pi})\boldsymbol{\Omega}\right) \cdot \mathbf{e}_r \\ &= \boldsymbol{\pi} \cdot \mathbf{e}_r - \cos\theta \boldsymbol{\Omega} \cdot \mathbf{e}_r \\ &= \cos\varphi - \cos\theta \cos f\end{aligned}$$

There is therefore a first relationship:

$$\cos\varphi = \sin\theta \cos i \sin f + \cos\theta \cos f \tag{B.1}$$

Furthermore, from $(\mathbf{e}_r \wedge \boldsymbol{\pi}) \cdot \mathbf{e}_z = 0$ one can write $(\mathbf{e}_r \wedge \boldsymbol{\pi}) \cdot (\boldsymbol{\Omega} \wedge \boldsymbol{\pi}) = 0$. Expanding the latter equation results in:

$$\begin{aligned}(\mathbf{e}_r \wedge \boldsymbol{\pi}) \cdot (\boldsymbol{\Omega} \wedge \boldsymbol{\pi}) &= \left((\mathbf{e}_r \wedge \boldsymbol{\pi}) \wedge \boldsymbol{\Omega}\right) \cdot \boldsymbol{\pi} \\ &= \left((\mathbf{e}_r \cdot \boldsymbol{\Omega})\boldsymbol{\pi} - (\boldsymbol{\pi} \cdot \boldsymbol{\Omega})\mathbf{e}_r\right) \cdot \boldsymbol{\pi} \\ &= (\mathbf{e}_r \cdot \boldsymbol{\Omega}) - (\boldsymbol{\pi} \cdot \boldsymbol{\Omega})(\mathbf{e}_r \cdot \boldsymbol{\pi}) \\ &= \cos f - \cos\theta \cos\varphi\end{aligned}$$

So $\cos f = \cos\theta \cos\varphi$. By substituting the expression of $\cos\varphi$ in (B.1) into the latter equation, after some algebraic manipulation, one ends up with $\cos f \sin\theta = \cos i \sin f \cos\theta$, which can be rewritten as:

$$\tan\theta = \cos i \tan f \tag{B.2}$$

The latter equation is useful because it links the evolution of the true anomaly with the azimuthal angle and the inclination of the orbit.

The z-component of the radius vector is $r \sin i \sin f$, thus $\sin\varphi = z / r = \sin i \sin f$. Using (B.2) to eliminate *f*, the following expression holds:

$$\sin\varphi = \sin i \frac{\sin\theta}{\sqrt{\sin^2\theta + \cos^2 i \cos^2\theta}}$$

Finally, in the general case, when the right ascension of the ascending node Ω is arbitrary, then one has to replace θ by $\theta-\Omega$ in the previous equation, which then becomes:

$$\sin\varphi = \sin i \frac{\sin(\theta-\Omega)}{\sqrt{\sin^2(\theta-\Omega)+\cos^2 i\cos^2(\theta-\Omega)}} \tag{B.3}$$

This is an important relation for the spherical shaping because if the behaviour of the osculating plane is known, then the shape of the elevation angle as a function of the azimuthal angle is obtained. Fig. B.2 illustrates the relation between the elevation angle and the azimuthal angle when the motion stays inside a fixed plane of different inclinations. When the inclination is small, the elevation angle evolves almost as a sinusoid, whereas when the inclination approaches *π/2*, the evolution tends towards a step function with values of *-π/2* or *π/2*.

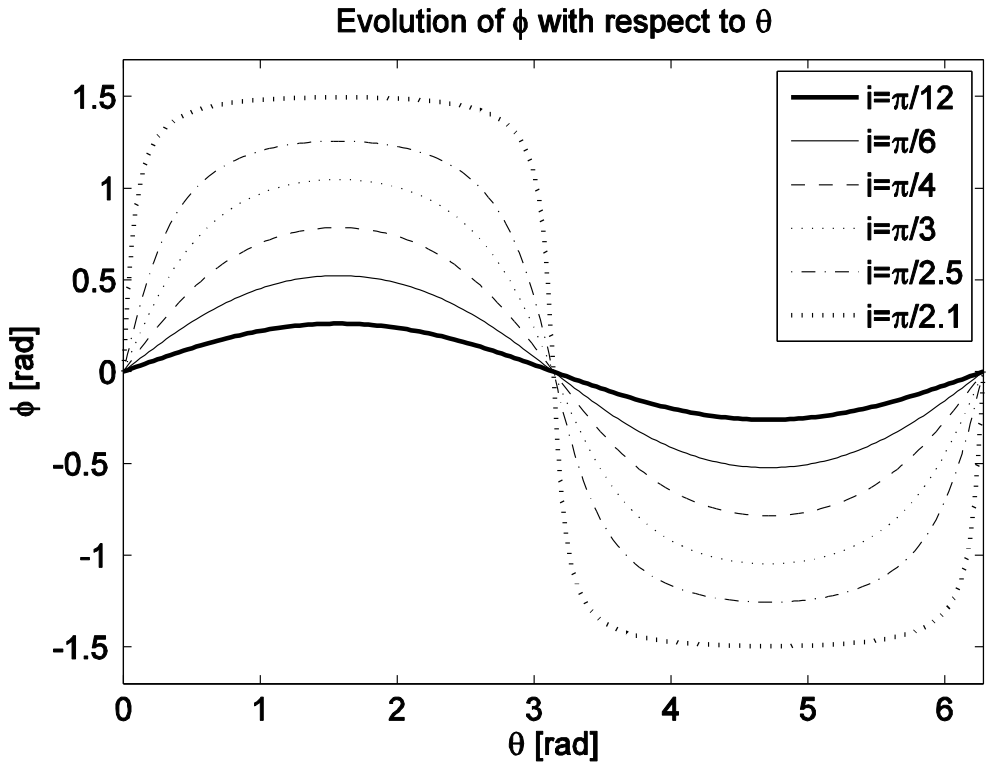

Fig. B.2 Evolution of *φ* with respect to *θ* for *Ω = 0* and different values of the inclination *i*.

If the motion stays in a plane with a constant inclination, it can be verified that the expression for φ verifies $\cos\varphi(\varphi''-\sin\varphi\cos\varphi)+2\sin\varphi(\varphi'^2+\cos^2\varphi)=0$, and one finds therefore that $\tilde{a}_h = 0$ from (2.18).

Appendix B Derivation of the elevation angle profile for Keplerian arcs

There is a simple expression for φ when the inclination i is small. If $i \ll 1$, since $|\varphi| \le i$, $|\varphi| \ll 1$ and one gets $\varphi \simeq \sin i \sin(\theta - \Omega)$. However, $\sin i \simeq 2\tan\frac{i}{2}$, so finally:

$$\begin{aligned} \varphi &\simeq 2\tan\frac{i}{2}(\sin\theta\cos\Omega - \cos\theta\sin\Omega) \\ &= 2h\sin\theta - 2k\cos\theta \end{aligned} \tag{B.4}$$

Therefore the elevation angle is a linear combination of the two equinoctial elements describing the orientation of the osculating orbital plane. If one wants to have a roughly linear evolution for h and k, then an appropriate shaping function for the elevation angle would have the expression $\Phi = (b_0 + b_1\theta)\cos\theta + (b_2 + b_3\theta)\sin\theta$, where the terms in front of the sine and cosine are small. Adopting such an approach is reasonable because it excludes brisk changes in the orientation of the orbital plane, and therefore the chances of high spikes in the magnitude of the control are reduced.

Moreover, such a shaping function covers the case of an unperturbed Keplerian orbit, where h and k remain constant, provided that the inclination of the orbit is not high. Technically, one can always define an intermediate inertial reference frame where the initial osculating orbital plane is the x-y plane, and describe the transfer in that frame using the corresponding azimuthal and elevation angle. One would have to transform all the vector components to the initial frame in the end. Proceeding this way covers exactly the planar transfer case, where the elevation angle always stays zero. Furthermore, the proposed shaping function will then provide a reasonable profile for the elevation angle for all the transfers where the inclination changes are reasonably small, with any initial inclination.

APPENDIX C Hybrid shaping method

A third, novel, shaping approach is presented here. It is a hybrid between the spherical shaping method and the pseudo-equinoctial method and has theoretical advantages compared to both. The quantity s that parameterizes the trajectory is the longitudinal anomaly L, i.e. the same parameter as in the pseudo-equinoctial shaping. As will be shown, the advantage compared to the pseudo-equinoctial shaping is the lower number of required shaping functions, due to the satisfaction of the osculating conditions. Moreover, the parameter chosen to shape the out-of-plane behavior of the trajectory covers the Keplerian motion for any inclination, based in any reference frame.

The hybrid shaping method is presented in appendix since no expression for the shaping functions has been found which results in trajectories with Δv or peak thrust values that would be interesting in practice. Further research in this direction may however end up in acceptable results.

Derivation

The motivation to construct the hybrid shaping originates from the analysis of the conditions satisfied by the osculating equinoctial elements (see (2.59)). They are reminded here:

$$\begin{cases} \dfrac{p'}{r} - f'\cos L - g'\sin L = \left(g'\dfrac{\sqrt{\mu p}}{r^2} - 1 \right)\left(f\sin L - g\cos L \right) \\ \dfrac{hk' - kh'}{1+h^2+k^2} = 1 - t'\dfrac{\sqrt{\mu p}}{r^2} \\ h'\sin L - k'\cos L = 0 \end{cases} \tag{C.1}$$

As a function of the equinoctial elements, the radius r is written:

$$r = \frac{p}{1 + f\cos L + g\sin L} \tag{C.2}$$

Analysing the system of equations in (C.1), one observes that if one chooses three functions shaping any three elements out of (p,f,g,h,k,t), the remaining three can only be obtained by solving a system of nonlinear differential equations, for which an analytical solution is generally impossible to find. However, through algebraic manipulations, it is possible to verify that if one introduces the following quantities:

$$\begin{aligned}
\tilde{f} &= f\cos L + g\sin L \\
\tilde{g} &= f\sin L - g\cos L \\
\tilde{h} &= h\cos L + k\sin L \\
\tilde{k} &= h\sin L - k\cos L
\end{aligned} \tag{C.3}$$

then (C.1) takes the form:

$$\begin{cases}
r'\sqrt{\dfrac{p}{\mu}} = \tilde{g}t' \\
\dfrac{\tilde{k}\left(\tilde{k}+\tilde{k}''\right)}{1+\tilde{h}^2+\tilde{k}^2} = 1 - t'\dfrac{\sqrt{\mu p}}{r^2} \\
\tilde{k}' = \tilde{h}
\end{cases} \tag{C.4}$$

where

$$r = \frac{p}{1+\tilde{f}} \tag{C.5}$$

Analysis of equations (C.4) leads to a useful observation. Indeed, if one chooses to assign shaping functions to r, p and $\tilde{k}$, then one can apply the reformulated osculating conditions (C.4) and obtain all the remaining parameters with simple algebra. The steps to perform are the following:

- Obtain $\tilde{h}$ from the third equation
- From the second equation get t'
- Get $\tilde{g}$ from the first equation
- Inverting equations (C.3) in order to one obtains the equinoctial elements *f*, *g*, *h* and *k*:

$$\begin{aligned} f &= \tilde{f}\cos L + \tilde{g}\sin L \\ g &= \tilde{f}\sin L - \tilde{g}\cos L \\ h &= \tilde{h}\cos L + \tilde{k}\sin L \\ k &= \tilde{h}\sin L - \tilde{k}\cos L \end{aligned} \tag{C.6}$$

- Recover the Cartesian position and velocity using (2.54), (2.56) and (2.57)

In a summary, if functions of L shaping the radius, the semi-latus rectum and the parameter $\tilde{k}$ are introduced, denoted respectively by R, P and $\tilde{K}$, then the trajectory will be completely defined. It is worth noting that R and $\tilde{K}$ carry purely geometrical information on the trajectory, whereas information on the dynamics is provided by the shaping of the semi-latus rectum, since it is related to the angular momentum by $P = \mathbf{h}^2 / \mu$. Hence the time of flight is also set by the provision of R, P and $\tilde{K}$.

Interpretation of the new parameters

Using (2.53) and (C.3), the parameters $\tilde{f}$, $\tilde{g}$, $\tilde{h}$ and $\tilde{k}$ have the following relationship with the Keplerian elements:

$$\begin{aligned} \tilde{f} &= e\cos\nu \\ \tilde{g} &= e\sin\nu \\ \tilde{h} &= \tan\frac{i}{2}\cos(\omega+\nu) \\ \tilde{k} &= \tan\frac{i}{2}\sin(\omega+\nu) \end{aligned} \tag{C.7}$$

It is clear therefore that these parameters are not conventional elements since they are not constant along an orbit. However, they can be related to usual physical quantities. An additional note can be made on the physical quantity that $\tilde{k}$ represents. $\tilde{k}$ has no units and in the case of an inclined unperturbed elliptical orbit, the value of $\tilde{k}$ oscillates between $-\tan i/2$ and $\tan i/2$, and is zero at the line of nodes. $\tilde{k}$ is therefore related to the instantaneous elevation φ of the radius vector. The relationship becomes very simple with the assumption of low inclinations, since (B.4) leads to $\tilde{k} \simeq \varphi/2$.

$\tilde{g}$ can also be expressed through quantities that have more physical meaning. Starting with the first equation in (C.4) one obtains:

$$\tilde{g} = \frac{r'}{t'}\sqrt{\frac{p}{\mu}} = \frac{\dot{r}\left\|\mathbf{h}\right\|}{\mu} = \frac{v_r\left\|\mathbf{h}\right\|}{\mu} \tag{C.8}$$

Therefore $\tilde{g}$ is proportional to the radial velocity and the magnitude of the angular momentum.

Particular case of a planar transfer

In this subsection the case of planar transfers is analysed. A trajectory will not be perturbed in the out-of-plane direction if $\tilde{k} = 0$ along the trajectory. Hence, from, $\tilde{h} = 0$, from which follows that:

$$t' = \frac{r^2}{\sqrt{\mu p}} \tag{C.9}$$

and

$$\tilde{g} = p\frac{r'}{r^2} \tag{C.10}$$

The relationship (C.9) is significant because of the absence of the controls, meaning that if the radius and the semi-latus rectum are fixed then *t'* is fixed. Thus, if one assigns a given profile for the radius, i.e. *r'* is also fixed, then the magnitude of the velocity will be constrained to be

$$\left\|\mathbf{v}\right\| = \frac{1}{t'}\sqrt{r'^2 + r^2} = \frac{\sqrt{\mu p\left(r'^2 + r^2\right)}}{r^2} \tag{C.11}$$

Implementation of boundary constraints

It is presented here how boundary constraints can be enforced for to a trajectory modelled by the hybrid shaping. Assuming that the shaping functions to be constrained are *R*, *P* and $\tilde{K}$ and that both the position $\mathbf{r}_0$ and velocity $\mathbf{v}_0$ are to be met, then the following steps are performed to obtain the values of the shaping functions at the point of interest:

1. compute $r_0 = \|\mathbf{r}_0\|$, $\mathbf{h}_0 = \mathbf{r}_0 \wedge \mathbf{v}_0$ and $\mathbf{p}_0 = h_0^2 / \mu$
2. compute the inclination i_0 from $\cos i_0 = \mathbf{h}_0 \cdot \mathbf{e}_z$
3. compute the ascending node's direction $\mathbf{u}_0 = \mathbf{h}_0 \wedge \mathbf{e}_z$ and Ω_0 from $\cos \Omega_0 = \dfrac{\mathbf{u}_0 \cdot \mathbf{e}_x}{\|\mathbf{u}_0\|}$ and $\sin \Omega_0 = \dfrac{\mathbf{u}_0 \cdot \mathbf{e}_y}{\|\mathbf{u}_0\|}$
4. compute $\omega_0 + \upsilon_0$ from $\cos(\omega_0 + \upsilon_0) = \mathbf{r}_0 \cdot \mathbf{u}_0 / (r_0 \|\mathbf{u}_0\|)$ and
$$\sin(\omega_0 + \upsilon_0) = \operatorname{sgn}\left(\mathbf{h}_0 \cdot (\mathbf{u}_0 \wedge \mathbf{r}_0)\right) / \sqrt{1 - \cos^2(\omega_0 + \upsilon_0)}$$
5. compute L_0 and $\tilde{k}_0$ and $\tilde{h}_0$ from $L_0 = \Omega_0 + \omega_0 + \nu_0$ and (C.7)

In the particular case when the result of step 2 is $i_0 = \pi/2$, in step 3 $\mathbf{u}_0$ is set to $\mathbf{e}_x$ and Ω_0 to *0*.

Note that these steps define the inverse operation of the one presented in subsection 0, whereby the position and velocity are computed from *R*, *P* and $\tilde{K}$. A set of three equations defining boundary constraints is thus given:

$$\begin{aligned} R(L_0) &= r_0 \\ P(L_0) &= p_0 \\ \tilde{K}(L_0) &= \tilde{k}_0 \end{aligned} \tag{C.12}$$

These three, combined with the value set for the longitudinal anomaly L_0 add up to four boundary constraints. The two additional boundary constraints are obtained from osculating conditions (C.4) for the new parameters. First the value of $\tilde{g}_0$ is obtained from $v_{r0} = \mathbf{v}_0 \cdot \mathbf{r}_0 / r_0$ and (C.8) and the one of value of $\tilde{h}_0$ from (C.7). Then an expression for t_0' is obtained the second equation of (C.4):

$$t_0' = \frac{r_0^2}{\sqrt{\mu p_0}}\left(1 - \frac{\tilde{k}_0\left(\tilde{k}_0 + \tilde{K}''\left(L_0\right)\right)}{1+\tilde{h}_0^2+\tilde{k}_0^2}\right) \tag{C.13}$$

This expression is then plugged into the first equation of (C.4), and after rearrangements one gets:

$$R'\left(L_0\right) + \frac{\tilde{g}_0 r_0^2}{p_0}\frac{\tilde{k}_0}{1+\tilde{h}_0^2+\tilde{k}_0^2}\tilde{K}''\left(L_0\right) = \frac{\tilde{g}_0 r_0^2}{p_0}\left(1 - \frac{\tilde{k}_0^2}{1+\tilde{h}_0^2+\tilde{k}_0^2}\right) \tag{C.14}$$

This constraint is expressed as a linear combination of $R'\left(L_0\right)$ and $\tilde{K}''\left(L_0\right)$, in the same way as in the spherical shaping the constraint on T' develops into a linear combination of R'' and Φ'' (see (2.40)). The final boundary constraint comes from the third equation in (C.4) and is:

$$\tilde{K}'\left(L_0\right) = \tilde{h}_0 \tag{C.15}$$

Therefore, if the trajectory has to satisfy constraints both on position and velocity at a certain point, one degree of freedom is necessary within P, plus, due to the nature of (C.14), either two degrees of freedom for R and two for $\tilde{K}$, or one for R and three for $\tilde{K}$. However, because the coefficient in front of $\tilde{K}''\left(L_0\right)$ in (C.14) becomes zero for planar trajectories, in order to keep (C.14) solvable in that case, the choice of two degrees of freedom for R and two for $\tilde{K}$ is the more appropriate.

Based on these considerations, if constraints on both position and velocity exist at both tips of the trajectory, then four degrees of freedom are necessary for setting R, two for P and four for $\tilde{K}$, much in the same way as in the spherical shaping, where six degrees of freedom are required for R and four for Φ.

Choice of the shaping functions' expression

At this point, a particular expression can be assigned for the function governing r, p and $\tilde{k}$. It was chosen to shape the radius r, similarly to the spherical shaping (see (2.51)) because of its ability to model the Keplerian unperturbed motion. The

difference is that here the variable is the longitudinal anomaly L instead of the azimuthal angle θ and that two less coefficients are required, based on the results of subsection 0. The expression adopted for R is then:

$$R(L) = \frac{1}{a_0 + a_1 L + a_2 L^2 + a_3 \cos L + a_4 \sin L} \tag{C.16}$$

The a_2 coefficient is set to zero by default, but can be tuned to satisfy other constraints, e.g. time of flight constraints.

The semi-latus rectum p is the other parameter selected for shaping the in-plane motion of a spacecraft. The shaping function P used in the pseudo-equinoctial shaping (see (2.61)) is simple, simulates smooth evolutions, remains strictly positive once it's strictly positive at the boundaries, and is capable of covering Keplerian coast arcs. Hence the identical expression is used for the hybrid shaping:

$$P(L) = p_0 + p_1 \exp \lambda_1 L \tag{C.17}$$

λ_1, as in the pseudo-equinoctial shaping, adds a degree of freedom to design the trajectory and is called shaping parameter. Finally the out-of-plane component $\tilde{k}$ is shaped by the function $\tilde{K}$ and requires four coefficients. Since $\tilde{k} = h \sin L - k \cos L$, the expressions of H and K of the pseudo-equinoctial shaping were used for $\tilde{K}$:

$$\tilde{K}(L) = \left(h_0 + h_1 e^{\lambda_3 L}\right) \sin L - \left(k_0 + k_1 e^{\lambda_3 L}\right) \cos L \tag{C.18}$$

Like for P, an additional degree of freedom is inserted in the expression of $\tilde{K}$ that can be tuned optionally.

REFERENCES

[1] Newton, S. I., Leseur, T. and Jacquier, F., Philosophiae naturalis principia mathematica, Excudit Georgius Brookman; impensis TT et J. Tegg, Vol. 1, 1833

[2] Tsiolkovsky, K.: The exploration of Cosmic Space by Means of Reaction Motors, Scientific Review, Moscow and St. Petersburg, 1903 (Russian edition)

[3] Hohmann, W.: Die Erreichbarkeit der Himmelskörper, Verlag Oldenburg München, 1925

[4] Pontryagin, L.S. et al.: The Mathematical Theory of Optimal Processes, Vol. 4. Interscience, 1962

[5] Belbruno, E. A. and Miller, J. K.: Sun-Perturbed Earth-Moon transfers With Ballistic Capture, Journal of Guidance, Control and Dynamics, Vol. 16, 1993, pp. 770-775

[6] Turner, M. J. L. : Rocket and Spacecraft Propulsion: Principles, Practice and New Developments, Springer, 2008

[7] Humble, R.W., Henry, G.N., Larson, W.J., United States. Dept. of Defense and United States. National Aeronautics and Space Administration: Space propulsion analysis and design, McGraw-Hill, 1995

[8] Czysz, P.A. and Bruno, C.: Future spacecraft propulsion systems: enabling technologies for space exploration, Springer Verlag, 2009

[9] Dachwald, B.: Optimal solar-sail trajectories for missions to the outer solar system, Journal of Guidance, Control, and Dynamics, Vol. 28, No. 6, 2005, pp. 1187-1193

[10] Rayman, M.D., Varghese, P., Lehman, D.H. and Livesay, L.L.: Results from the Deep Space 1 Technology Validation mission, Acta Astronautica, Issues 2-9, July-November 2000, pp. 475-487

[11] Russel, C.T., Capaccioni, F., Corradini, A., Christensen, U., De Sanctis M.C., Feldman W.C., Jaumann R., Keller H.U., Konopliv A., McCord T.B., McFadden L.A., McSween H.Y., Mottola S., Neukum G., Pieters C.M., Prettyman T.H., Raymond C.A., Smith D.E., Sykes M.V., Williams B. and Zuber M.T. Dawn Discovery Mission to Vesta and Ceres: Present Status. Advances in Space Research, Vo. 38, Issue 9, 2006, pp 2043-2048

[12] Haros, D. and Schoenmakers, J.: Post-Launch Optimisation of the Smart 1 Low-Thrust Trajectory to the Moon, 18th International Symposium on Spaceflight Dynamics, Munich, Germany, 15th-22nd Oct. 2004

[13] Kuninaka H., Nishiyama K., Funaki I., Yamada T., Shimizu Y.: Powered Flight of HAYABUSA in Deep Space. 42nd AIAA/ASME/SAE/ASEE Joint Propulsion Conference & Exhibit 9-12 July 2006, Sacramento, California

[14] Yarnoz D.G., Jehn R.: Recovery Opportunities For The BepiColombo Mission To Mercury. Journal of the British Interplanetary Society, JBIS, Vol. 62, No. 10, 2009, p. 362

[15] Betts, J.T.: Survey of Numerical Methods for Trajectory Optimization, Journal of Guidance, Control and Dynamics, Vol. 21, No. 2, March-April 1998, pp. 193-207

[16] Sims, J. A., and Flanagan, S. N.: "Preliminary Design of Low-Thrust Interplanetary Missions," AAS/AIAA Astrodynamics Specialist Conference, AAS Paper 99-338, Girdwood, Alaska, Aug. 1999. Also in Advances in the Astronautical Sciences, Univelt Inc., San Diego, CA, Vol. 103, Part I, 1999, pp. 583-592

[17] Yam, C. H., Izzo, D., and Biscani, F.: "Towards a High Fidelity Direct Transcription Method for Optimisation of Low-Thrust Trajectories," 4th International Conference on Astrodynamics Tools and Techniques, Madrid, Spain, May 3-6, 2010

[18] Markopoulos, N.: Non-Keplerian Manifestations of the Keplerian Trajectory Equation and a Theory of Orbital Motion Under Continuous Thrust, AAS Spaceflight Mechanics Conference, American Astronomical Society, Washington, D.C., 2005, pp. 1061–1080

[19] Petropoulos, A.E. and Longuski, J.M.: Shape-Based Algorithm for the Automated Design of Low-Thrust, Gravity-Assist Trajectories, Journal of Spacecraft and Rockets, Vol. 41, No. 5, September-October 2004, pp. 787-796

[20] Wall, B.J. and Conway, B.A.: Shape-Based Approach to Low-Thrust Rendezvous Trajectory Design, Journal of Guidance, Control and Dynamics, Vol. 32, No. 1, January-February 2009, pp. 95-101

[21] Wall B.: Shape-Based Approximation Method for Low-Thrust Trajectory Optimization. AIAA-2008-6616, AIAA/AAS Astrodynamics Specialist Conference and Exhibit, Honolulu, Hawaii, August 18-21, 2008

[22] De Pascale P., Vasile M., Preliminary Design of Low-Thrust Multiple Gravity Assist Trajectories. Journal of Spacecraft and Rockets, Vol. 43, Number 5, September-October 2006

[23] Vasile, M., De Pascale, P. and Casotto, S.: On the optimality of a shape-based approach based on pseudo-equinoctial elements, Acta Astronautica, Volume 61, Issues 1-6, June-August 2007, pp. 286-297

[24] Rinderle, E. A.: Galileo User's Guide, Mission Design System, Satellite Tour Analysis and Design Subsystem, Jet Propulsion Laboratory, California Institute of Technology, Pasadena, CA, JPL D-263, 1986

[25] Williams, S.N. and Longuski, J.M.: Automated design of multiple encounter gravity-assist trajectories, Master's Thesis, School of Aeronautics and Astronautics, Purdue University, West Lafayette, Indiana, 1990

[26] Petropoulos, A.E., Longuski, J.M. and Bonfiglio, E.P.: Trajectories to Jupiter via gravity assists from Venus, Earth, and Mars, *Journal of Spacecraft and Rockets*, Vol. 17, No. 6, November-December 2000, pp. 776-783

[27] Petropoulos, A. E. and Longuski, J. M.: Automated design of low-thrust gravity-assist trajectories, AIAA/AAS Astrodynamics Specialist Conference, AIAA Paper, Vol. 4033, pp.157-166, 2000

[28] Izzo, D., Becerra, V. M., Myatt, D. R., Nasuto, S. J. and Bishop, J. M.: Search space pruning and global optimisation of multiple gravity assist spacecraft trajectories, Journal of Global Optimization, Springer, Vol. 38, No. 2, 2007, pp. 283-296

[29] De Pascale, P. and Vasile, M. : Preliminary Design of Low-Thrust Multiple Gravity-Assist Trajectories, Journal of Spacecraft and Rockets, Vol. 43, No. 5, 2006, pp. 1065

[30] Yam, C. H., Di Lorenzo, D. and Izzo, D.: Constrained Global Optimization of Low-Thrust Interplanetary Trajectories, IEEE Congress on Evolutionary Computation (CEC), 2010, pp. 1-7

[31] Carnelli, I., Dachwald, B. and Vasile, M.: Evolutionary Neurocontrol: A Novel Method for Low-Thrust Gravity-Assist Trajectory Optimization, Journal of guidance, control, and dynamics, Vol. 32, No. 2, March-April 2009

[32] Petropoulos, A.E. and Longuski, J.M.: Shape-Based Algorithm for the Automated Design of Low-Thrust, Gravity-Assist Trajectories, Journal of Spacecraft and Rockets, Vol. 41, No. 5, September-October 2004, pp. 787-796

[33] Becerra, V. M., Myatt, D. R., Nasuto, S. J., Bishop, J. M. and Izzo, D.: An efficient pruning technique for the global optimisation of multiple gravity assist trajectories, Acta Futura, Vol. 2005, p. 35, 2003

[34] Vasile, M., Schuetze, O., Junge, O., Radice, G., Dellnitz, M., and Izzo, D.: Spiral trajectories in global optimisation of interplanetary and orbital transfers, Technical report, Ariadna Study Report AO4919 05/4106, Contract Number 19699/NL/HE, European Space Agency, 2006

[35] Lane, S.H. and Stengel, R.F.: Flight Control Design Using Non-linear Inverse Dynamics, Automatica, Vol. 24, No. 4, 1988, pp. 471-483

[36] Baumgarte, J., “Stabilization of Constraints and Integrals of Motion in Dynamical Systems,” Computer Methods in Applied Mechanics And Engineering, Vol. 1, No. 1, Elsevier, New York, 1972, pp. 1–16

[37] Kline, M., “Calculus: An intuitive and physical approach”, Dover Publications, 1998

[38] Petropoulos, A.E. and Longuski, J.M.: Shape-based algorithm for automated design of low-thrust, gravity-assist trajectories, Journal of Spacecraft and Rockets, Vol. 41, No. 5, 2004, pp. 787-796

[39] Izzo, D.: Lambert’s problem for exponential sinusoids, Journal of Guidance, Control and Dynamics, Vol. 29, No. 5, 2005, pp. 1242-1245

[40] Battin, R. H., An introduction to the mathematics and methods of astrodynamics, AIAA Education Series, 1999, pp. 490-493

[41] Efroimsky, M.: Gauge Freedom in Astrodynamics, Modern Astrodynamics, edited by P. Gurfil, Butterworth-Heinemann, 2006, pp. 23-52.

[42] Vasile, M., Bernelli-Zazzera F.: Optimizing Low-Thrust and Gravity Assist Maneuvres to Design Interplanetary Trajectories, The Journal of the Astronautical Sciences, Vol. 51, No. 1, January-March 2003

[43] McConaghy, T.T., Debban, T.J., Petropoulos, A.E. and Longuski, J.M.: Design and optimization of low-thrust trajectories with gravity assists, Journal of spacecraft and rockets, Vol. 40, No. 3, 2003, pp. 380-387

[44] Schuetze, O., Vasile, M., Junge, O., Dellnitz, M., and Izzo, D.: Designing optimal low-thrust gravity-assist trajectories using space pruning and a multi-objective approach, Engineering Optimization, Vol. 41, No. 2, 2009